

High field investigations into the electronic state of  
unconventional superconductors

January 29, 2013

Brendan James Arnold

---

A dissertation submitted to the University of Bristol in accordance with the requirements  
for award of the degree of Doctor in Philosophy in the Faculty of Science, School of Physics



## Abstract

This thesis presents de Haas–van Alphen (dHvA) measurements on high quality samples of BaFe<sub>2</sub>P<sub>2</sub>. Energy dispersions from density functional theory (DFT) calculations were tweaked to match the measured Fermi surface orbits by rigidly shifting both the inner and outer electron energy bands and the inner hole band by 50 mRy, 43 mRy and -83 mRy respectively. The hourglass shaped outer hole band energy required no shift at the wide part and a shift of -38 mRy at the narrow part which was found to be nested with the inner electron band. To achieve a smooth transition between the two energy shift regimes, the dispersion was tweaked proportionally to the  $d_{z^2}$  band character and a complete Fermi surface was determined. The shifts were attributed to nesting conditions which were supported from calculation of the bare Lindhard susceptibility. Therefore nesting is not a sufficient condition for superconductivity.

The thermal effective masses were determined on the electron and, for the first time, hole orbits and the spin effective masses on the electron orbits. The masses showed a moderate renormalisation (between 0.88  $m_b$  and 3.04  $m_b$ ) on both hole and electron bands in line with previous literature.

In addition, Hall measurements taken in high field from 1.4 K to 300 K on good quality samples of Bi<sub>2+z-y</sub>Pb<sub>y</sub>Sr<sub>2-x-z</sub>La<sub>x</sub>CuO<sub>6+δ</sub> (BSCO2201) were presented. A sharp change in  $R_H(0\text{ K})/R_H(300\text{ K})$  was observed at  $p = 0.19$  well inside the superconducting dome which coincides with various phenomena related to the pseudogap and so hints at the fact that the pseudogap may persist inside the superconducting dome.

A simple model based on the Ong construction was fitted to the Hall data and relative magnitudes of the scattering terms,  $\Gamma = \Gamma_0 + \Gamma_1 \cos^2(2\phi)T + \Gamma_2 T^2$  were compared with terms obtained from fits to resistivity curves. The  $T$ -linear terms were found to agree within a factor of around 0.6 to 1.5 although the residual resistivity terms only agreed within an order of magnitude likely due to a lack of a  $v_F$  term in the scattering rate and the relative proximity to the van-Hove singularity. Nonetheless an increase in scaling of the  $T$ -linear term with  $T_c$  similar to that found by Abdel-Jawed *et al.* These results provide a good starting point for further refinement and possible full agreement between temperature dependent Hall and resistivity data in the cuprates without resorting to complicated Fermi surface reconstruction scenarios.

Finally a novel doping determination technique based on a method of matching high temperature Hall coefficient of BSCO2201 to that of Tl<sub>2</sub>Ba<sub>2</sub>CuO<sub>6+δ</sub> (Tl2201) as a reference material. The resulting dopings are greater than those from the ‘universal’ Presland/Tallon relation and less than those assigned to similar samples measured with angle resolved photoemission spectroscopy (ARPES). The overall spread in dopings for these samples from this new method was determined to be between  $p = 0.12$  and  $p = 0.36$ .



## Acknowledgements

Finally, it is done. This thesis marks the culmination of what has been a very enjoyable four years at Bristol working in one of the world's leading low temperature groups. Perhaps quite naturally this thesis has evolved into a work of two halves. On one side is Prof. Tony Carrington and the work exploring the pairing mechanism in the recently discovered pnictide materials and on the other side is Prof. Nigel Hussey and the work picking apart the fine detail of the cuprate phase diagram. Both supervisors have been outstanding and I would like to thank them for guiding me through the PhD with a great deal of patience and support and allowing me to spend time at summer schools in weird parts of Europe.

I would like to thank our collaborators Prof. Shibauchi and his group at Kyoto university who grew the  $\text{BaFe}_2(\text{As}_{1-x}\text{P}_x)_2$  crystals and Prof. Takeuchi and his group at Sendai University for the BSCO2201 samples. The first set of high field data taken at the Laboratoire National des Champs Magnétiques Intenses (LNCMI), Toulouse was taken with the help of Dr. Baptiste Vignolle, Prof. Cyril Proust and Dr. Patrick Rourke. The second set of high field data was taken by Dr. Baptiste Vignolle, Prof. Cyril Proust, Dr. Patrick Rourke, Prof. Nigel Hussey and Dr. Jean-Francois Mercure. The final set of high field data from High Field Magnet Laboratory (HFML), Nijmegen was taken by Dr. Patrick Rourke, Dr. Alix McCollam, Ioanna Mouzoupoulou and Dr. Xiaofeng Xu. I would also like to acknowledge Dr. Mairi Haddow for help on the x-ray characterisation.

I also owe thanks to the workshop staff, John Rowden, Adrian Crimp, Tim Newbury and especially Richard Exley who helped with experiments early on and also gave lots of help and advice regarding the first two years of the PhD spent aboard Greenwood.

I would like to thank members of the CES group throughout my time here who have made my life and work enjoyable. These include Dr. Ali Bangura, Dr. Rosie Cooper, Dr. Benoit Faque, Dr. M. French, Dr. I. Guillamon, Dr. Neil Headings, Dr. Liam Malone, Iioanna Mouzoupoulou, Carsten Putzke, Dr. Alessandro Serafin, Nick Wakeham and Phil Walmsley. I would like to thank Dr. Jon Fletcher for huge amounts of support early on and for being a pretty sound kind of person and Dr. Patrick Rourke and Dr. Jean-Francois Mercure for similar reasons. Special late night, long weekend and drinking credit goes to Dr. Xiaofeng Xu, Dr. Chris Lester and Dr. Caroline Andrew and I owe thanks to Bob Wiltshire and James Kelly for the craic. I would also like to thank the nano group, members of the IAC and others for ski trips and other general good times during this four year epilogue to my studies at Bristol.

Finally thanks to my family to whom I owe just about everything else.



## Declaration

I declare that the work in this dissertation was carried out in accordance with the requirements of the University's Regulations and Code of Practice for Research Degree Programmes and that it has not been submitted for any other academic award. Except where indicated by specific reference in the text, the work is the candidate's own work. Work done in collaboration with, or with the assistance of, others, is indicated as such. Any views expressed in the dissertation are those of the author.

SIGNED: ..... DATE:.....



*Dedicated to Elijah Steven Nisbett*



# Contents

<b>1</b>	<b>Introduction</b>	<b>1</b>
1.1	The iron-pnictides . . . . .	1
1.1.1	Fermiology of the pnictides . . . . .	2
1.1.2	The $\text{BaFe}_2(\text{As}_{1-x}\text{P}_x)_2$ series . . . . .	6
1.2	The high- $T_c$ pairing mechanism . . . . .	8
1.2.1	The case against conventional superconductivity in high- $T_c$ materials	9
1.2.2	Spin-fluctuations . . . . .	10
1.2.3	Pairing in the pnictides . . . . .	11
1.2.4	Motivation for dHvA measurements on $\text{BaFe}_2\text{P}_2$ . . . . .	12
1.3	The cuprate phase diagram . . . . .	12
1.3.1	Charge transfer insulator parent compound . . . . .	13
1.3.2	Superconducting dome . . . . .	14
1.3.3	Coherent phase . . . . .	14
1.3.4	The pseudogap . . . . .	15
1.3.5	Stripe order Fermi surface reconstruction . . . . .	16
1.3.6	Previous work by the Bristol group . . . . .	17
1.4	Properties of BSCO2201 . . . . .	19
1.4.1	Fermiology of BSCO2201 . . . . .	20
1.4.2	Determining the doping . . . . .	21
1.4.3	Motivation for high-field transport measurements on BSCO2201 . .	21
<b>2</b>	<b>Theory</b>	<b>23</b>
2.1	Band theory and the Fermi surface . . . . .	23
2.2	Fermi liquid theory . . . . .	24
2.3	De Haas-van Alphen oscillation . . . . .	24
2.3.1	Overview . . . . .	25
2.3.2	Exploring the origin of the oscillations . . . . .	26
2.3.3	Lifschitz-Kosevitch equation . . . . .	28
2.3.4	Band mass . . . . .	33
2.3.5	Final theoretical observations . . . . .	34
2.4	Spin density wave instability . . . . .	35
2.4.1	Lindhard susceptibility . . . . .	35
2.4.2	Band structure nesting . . . . .	37
2.4.3	Spin density wave fluctuations . . . . .	37
2.4.4	Notes on practical calculation . . . . .	38
2.5	Density functional theory . . . . .	39

2.5.1	The generalised gradient approximation . . . . .	40
2.5.2	Single particle wavefunction bases . . . . .	41
2.5.3	Local orbit wavefunction bases . . . . .	41
2.5.4	Code and execution details . . . . .	41
2.6	Hall effect . . . . .	42
2.6.1	Effects of Fermi surface topology . . . . .	44
<b>3</b>	<b>Experimental and Computational Methods</b>	<b>47</b>
3.1	De Haas-van Alphen torque measurement . . . . .	47
3.1.1	Experimental apparatus . . . . .	47
3.1.2	Data analysis . . . . .	50
3.1.3	Measuring the spin mass . . . . .	53
3.1.4	Extracting effective mass from the temperature dependence . . . . .	54
3.2	Calculating susceptibility . . . . .	56
3.3	Measuring charge transport . . . . .	59
3.3.1	Experimental apparatus . . . . .	59
3.3.2	Sample size determination . . . . .	64
3.3.3	Data Analysis . . . . .	64
3.3.4	Determining the doping . . . . .	67
<b>4</b>	<b>dHvA measurements on BaFe<sub>2</sub>P<sub>2</sub></b>	<b>69</b>
4.1	Sample synthesis . . . . .	69
4.2	X-Ray Diffraction . . . . .	69
4.3	Angle dependent measurements . . . . .	70
4.3.1	Determining experimental parameters . . . . .	70
4.4	Interpolating the BaFe <sub>2</sub> (As <sub>1-x</sub> P <sub>x</sub> ) <sub>2</sub> series Fermiology . . . . .	82
4.5	Harmonic parametrisation of the Fermi surface . . . . .	83
4.6	Susceptibility calculations . . . . .	84
4.7	Determining the spin effective mass . . . . .	90
4.8	Determining the thermal effective mass . . . . .	91
4.9	Conclusions . . . . .	96
<b>5</b>	<b>Hall measurements on BSCO2201</b>	<b>101</b>
5.1	Sample growth . . . . .	101
5.2	Size determination . . . . .	102
5.3	Temperature sweeps . . . . .	103
5.4	Hall plots . . . . .	106
5.4.1	Anisotropic model based on the Ong construction . . . . .	110
5.5	Doping determination . . . . .	114

5.6 Conclusions . . . . .	116
<b>6 Conclusions</b>	<b>119</b>
<b>Bibliography</b>	<b>121</b>
<b>A ‘Microfit’ parameters</b>	<b>127</b>
<b>B Lindhard susceptibility calculation code</b>	<b>129</b>
<b>C focused ion beam (FIB) scans</b>	<b>135</b>



# Chapter 1

## Introduction

---

This first part of this chapter starts with a brief general overview of the pnictides with particular focus on the Fermiology of the ‘122’ family and the  $\text{BaFe}_2(\text{As}_{1-x}\text{P}_x)_2$  series. This includes previous work by the Bristol group and how this relates to spin fluctuation mediated pairing.

The second part of this chapter describes the cuprate phase diagram. In particular it outlines some more contentious regions of the diagram such as the pseudogap and stripe order and how high field transport studies on BSCO2201 can elucidate their nature. It also details previous work performed by the Bristol group on LSCO and how performing high field measurements on BSCO2201 can provide further understanding of the mechanisms at work in the phase diagram.

---

### 1.1 The iron-pnictides

One of the most important recent breakthroughs in the field of high- $T_c$  superconductivity has been the discovery of the iron-pnictide superconductors in 2006 [1, 2] which sparked an enormous amount of interest when it was discovered that they could be tuned to transition temperatures above the historic limit in  $\text{Nb}_3\text{Ge}$  of 23 K [3].

Since their initial discovery, many different superconductors have been discovered which all feature similar tetrahedrally bonded transition metal-pnictide or transition metal-chalcogenide\* layers which are grouped by structure into families as shown in figure 1.1.1. The families are labelled according to the ratios of the constituent elements, so for example the ‘1111’ family features four element types in equal proportion, the ‘122’ family features three element types with one of the elements being half as abundant as the other two. In the case of a doped or substituted material, this labelling refers to the stoichiometric parent compound.

With the exception of the 11 family, the ‘iron-pnictide’ layers are separated by the so called ‘charge reservoir’ layers, which are comprised of a single element type in the case of the ‘122’ and the ‘111’ families and two element types in the ‘1111’ family as shown in figure 1.1.1.

---

\*For convenience, when referring to iron-pnictides in this thesis, unless otherwise stated, it should be taken to also include the various transition metal-pnictide/chalcogenide combinations that feature this tetrahedral structure.

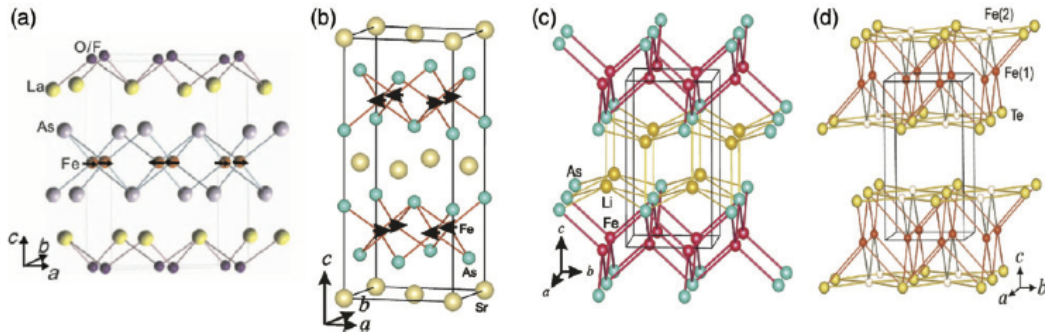


**Figure 1.1.1:** From left to right: 1111 unit cell, 122 unit cell, 111 unit cell, 11 unit cell. Adapted from ref. [4].

Although the highest  $T_c$  values have been attained with compounds in the ‘1111’ family ( $\text{SmFeAsO}_{1-x}\text{F}_x$  has a  $T_c$  of 55 K [5],  $\text{Gd}_{0.8}\text{Th}_{0.2}\text{FeAsO}$  has a  $T_c$  of 56 K [6] and  $\text{Sr}_{1-x}\text{Sm}_x\text{FeAs}$  has a  $T_c$  of 56 K [7]), it is comparatively difficult to grow large single crystals of the 1111 family causing the emphasis to be shifted to the 11 and the 122 families, especially for neutron scattering studies [4].

The most studied materials with these transition metal-pnictide/chalcogenide layers typically feature As and P in the pnictide case and Se and Te in the chalcogenide case with the highest  $T_c$  values being attained with Fe as the transition metal although superconductivity has been achieved with stoichiometric compounds featuring Ru, Rh, Ir and Ni as the transition metal [4].

### 1.1.1 Fermiology of the pnictides

The Fermiology — i.e. the nature of the Fermi surface — is key to the formation of the spin density wave (SDW) state, the onset of which provides the fluctuations necessary for spin-fluctuation mediated pairing and will be described in more detail in the next section. The Bristol group has published a series of results on the Fermiology of various iron-pnictides obtained by de Haas–van Alphen (dHvA) measurements which complement measurements of the Fermi surface by other groups using angle resolved photoemission spectroscopy (ARPES). A summary of some of these measurements are detailed below.

$\text{LaFePO}$ , a member of the 1111 family, has a relatively low superconducting transition temperature of  $\sim 6$  K, nonetheless it is a good example to demonstrate the quasi-cylindrical electron and hole Fermi surfaces typical to the iron-pnictides. Figure 1.1.2 shows the Fermi surface from density functional theory (DFT) calculations using generalised gradient approximation (GGA) with hole pockets centred around  $\Gamma$  and the electron pockets centred around  $M$  (adapted from ref. [8]).

The momentum separated hole and electron pockets are indicative of a semi-metal,

which distinguishes the pnictides from the cuprates\* which are charge insulating antiferromagnets in the undoped state.

The top right two panels of figure 1.1.2 shows slices along the 110 plane through the LaFePO brillouin zone (BZ) which demonstrate how the mean field DFT calculations had to be adjusted by uniformly shifting the energies in each of the bands to match the dHvA measurements. This leads to smaller Fermi surface volumes than the unadjusted GGA calculations.

The LaFePO Fermi surfaces are quasi-2D with only relatively weak energy dispersions in  $k_z$  which are more pronounced for the electron pockets. In contrast, the middle portion of figure 1.1.2 shows the Fermi surface for the non-superconducting 122 family iron-pnictide CaFe<sub>2</sub>P<sub>2</sub> measured by the Bristol group [9]. This also demonstrates semi-metal characteristics but a much stronger  $k_z$  dispersion leading to entirely 3D hole surfaces. In this case the GGA calculations matched the measured dHvA data closely with no energy shifts required.

Comprehensive determination of the Fermi surface of Sr<sub>2</sub>P<sub>2</sub>, another non-superconducting 122 phosphide, also shows 3D hole Fermi surfaces as demonstrated in the bottom row of figure 1.1.2. In this case it was necessary to shift some of the bands from the GGA calculations to match the dHvA data. Here the outer hole pocket is strongly warped along  $k_z$  but does not pinch off as in the CaFe<sub>2</sub>P<sub>2</sub> case, the inner hole pocket after the shift becomes pinched off and fully 3D.

SrFe<sub>2</sub>P<sub>2</sub>, CaFe<sub>2</sub>P<sub>2</sub> as well as BaFe<sub>2</sub>P<sub>2</sub> form the end members of superconducting series that begin with the arsenide counterparts. The arsenide parent compound change from the tetragonal structure to an orthorhombic structure below a characteristic temperature,  $T_s$  which occurs close to a transition from a paramagnetic phase to a stripe SDW state below the Néel temperature,  $T_N$ . This affects the Fermiology by a doubling of the real-space unit cell volume and therefore halving of the BZ volume. The halving of the BZ ‘folds’ the larger zone along the dashed lines illustrated in figure 1.1.3 (a) causing the electron bands in the tetragonal BZ corners to be superimposed on the hole bands around  $\Gamma$  at the BZ centre. Figure 1.1.3 (c) demonstrates how the overlaying of the hole and electron bands in momentum space opens a gap around the Fermi energy and the Fermi surface disappears. In practice, the hole and electron Fermi surfaces are not sufficiently symmetric to perfectly cancel and so several small residual hole and electron pockets are left over. LDA+U calculations and dHvA measurements were performed on BaFe<sub>2</sub>As<sub>2</sub> [12] with the Fermi surface from this publication reproduced in figure 1.1.4. Similar measurements were also performed on detwinned<sup>†</sup> samples of BaFe<sub>2</sub>As<sub>2</sub> by Terashima *et al.* [13] which demonstrated similar small pockets with only small difference in detail.

---

\*Cuprates are the other major class of high- $T_c$  superconductors, see section 1.3 for an introduction.

<sup>†</sup>Similar  $a$  and  $b$  lattice vectors in orthorhombic crystals can lead to imperfections where one region is rotated by 90° with respect to another region. This is known as twinning and when a material which is susceptible to twinning has all the  $a$  and  $b$  axes aligned, the crystal is said to be ‘detwinned’.

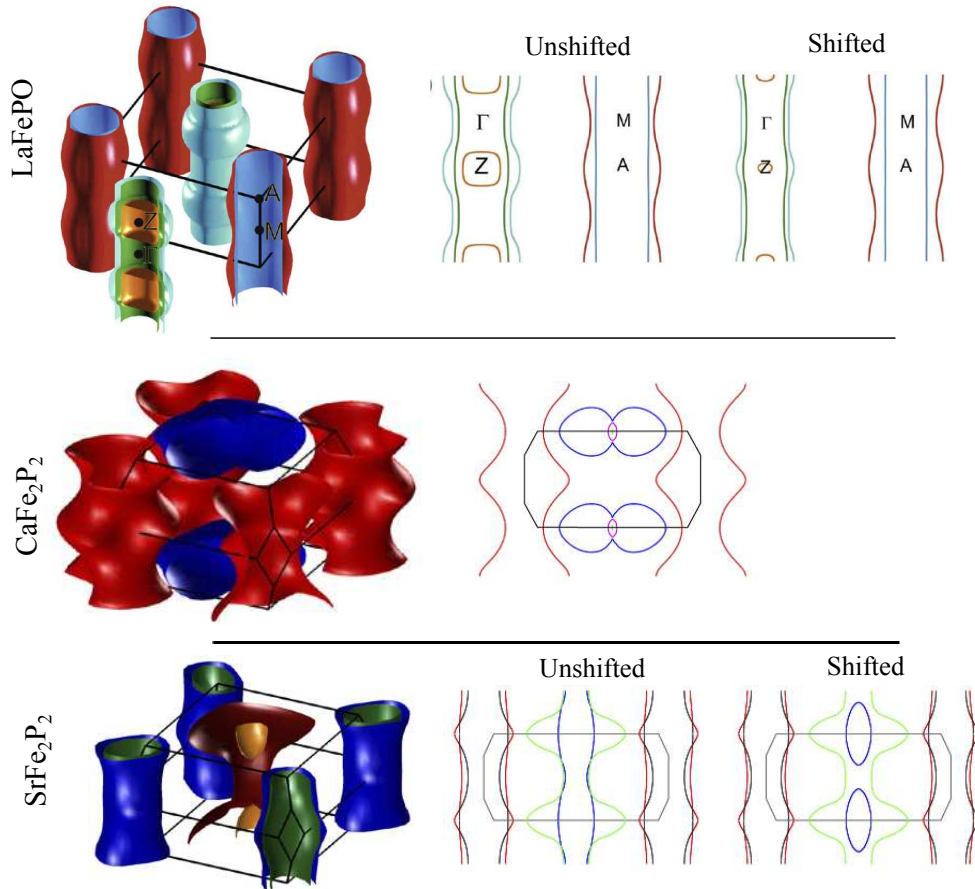


**Figure 1.1.2:** Fermi surfaces of various iron-pnictides from top to bottom: LaFePO (top) with 110 slices of the BZ showing the DFT calculations both before (unshifted) and after (shifted) adjustments to match the dHvA data. CaFe<sub>2</sub>P<sub>2</sub> (middle) with a 110 slice across the Fermi surface. SrFe<sub>2</sub>P<sub>2</sub> (bottom) with 110 slices similar to LaFePO. Adapted from refs. [8–11].

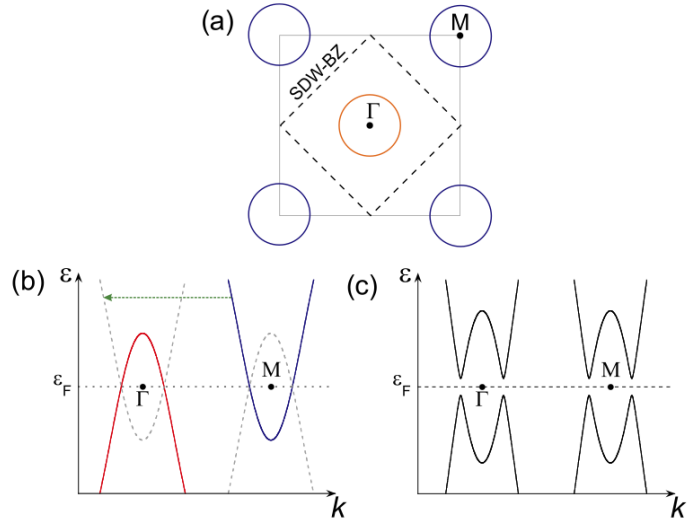


**Figure 1.1.3:** (a) Illustrative 2D projection of the Fermi surface of the tetragonal BZ (solid line) with the reconstructed BZ as a dashed line (b) Schematic semi-metal band structure of the tetragonal phase showing the hole band at  $\Gamma$  and the electron band at  $M$  with the dashed lines showing how the folding of the BZ aligns the hole bands onto the electron bands (c) The folded SDW BZ with the resulting gap at the Fermi energy.

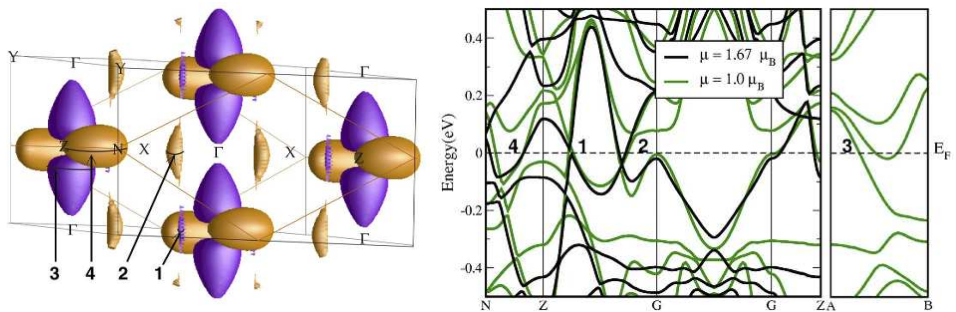


**Figure 1.1.4:** Left:  $\text{BaFe}_2\text{As}_2$  Fermi surface from LDA+U calculations adjusted to fit dHvA measurements. Right: Corresponding band structure showing both with (green) and without (black) corrections to  $U$ .

### 1.1.2 The $\text{BaFe}_2(\text{As}_{1-x}\text{P}_x)_2$ series

The  $\text{BaFe}_2(\text{As}_{1-x}\text{P}_x)_2$  series is one of many that stem from the parent compound  $\text{BaFe}_2\text{As}_2$ , although unlike the electron doped  $\text{BaCo}_{2x}\text{Fe}_{2(1-x)}\text{As}_2$  and the hole doped  $\text{Ba}_x\text{K}_{(1-x)}\text{Fe}_2\text{As}_2$  series, the  $\text{BaFe}_2(\text{As}_{1-x}\text{P}_x)_2$  progression is entirely isovalent meaning that the changes affected due to the P substitution are due to structure and chemical pressure rather than additional charge carriers. Nonetheless, superconductivity occurs with a very similar phase diagram as with the charge-doped examples in the same 122 family of iron-pnictide materials.\*.

At  $x = 0$  the  $\text{BaFe}_2(\text{As}_{1-x}\text{P}_x)_2$  series begins at  $\text{BaFe}_2\text{As}_2$ , a compound which becomes antiferromagnetic at around 138 K, and moves with increasing  $x$  towards  $\text{BaFe}_2\text{P}_2$  which is metallic to low temperatures. Neither end members are superconducting, however as As is substituted for P, the low temperature antiferromagnetic state decays, giving way to superconductivity which kicks in at approximately  $x = 0.18$  and increases to the optimal substitution of  $x = 0.31$ . Superconductivity then decreases until it gives way to a paramagnetic ground state at around  $x = 0.71$ . Figure 1.1.5 shows the phase diagram adapted from ref. [15] as determined by resistivity measurements. Also detailed in the

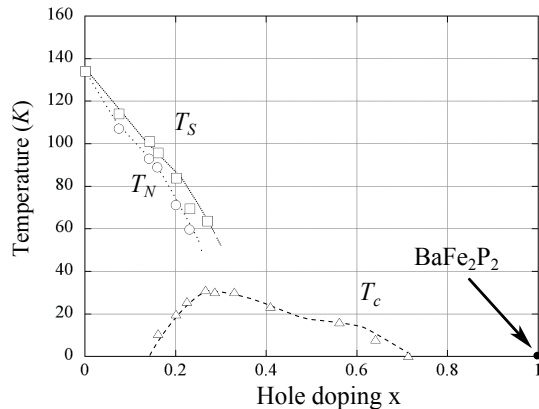


**Figure 1.1.5:** Phase diagram adapted from ref [15] measured by resistivity.  $T_s$ ,  $T_N$  and  $T_c$  are the structural transition, the antiferromagnetic transition and the superconducting transition temperatures respectively.

phase diagram is the structural transition which occurs as the tetragonal  $I4/mmm$  cell moves to an orthorhombic cell as it passes below the line marked  $T_s$ . This coincides with the reconstruction of the Fermi surface detailed in the previous section.

The progression along the series is isovalent since P and As are in the same periodic group – group V. The net effect of the substitution is to apply an increasing chemical pressure as  $x$  moves towards 1. Several reports show that applying high *physical* pressure ( $\sim 5$  GPa) to  $\text{BaFe}_2\text{As}_2$  results in a similar phase diagram with an antiferromagnetic phase

\*See for example figure 1 in ref. [14].

and superconductivity up to  $\sim 30$  K [16–18] with Klintberg *et al.* [19] presenting a direct comparison between the two types of pressure. As pressure is applied, the unit cell  $a$  axis shrinks slightly less than the  $c$  axis ( $\sim 3\%$  cf.  $\sim 4.5\%$  respectively). Interestingly the  $c$  axis shrinking largely occurs in the Fe-Pnictide plane leading to some theories of the superconductivity emerging from the tetrahedral bond angle between the Fe and the pnictogen.

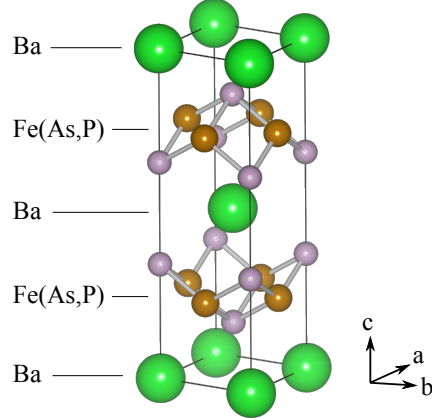


**Figure 1.1.6:** The tetragonal unit cell of the 122  $\text{BaFe}_2(\text{As}_{1-x}\text{P}_x)_2$  series clearly showing the tetragonally bonded  $\text{Fe}(\text{As},\text{P})$  layers.

The Fermiology of the  $\text{BaFe}_2(\text{As}_{1-x}\text{P}_x)_2$  series from a substitution of  $x = 0.41\text{--}1.0$  has been previously measured by members of the group at Bristol using dHvA oscillations [20]. As suggested in the Shishido reference [20], since dHvA has been observed across such a large range of substitutions, it implies that the material is not prone to disorder as is the case in many charge doped series [21] making the series an excellent candidate for dHvA studies. This could be explained by the fact that the substitution is isoivalent and that there is relatively little contribution at the Fermi surface from the pnictide sites\* where the substitution takes place, meaning the Fermi surface should not be strongly disrupted when traversing the series. The Fermi surfaces from the Shishido paper have been characterised for  $x$  ranging from 0.41 to 1 for electron sheets only but have clearly shown that the DFT calculations consistently overestimate the size of the surfaces. They also show a linear progression of the electron orbit sizes which is proportional to  $x$ . Moreover, dHvA measurements on the material with  $x = 0.63$  have been performed where one of the hole surface extrema was observed [22] however DFT calculations as well as comparisons with  $\text{SrFe}_2\text{P}_2$  [11] give evidence for a second hole Fermi surface for materials towards the P end of the series, (towards the As end of the series, there appears this second hole and a *third* hole surface similar but smaller to the other hole sheets). If the electron

\*See for example, the orbital character for the iron sites from DFT calculations presented in figure 4.3.9 in chapter 4.

Fermi surfaces are oversized in the DFT calculations, then the hole Fermi surface volumes should also be oversized in order to remain compensated (electrically neutral). What is not clear though is whether the *shapes* of the hole pockets are also altered in the compounds leading to BaFe<sub>2</sub>P<sub>2</sub>. DFT calculations show the larger of the hole pockets in particular undergoing significant geometric changes, specifically in that it becomes much more three dimensional as P substitution becomes more complete. The Fermi surface of the opposite end-member, BaFe<sub>2</sub>As<sub>2</sub>, has been fully characterised by previous ARPES measurements [23] and dHvA [12, 13]. Intermediate unreconstructed superconducting compounds have been partially characterised by dHvA [22] and ARPES [24]. Coupled with a full characterisation of the Fermiology of BaFe<sub>2</sub>P<sub>2</sub>, this unreconstructed Fermi surface data can be used to interpolate the Fermiology of the hole pockets across the portion of the phase diagram outside of the SDW state.

The ARPES measurements of the Fermi surface of BaFe<sub>2</sub>As<sub>2</sub> below the Néel temperature concluded that despite some  $k_z$  dispersion in the Fermi surfaces, there is adequate nesting to form the antiferromagnetic state. Ab-initio DFT calculations [20] of the paramagnetic state have shown the  $k_z$  dispersion increasing with increasing P, with the outer hole pockets becoming more three-dimensional through the progression providing the partial nesting conditions necessary for pair forming SDW fluctuations described in section 1.2\*

## 1.2 The high- $T_c$ pairing mechanism

The previous section discusses the Fermiology of the iron-pnictides but does not make any statements as to why this is important to the high- $T_c$  problem. In particular how does Fermiology relate to the mechanism which causes the Cooper pairs to couple — the so called ‘pairing glue’.

The charge carrier in a superconducting condensate is a Cooper pair - a quasi-particle comprising of a bound state of two electrons or two holes with opposite momentum and, in the singlet case, opposite spin. Evidence for this configuration can be shown from the Ginzburg-Landau model which, when applied to a superconducting system, gives the charge of the quasi-particle carriers as  $2e$ , where  $e$  is the charge of an electron [25]. Given that due to their like charges two free electrons repel, it is natural to ask what could overcome the electromagnetic force to cause these electrons to remain bound in this quasi-particle state.

Bardeen, Cooper and Schreiffer established much of the theoretical basis — from which the Ginzburg–Landau model can be derived — in Bardeen-Schreifer-Cooper (BCS) *theory* (named after the authors). Within the framework of BCS theory, Bardeen Cooper and Schreiffer wrote a 1957 paper [26] detailed a pairing mechanism known as the BCS *model*

---

\*These calculations do not take into account the reconstruction below  $T_s$  however for low  $x$ , and instead assume a hypothetical non-magnetic order.

which would explain how these electron remained bound together. The model is based around the concept of phonons scattering off electrons which well suited the superconducting materials known at the time. Phenomenologically, the mechanism of attraction is straightforward. Electrons moving through a crystal lattice attract ions on the lattice sites. These heavy ions respond slowly and are drawn in *behind* the electron. This has the effect of both screening the negative electron charge as well as providing an attractive positive potential for any electron following the original electron. The net effect is the leading electron draws the following electron in its wake, thus coupling them with one another. The wavelike distortion of the ions in the lattice can be considered as a phonon, and the interaction between the electrons and the lattice can be modelled as electron–phonon–electron scattering.

The BCS model accurately describes what we now know as ‘conventional superconductivity’, that is pairing which forms a spin-singlet state ( $S = 0$ ) and which has zero orbital angular momentum ( $L = 0$ ). It was not until the discovery of superfluidity\* in  $^3\text{He}$  in 1972 [27] that it became apparent that there may exist forms of pairing that resulted in spin-triplet pairing state ( $S = 1$ ) with  $L > 0$ . This was later confirmed when superconducting analogues were found in the form of heavy Fermion materials. What really spurred the explosion in interest though was the 1986 discovery by Bednorz and Müller [28] of high transition temperature ( $T_c$ ) superconductivity in the cuprates and, more recently, the ‘pnictides’ by Kamihara *et al.* [2]. The cuprate class of materials that Bednorz and Müller found to be superconducting have transition temperatures far in excess of any previously known superconducting materials and although the BCS model phonon pairing may play a part, the predominant pairing mechanism in the high- $T_c$  materials is likely to be something else entirely.

### 1.2.1 The case against conventional superconductivity in high- $T_c$ materials

There is a great deal of evidence in the literature for non-BCS model pairing in the high- $T_c$  and heavy Fermion materials. Although the pairing wavefunction cannot be measured directly with current techniques, experiments indirectly infer ‘unconventional’ i.e. non  $s$ -wave, BCS-model, characteristics. For example, analysis on penetration depth measurements of  $\text{YBa}_2\text{Cu}_3\text{O}_y$  (YBCO123) show power law behaviour [29], indicating that there exists states within the momentum averaged gap. SQUID measurements and Josephson tunnelling experiments on the same material have confirmed alternating phase of the condensate wavefunction which points strongly to  $d_{x^2-y^2}$ -wave symmetry [30] (see also refs. therein). As for other cuprate materials, specific heat measurements on BSCO2201 [31],

---

\*Superfluidity and superconductivity share much of the same physics although the superfluid  $^4\text{He}$  molecules are already bosons and so pairing is not required. Parallels between the two are discussed in ref. [25].

as well as penetration depth measurements on LSCO [32] have also proved consistent with  $d$ -wave pairing.

More evidence against conventional superconductivity include the unusual normal state (i.e. non-superconducting) state properties of the cuprates and heavy Fermion materials. The BCS model is grounded in Landau Fermi liquid theory which models interacting itinerant electrons with quasiparticles of heavier effective mass than ordinary electrons and holes. A hallmark of Fermi liquid behaviour is a  $T^2$  dependence of the resistance, however experiments on the cuprate  $\text{La}_{2-x}\text{Sr}_x\text{CuO}_4$  (LSCO) [33] and a heavy Fermion material [34] have demonstrated fractional power law behaviour,  $T^\gamma$  where  $1 < \gamma < 2$ , at temperatures above the superconducting transition. Given that the Fermi liquid model breaks down in these examples, it follows that the BCS-model also is likely on shaky ground for these materials.

There are several arguments against phonons as the sole pairing mechanism in the pnictide case, Boeri *et al.* [35] and Mazin *et al.* [36] present calculations showing that the magnitude of the electron-phonon coupling is not adequate for the high  $T_c$  values attained in LaFeAsOF, Haule *et al.* [37] note in the same material that the gradient of the density of states (DOS) at the Fermi level is such that you would expect an increase in DOS and hence  $T_c$  with hole doping if the BCS model held, however the reverse is true. Non Fermi-liquid behaviour was demonstrated in the  $\text{BaFe}_2(\text{As}_{1-x}\text{P}_x)_2$  series [38, 39] and although many superconducting pnictides are believed to have a nodeless superconducting gap [40–43] there are many [40, 44–47] including the  $\text{BaFe}_2(\text{As}_{1-x}\text{P}_x)_2$  series [48–50] which are thought to have nodes.

It is interesting to note that unlike the cuprates which universally show a  $d_{x^2-y^2}$  gap symmetry, the pnictide materials are not all alike, even pnictides along the same series such as the LiFeAs and LiFeP show a change in gap structure. Consequently, it may prove that the nature of the superconductivity may not be universal amongst the pnictide materials. Irrespective of this, the BCS model pairing alone has been shown to be too weak to explain high- $T_c$  superconductivity.

### 1.2.2 Spin-fluctuations

One possible alternate pairing mechanism arises from scattering due to spin fluctuations. A common feature of phase diagrams for all of the pnictides and the cuprate materials is close proximity of an antiferromagnetic state to the superconducting state as shown in figure 1.2.1. The SDW state, described in more detail in section 2.4, is a general form of magnetic order that describes a periodic modulation of the spins of a system and encompasses antiferromagnetism and arguably ferromagnetism. In a system close to a SDW state, short range, damped, antiferromagnetic fluctuations occur and it is these that are thought to provide the pairing interaction for the Cooper pair states.

Spin fluctuations were originally investigated as a mechanism which *suppressed* con-

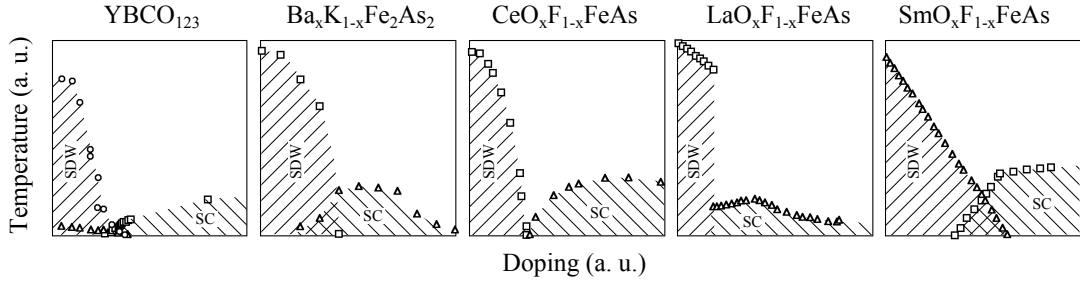


**Figure 1.2.1:** Phase diagrams for various high- $T_c$  materials adapted from ref. [51] showing the proximity of the superconducting phase (SC) to the spin density wave state (SDW) in all cases.

ventional, i.e. *s*-wave, superconductivity [52] from ferromagnetic fluctuations and were used to explain why nearly ferromagnetic metals such as Pd has lower than expected  $T_c$ . Later however it was found that in certain regions in real space, for example that satisfy *d*-wave symmetry, that *antiferromagnetic* spin fluctuations could possibly provide an interaction which is attractive and could overcome the Coulomb repulsion [53].

As we will see in section 2.4, a free electron gas is unstable to the ferromagnetic state, however with favourable band structure conditions, in particular where there is a ‘nesting’ condition, an antiferromagnetic SDW may occur. Nesting is where a Fermi surface in one region of the BZ maps through reciprocal space onto another similarly sized and shaped Fermi surface in another region of the BZ via a particular vector  $\mathbf{q}$  known as the nesting vector. Since strong nesting leads to a stable SDW state, we are looking for only partial nesting in the Fermi surface of superconducting materials so that we get enough spin fluctuations to cause pairing but not too many to cause a full SDW state. A fuller discussion of the mechanism of pairing due to spin density wave fluctuations is detailed in section 2.4.

As an aside, nesting is not the only cause of spin fluctuations. For example, frustrated spin systems such as the Kagome triangular lattice can also be a cause of spin fluctuations, however this is thought to occur only in very specific 1D and 2D materials.

### 1.2.3 Pairing in the pnictides

Soon after the discovery of the pnictide materials, a possible pairing mechanism was proposed based on the above described spin density wave fluctuations. The original paper suggested a  $s_{\pm}$  gap symmetry [36] which features a multi band model based on LaFeAsO<sub>1-x</sub>F<sub>x</sub> which matches the semi-metal bandstructure discussed earlier. The spin fluctuation couples over the BZ diagonal two separate, approximately cylindrical, Fermi surfaces of opposite phase.

This is an extended *s*-wave model which satisfies the requirement for opposite phase by having two separate Fermi surfaces of opposite phase which are partially nested. However

as already stated, more recent measurements have discovered nodes in the gap structure in many pnictide materials. While no nodes featured in the original Mazin model, the *s*-wave symmetry allows nodes. However the *d*-wave state *requires* nodes and given that, as already stated, some pnictides are nodeless, the *d*-wave symmetry cannot be the correct pairing symmetry across all the pnictide materials [54].

#### 1.2.4 Motivation for dHvA measurements on BaFe<sub>2</sub>P<sub>2</sub>

In order to explore the role of nesting in the high- $T_c$  superconductors, an investigation at Bristol was undertaken on the Fermiology of the BaFe<sub>2</sub>(As<sub>1-x</sub>P<sub>x</sub>)<sub>2</sub> series by studying angle resolved dHvA oscillations. This thesis details results in particular on the end-member, BaFe<sub>2</sub>P<sub>2</sub>. The results elucidate the nature of the hole pockets which according to the DFT calculations change topologically much more than the electron pockets throughout the series. This will also provide an interesting comparison to recent measurements on the structurally similar compound SrFe<sub>2</sub>P<sub>2</sub> and CaFe<sub>2</sub>P<sub>2</sub>.

We seek to examine if partial nesting is found between the outer hole surface and the inner electron surface with  $q = (\pi, \pi, \pi/2)$  meaning the nesting phenomenon persists through to the end member of the series despite the fact that superconductivity is not observed beyond a phosphor content of around  $x = 0.71$ . We also seek to measure the effective masses of the hole pocket in particular to see if they greater than the relatively weak mass enhancements from the electron pockets thereby indicating stronger electron correlations on the hole sheets. These investigations are undertaken in chapter 4.

The investigations described here are undertaken in chapter 4. The samples were grown by our collaborator T. Shibauchi in Kyoto university. Prof. A. Carrington performed the x-ray characterisation with Dr. I. Guillamon and Dr. M. Haddow. Prof. A. Carrington also mounted the sample on the cantilever and performed initial DFT calculations which were repeated by the author. The measurements in the ‘Yellow magnet’ and analysis were performed by the author with consultation from Prof. A. Carrington and using MATLAB scripts adapted from code originally written by Dr. E. Yelland. The MATLAB susceptibility code was written by the author.

### 1.3 The cuprate phase diagram

The second half of this thesis concerns the nature of the phase diagram of the high- $T_c$  cuprate materials and understanding the mechanisms at play. As shown in figure 1.2.1 the phase diagrams for the pnictide materials vary somewhat in their composition but in the cuprate case, as exemplified by YBCO123 in figure 1.2.1, the hole doped cuprate phase diagrams are remarkably consistent with the chief differences being quantitative in nature. However this ‘universality’ amongst the cuprate phase diagrams comes with an abundance

of features which provide for some complex physical interactions and fragile intermediate ‘crossover’ phases.

The tuning parameter for the cuprate phase diagram is either electron or hole doping typically performed by elemental substitution at the crystal growth stage or by oxygen incorporation through annealing. As shown in figure 1.3.1, the two types of doping are not symmetric with hole doping generally resulting in more robust superconductivity. For this reason the literature has largely concentrated on the hole doped progression and as a result it is far better characterised. The doping is usually expressed as a  $p$  value which represents the amount of additional holes (or electrons) per Cu atom.

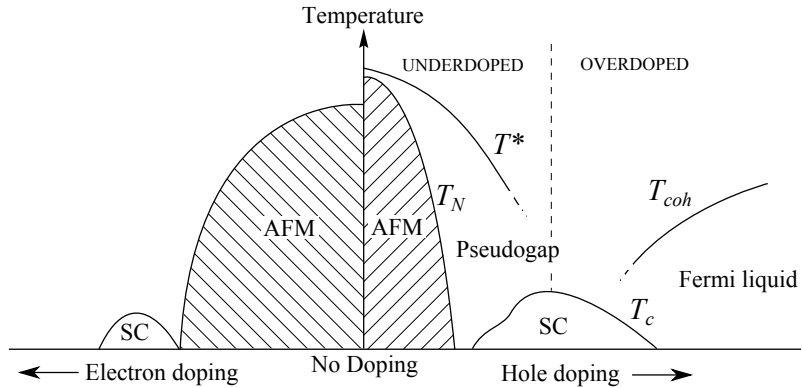


**Figure 1.3.1:** A schematic phase diagram showing electron doped to the left and hole doped to the right. AFM is the antiferromagnetic charge transfer insulator phase, SC is the superconducting phase.  $T^*$ ,  $T_N$ ,  $T_c$  and  $T_{coh}$  are the temperature scales for the pseudogap, AFM state, superconductivity and coherent Fermi liquid phases respectively. Sketch loosely based on ref. [55].

### 1.3.1 Charge transfer insulator parent compound

Starting with the undoped state in figure 1.3.1, the parent compound materials at zero doping are thought to be charge transfer insulators i.e. the top most filled state on each lattice site contains one electron. In the conventional band picture this should be metallic since the bands are only partially filled, however when we consider a localised picture of electrons where electrons are confined to lattice sites, any movement of an electron to the neighbouring lattice site will cause an energetically costly double occupancy on one site and zero occupancy on another. This causes the electronic density of states (DOS) to become gapped around the Fermi surface and hence suppressed conduction leading to a splitting of the conduction band and an energy gap hence the insulating behaviour.

This is most simply captured in the Hubbard model which encapsulates the charge hopping concept in a two term Hamiltonian. In the ‘single-band’ case\* one term represents the hopping amplitude,  $t$  and another representing the cost for double occupancy,  $U$ .

\*which actually refers to the fact that each atom has one ‘orbit’ allowing for a maximum occupancy of two electrons [56].

At half filling, the conduction band is split by energy  $U$  so that half the states are above the chemical potential and half are below. If the lower of the split conduction band is below a band of another orbital character, a charge insulator state is realised and any hopping of electrons is predominantly between bands of a different orbital character within the same real-space unit cell. Otherwise if the chemical potential lies directly between the split conduction band, a Mott insulating state is realised and electron hopping predominantly occurs between unit cells.

The  $t$  term is reduced when the ordering of the sites is antiferromagnetic since for any hopping to occur at all, the spins must be antialigned to avoid double occupancy of like spins. This region dominates the low doping portion of the phase diagram and remains antiferromagnetic until either the temperature is high enough to allow transitions from the Fermi energy to the states at the edge of the gap or the doping has introduced enough double occupancy holes (or electrons) on lattice sites, which can move without the double occupancy energy cost, to overcome the insulating behaviour.

### 1.3.2 Superconducting dome

With increased doping, the antiferromagnetic state gives way to the superconducting dome at around  $p = 0.05$  which itself gives way to a Fermi liquid metallic state at a doping of around  $p = 0.3$ . The maximum  $T_c$  occurs at around  $p = 0.16$ . Temperature driven transitions from both the antiferromagnetic and the superconducting state are clearly second order thermodynamic phase transitions with jumps in the heat capacity for example, however there are other regions in the phase diagram which are less well defined such as the pseudogap and the Fermi liquid crossover whose temperature scale can depend on the particular probe used and do not have a clear order parameter.

### 1.3.3 Coherent phase

To the heavily overdoped side of the phase diagram, beyond the superconducting dome lies the coherent region delimited by  $T_{coh}$  where the system bears the hallmarks of a ‘conventional’ metal. More specifically this is defined as the region where  $\Sigma'' \propto \omega^2$  which falls in line with Landau Fermi liquid theory, the standard theory used to model conventional metals\*. This is in contrast to the broadly funnel shaped region above and between  $T_{coh}$  and  $T^*$  where  $\Sigma'' \propto \omega$  and is sometimes known as the ‘strange metal’ region.

The implication is that correlations between electrons are sufficiently weak such that the mass enhanced quasiparticles of Landau’s Fermi liquid theory are well defined, leading to conventional metal behaviour. A clear indication of this is a dominant  $T^2$  term in the resistivity. In the region above  $T_{coh}$  we observe an anomalous additional  $T$ -linear

---

\* $\Sigma''$  is the imaginary part of the self energy which relates to the quasiparticle lifetime (and scattering rate) and  $\omega$  is the excitation energy which is related to  $T$ . For more on Landau Fermi liquids see section 2.2.

contribution high above the Debye temperature typical for cuprates meaning that it is unlikely to be due to electron-phonon scattering. The confinement of this  $T$ -linear region to above the superconducting dome has been observed in heavy Fermion materials [34] and is often associated with proximity to a quantum critical point (QCP) [57].

### 1.3.4 The pseudogap

Above the antiferromagnetic region and the superconducting state is one of the most controversial regions of the phase diagram, the so called pseudogap phase. This is a region which was first demonstrated in 1989, just a few years after the discovery of the cuprate materials, by nuclear magnetic resonance (NMR) measurements performed at Bell labs [58]. A noticeable fall in the susceptibility occurs at a temperature significantly above  $T_c$  which led to conclusion of possible spin pairing before the onset of bulk superconductivity\*. The question arose as to what the exact relation of the pseudogap is to the superconducting state — is it a precursor state, from which superconductivity arises or is it a competing phase? — and from a materials development point of view, to obtain higher  $T_c$  should we be finding ways to suppress the crossover to the pseudogap state or encourage it? By

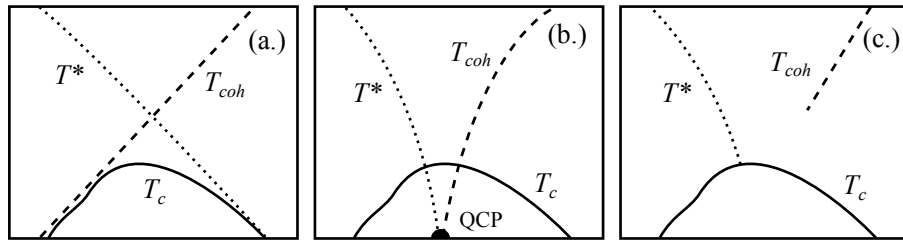


**Figure 1.3.2:** Three scenarios proposed for the  $T^*$  temperature scale behaviour. (a.) the pseudogap as the ‘precursor’ state, (b.) as the ‘competing’ state, (c.) and the ‘transition’ scenario.

finding where exactly the  $T^*$  energy scale meets the superconducting dome, strong evidence can be found that supports one or the other scenario. However the problem lies in the type of probe used. Select spectroscopic measurements including scanning tunneling microscopy (STM), ARPES and Raman spectroscopy on materials of comparable  $T_c$  values have found that the  $T^*$  overreaches the superconducting dome entirely [60], meeting with the overdoped edge at  $T = 0$  K. This supports the precursor state theory illustrated in figure 1.3.2 (a.) where  $T^*$  and  $T_{coh}$  cross to define a region which is below both temperature scales where the carrier are both coherent quasiparticles and paired leading to the superconducting condensate.

A second scenario is supported by measurements using bulk probes such as heat capacity, magnetic susceptibility and resistivity measurement have shown the  $T^*$  energy scale

\*Cooper paired electrons in the singlet state have zero net spin hence they do not contribute to the susceptibility, whereas unpaired electrons do. Cooper pairing leads to a reduction in susceptibility, see for example neutron scattering chapter by S. M. Hayden in ref. [59].

drops into the top of the superconducting dome [61]. This supports the scenario where the pseudogap is in competition with superconductivity for states at the Fermi surface. Once the pseudogap phase is suppressed, scattering from quantum fluctuations at zero temperature leads to the formation of the superconducting phase at a QCP similar to that found in heavy fermion materials. This scenario is supported by the observation of linear scaling of the resistivity with temperature in the region above the superconducting dome which is a hallmark of proximity of a QCP.

A third scenario is one where the pseudogap simply becomes the superconducting gap as it meets the top of the superconducting dome. However this scenario leaves hanging questions as to the roles of the pseudogap,  $T_{\text{coh}}$  and other phenomena in the phase diagram which would need to be addressed theoretically. Moreover this picture is rendered less compelling by the observation in LSCO of rapidly increasing, low temperature, normal state resistivity inside of the underdoped superconducting dome which implies the non-superconducting energy gap persists into this region.

### 1.3.5 Stripe order Fermi surface reconstruction

A second contentious region occurs on the underdoped side of the superconducting dome. Stripe order — i.e. one dimensional charge ordering — has long been known about in this region in LSCO [62], however LeBoeuf *et al.* in a recent paper [63] discusses how low temperature Hall data in YBCO123 can be interpreted in terms of a Fermi surface reconstruction at  $p = 0.08$  between two different Fermi surface topologies — both of which feature stripe order and how stripe order may be more general to the cuprates\*. Figure 1.3.3 illustrates the proposed reconstruction where the mobile electron pockets at

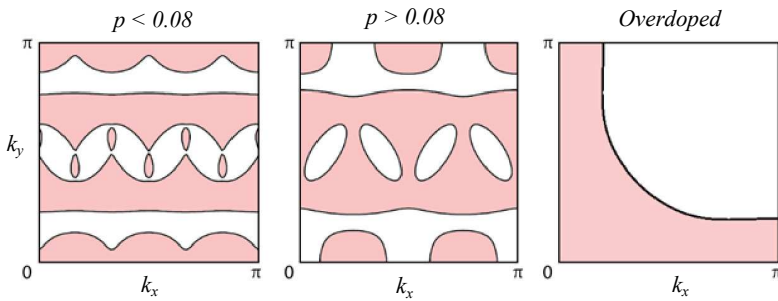


**Figure 1.3.3:** Schematic representation of the reconstruction thought to occur at  $p = 0.08$ . Shaded region are occupied. Adapted from ref. [64]

the top and bottom of the plot at  $p > 0.08$  undergo a so called Lifshitz transition and merge into 1D stripes at  $p < 0.08$ . Evidence for this is provided in the form of low temperature

---

\*This proposed reconstruction is separate to the more dramatic Fermi surface reconstruction which is thought to occur between the large hole-like Fermi surface on the overdoped side (right panel fig. 1.3.3) and the stripe order phase on the underdoped side (left and centre panel, fig. 1.3.3).

Hall data where, for  $p > 0.08$ ,  $R_H$  is found to drop from positive at high temperatures to negative at low temperatures which is attributed to the formation of the stripe phase with highly mobile electron pockets (hence the negative  $R_H$  at low  $T$ ). For  $p < 0.08$ ,  $R_H$  still drops but remains positive for all temperatures which the author attributes to a different Fermi surface topology which no longer features the small highly mobile electron pockets.

However, as we shall see in the next section, an alternative explanation for the low temperature Hall behaviour is suggested based on the anisotropic scattering rate observed in Sr doped  $\text{La}_{2-x}\text{Sr}_x\text{CuO}_4$  (LSCO).

### 1.3.6 Previous work by the Bristol group

Clearly lots of interesting physics is occurring in and around the superconducting dome and a solid understanding of this region is key to understanding the problem of high- $T_c$ . Prof. N. Hussey has been involved in many efforts to shed light on the situation and has described how an usual anisotropic scattering term in the resistivity can be explain much of the unusual behaviour in the cuprates [57, 65, 66]. A summary of the work relevant to this thesis is presented below.

#### Links between anisotropic scattering and $T_c$

Simply measuring resistance along different axes gives an averaged scattering rate through all conduction paths and so to build a map of the angle dependent scattering rates, a different technique must be used. In angle dependent magnetoresistance (ADMR)\* a strong persistent magnetic field is applied before resistance measurements are taken. The field serves two purposes; firstly, to suppress superconductivity so the normal state can be probed, secondly to confine the electrons to orbits perpendicular to the field. By detailed analysis of the change in resistance as the field is applied at various angles, a picture of the angle dependent scattering rate can be determined.

After performing measurements on samples of Tl2201 with dopings ranging from strongly overdoped to slightly underdoped [67], a trend emerged which is illustrated in figure 1.3.4. Here the scattering rate within the  $ab$ -plane,  $\Gamma$ , was found to be composed of two terms; an isotropic term which remained constant with doping (dotted circle) and an anisotropic component which scaled with the superconducting gap,  $\Delta_g$  (solid line). Moreover it was found that the superconducting gap and the anisotropic scattering rate both shared the same shape, ('d-wave'), and orientation (aligned with the CuO bonds) which suggests that the anisotropic term may be linked with the exotic superconductivity.

Evidence for the anisotropic scattering term has also been found in ARPES measurements. In underdoped samples, Fermi surface spectral weight that coincides with the

---

\*Some older literature labels the technique as a measurement of angle-dependent magnetoresistance oscillations (AMRO), however ADMR is the current preferred term now.

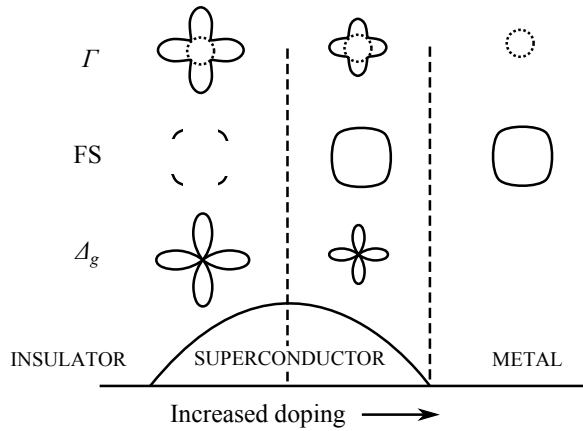


**Figure 1.3.4:** Schematic of how the scattering rate,  $\Gamma$ , the Fermi surface,  $FS$ , and the superconducting gap,  $\Delta_g$  evolve with doping across the superconducting dome. Based on figure 1 in ref. [68]. The dotted line in the scattering is the isotropic part.

antinodal points of  $\Gamma$  (and  $\Delta_G$ ) disappears [69] i.e. coherent particles are lost in the regions of strong scattering.

Further transport measurements which used high magnetic fields to suppress superconductivity and measure resistivity inside the superconductivity dome have also uncovered an unusual  $T$ -linear term. The measurements showed that the  $T$ -linear term did not funnel down to a point (figure 1.3.5) as is typical of QCP behaviour in, for example, the heavy Fermion materials [34] but instead spread out into the superconducting region in a ‘foot’ shape [33]. This behaviour is highly remarkable since it does not follow either of the usual

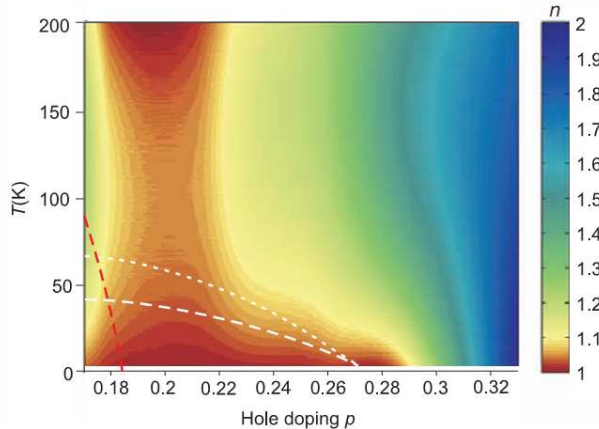


**Figure 1.3.5:** Plot of the  $T^n$  term in the fitted field suppressed normal state of Sr doped LSCO showing the  $T$ -linear term extending throughout the superconducting dome and not to a single QCP. Taken from Cooper *et al.* [33]

expected BCS behaviour (given the ‘strange metal’ scattering dependence) or the expected QCP behaviour (since it does not funnel down to a single QCP at  $T = 0$  K). As of yet,

this highly unusual behaviour is still not fully explained and has so far this has only been observed in LSCO. LSCO is known to be in close proximity to a van-Hove singularity\* in this region at  $p \approx 0.18$  [70] and so it begs the question as to whether this is an effect due to the proximity of the singularity or something more general to the cuprates.

#### Links between anisotropic scattering and low temperature Hall behaviour

Narduzzo *et al.* [71] used the anisotropic scattering rate to successfully explain the temperature dependence of the Hall behaviour in Sr doped LSCO which did not require the invocation of any Fermi surface reconstruction scenarios as described in section 1.3.5. Through appropriately curved Fermi surfaces — described in more detail in section 2.6.1 — the anisotropic scattering can cause  $R_H$  to become negative at low  $T$  even with an ostensibly large, hole-like Fermi surface similar to that observed in the overdoped regime.

So far, this has only been demonstrated in LSCO [71] and in order for it to be a viable explanation for the low temperature Hall behaviour in the cuprates, it will need to be demonstrated in other cuprate materials.

## 1.4 Properties of BSCO2201

The unit cell of the high- $T_c$ , doped cuprate  $\text{Bi}_{2+z-y}\text{Pb}_y\text{Sr}_{2-x-z}\text{La}_x\text{CuO}_{6+\delta}$  (BSCO2201) is illustrated in figure 1.4.1. It is made up of layers as follows from the top; a BiO layer, then a SrO layer, then a CuO layer common to all cuprates, then two BiO layers, a SrO layer, a CuO, SrO and a BiO layer. Variants of BSCO2201 include  $\text{Bi}_2\text{Sr}_2\text{Ca}_1\text{Cu}_2\text{O}$  (BSCO2212) and  $\text{Bi}_2\text{Sr}_2\text{Ca}_1\text{Cu}_3\text{O}$  (BSCO2213) which feature one and two extra CuO layers respectively. Most closely related in terms of structure is Tl2201 which features Tl and Ba in place of Bi and Sr respectively. BSCO2201 is orthorhombic with  $a = 5.362(3)$  Å,  $b = 5.374(1)$  Å and  $c = 24.622(6)$  Å [72], Tl2201 on the other hand has  $a = 5.4580(3)$  Å,  $b = 5.4848(5)$  Å and  $c = 23.2014(5)$  Å [73]. Undoped BSCO2201 has an excess of holes and lies slightly to the underdoped side of the phase diagram. By substituting in La for Sr, the amount of holes is reduced allowing access to a range of slightly overdoped to underdoped. However, since the substitution takes place adjacent to the CuO planes where all the interesting electronic behaviour happens, La doping introduces a lot of disorder into the system. Pb is also substituted for Bi which increases the number of holes allowing the more overdoped region to be accessed. Since Pb substitutes into the BiO layer which is far from the CuO plane, less disorder is introduced. Sometimes Pb is introduced alongside La even when a more underdoped state is desired to avoid forming structures in the BiO planes which affect ARPES measurements [74]. Furthermore, annealing in oxygen decreases the number of carriers depending on how much additional oxygen is absorbed allowing for even more

---

\*A spike in the DOS brought about by a flat region of the bandstructure at the Fermi level.

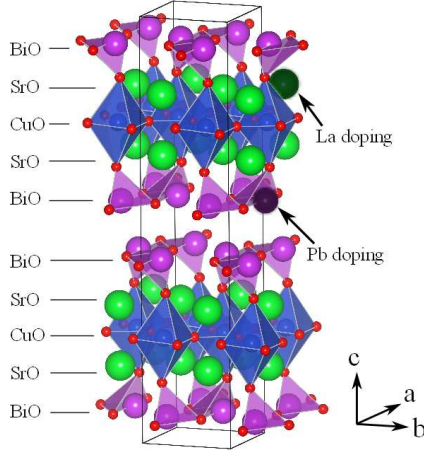


**Figure 1.4.1:** Unit cell of BSCO2201 demonstrating the layers. Tl2201 is similar but with La for Bi and Ba for Sr. Note that Pb doping occurs away from the CuO planes.

fine grained tuning of the doping. By adjusting these parameters a very wide range of doping values can be accessed in BSCO2201 which makes it appealing for study.

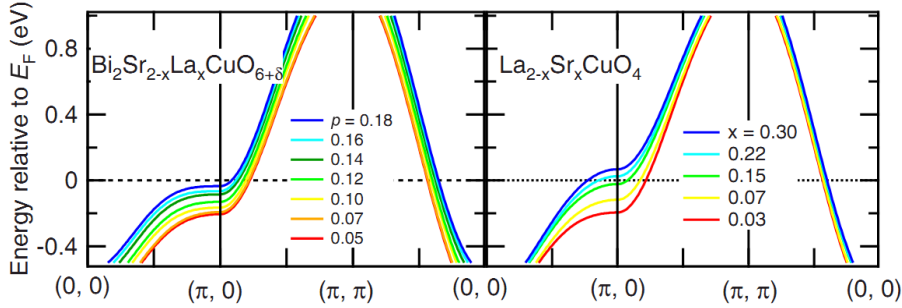


**Figure 1.4.2:** Band dispersions at the Fermi energy for various dopings. Left panel shows BSCO2201, right panel shows LSCO. Note the saddle points at  $(\pi, 0)$  which cause the van-Hove singularity at  $p \approx 0.18$  for LSCO and at  $p \geq 0.2$  for BSCO2201. Adapted from ref. [70].

### 1.4.1 Fermiology of BSCO2201

There is a crossover in overdoped cuprates between a large hole-like Fermi surface to an electron-like Fermi surface that leads to a saddle point in the DOS and consequently a van Hove singularity as shown in figure 1.4.2, which is adapted from ARPES results from ref. [70]. This occurs in LSCO at around  $p \approx 0.18$  which is approximately critical doping and may lead one to believe that the critical behaviour is related to the proximity of the van Hove singularity. However the same crossover does not happen at the same doping in BSCO2201, rather it appears to occur at  $p \geq 0.2$ , relatively far from the critical value of  $p \approx 0.16$ . For this reason BSCO2201 is an attractive material to study to determine more

about the relationship (or lack thereof) between the critical behaviour and the van Hove singularity.

### 1.4.2 Determining the doping

The precise determination of doping from a chemical standpoint is tricky. For LSCO — assuming pure ionic donation — substituting more Sr for La simply adds one more hole per extra Sr atom per unit cell. However for YBCO123 and  $\text{YBa}_2\text{Cu}_4\text{O}_y$  (YBCO124) for example, there exist CuO chains (oxygen deficient CuO layers) which absorb some of the doped charge, in other cuprates the heavy metal atom has a mixed valency meaning that the substitution relation is not so straightforward. Various techniques are employed to determine the doping level but as a rule some a priori knowledge of composition is required.

Typically BSCO2201 doping is determined by matching the  $T_c$  normalised to the maximum  $T_c$  to a ‘universal’ parabola determined by Presland *et al.* [75] or more recently by comparing Hall data to the well defined doping of LSCO [76]. However there are concerns as to whether it is appropriate to compare BSCO2201 to LSCO when it comes to the Hall data in the overdoped side of phase diagram due to the proximity of the van-Hove singularity.

However, recently the doping of Tl2201 in overdoped samples was well characterised by dHvA measurements of the Fermi surface [77] which through the Luttinger sum rule, based on the size of the Fermi surface volume, assigned higher dopings to the Tl2201 samples than samples of LSCO of comparable  $T_c$ . Given that structurally, BSCO2201 is much more similar to Tl2201 than LSCO and Tl2201 is also not in immediate proximity to the van-Hove singularity, it may be preferable to compare the  $R_H$  values in BSCO2201 to Tl2201 using a method similar to that used by Ando *et al.*

### 1.4.3 Motivation for high-field transport measurements on BSCO2201

Original motivation for the high field transport measurements on BSCO2201 was to recreate the magnetoresistance measurements performed on LSCO on a different material which is not so close to a van-Hove singularity to elucidate whether the highly unusual ‘foot’ shape for the  $T$ -linear region is specific to LSCO or more general to the cuprates. Moreover BSCO2201 allows for wider doping into the underdoped region — resistivity in LSCO diverges on the underdoped side at low temperatures — and so will allow us to observe how the progression continues. BSCO2201 also demonstrates transport behaviours which are consistent with other high- $T_c$  cuprate materials, for example, from resistance measurements it demonstrates a similar maximum in the underdoped  $d\rho_{ab}/dT$  curve as underdoped YBCO [78] and on the overdoped side, BSCO2201 demonstrates a monotonic upward trend in  $d\rho_{ab}/dT$  with increasing temperature similar to what has been observed in Tl2201 and

LSCO [78].

During the course of the investigations however, it became apparent that even with field strengths of up to 60 T in pulsed fields, the upper critical field,  $H_{c2}$  of many of the samples at key temperatures could not be reached despite their relatively low  $T_c$  which would imply narrower fluctuation regimes. However, field strengths were generally strong enough to recover  $B$ -Linear behaviour in the Hall component.

By examining the temperature dependence of Hall data down to 1.4 K in BSCO2201 we can determine if a model based on the Ong construction and anisotropic scattering can explain the low temperature Hall behaviour in BSCO2201 similar to what was shown for LSCO [71]. This will help determine whether the geometric arguments provided by Ong apply more generally to the cuprates and whether it is therefore necessary to invoke the complex Fermi surface re-construction scenario described by LeBoeuf *et al.* to describe the behaviour of  $R_H$  in the cuprates.

Previous Hall measurements have been performed on BSCO2201 by Ando *et al.* [76, 78] which are shown for comparison in the results section [78]. However these results do not go to low temperatures, being restricted by the onset of superconductivity. Our own results used high field measurements at LNCMI and HFML to suppress superconductivity and examine the low temperature regions in detail. Moreover our samples are focused on the overdoped region which complements the underdoped data set presented in the Ando and Balkirev papers [79].

Furthermore, we can study the Hall effect to investigate the doping determination according to Tl2201 described previously. We compare the data with results from ARPES by our collaborators on the samples from the same batch which determine the doping directly, rather than inference through comparison to Tl2201, by measuring the size of the Fermi surface within the BZ [80]. The investigations described in this section are presented in chapter 5.

The samples were grown by Prof. Takeuchi's group in Sendai University, Japan in May 2009. The high field data was obtained on three separate occasions. The first LNCMI, Toulouse results were obtained by the author with the help of Dr. P. Rourke, Dr. B. Vignolle and Dr. C. Proust. The second set of LNCMI results were obtained by Dr. P. Rourke, Dr. J-F. Mercure, N. Wakeham, Prof. N. Hussey with the help of Dr. B. Vignolle and Dr. C. Proust. Finally the data from HFML, Nijmegen was taken by Dr. P. Rourke, I. Mouzoupoulou, Dr. X. Xu and Dr. A. McCollum. The low field data taken in the 'Polo magnet' at Bristol and all the analysis was performed by the author. The investigations described in this section are undertaken in chapter 5.

# Chapter 2

## Theory

---

This chapter outlines the theoretical basis for both the concepts and measurements relevant to this thesis. We start with very brief overview of band and Fermi liquid theory, leading on to the theory behind the dHvA torque technique, then a brief overview of DFT and magnetotransport.

---

### 2.1 Band theory and the Fermi surface

The size and shape of the Fermi surface is key to many electronic phenomena and in particular plays an important role in the formation of the spin density wave (SDW) instability explained in section 2.4. The Fermi surface, defined as the volume in  $k$ -space which bounds the occupied electron states at  $T = 0$  K, is spherical in simple free-electron case. This corresponds with intuition as the electrons tend to the lowest energy states without double occupancy and in the free-electron case the lowest states correspond to the lowest magnitude of  $\mathbf{k}$ . However most Fermi surface topologies are more complicated and may feature more than one ‘sheet’ or ‘pocket’ which encloses occupied (i.e electron) or unoccupied (i.e. hole) states. BaFe<sub>2</sub>P<sub>2</sub> which is the subject of chapter 4, has a combination of both hole and electron pockets in separate regions of the BZ.

To examine how hole and electron pockets may arise, we examine how gaps in the energy dispersion may occur. It can be shown\* that energy gaps appear in the repeated free-electron dispersion when subject to a perturbing periodic potential due to Bragg reflection at the BZ boundaries. This leaves a dispersion which is separated into discrete layers of energy known as ‘bands’. The dispersion forms an inverse parabola near the top of a band and so when the electrons are allocated states, the energy of the Fermi surface states may fall just below the peak of these parabola in which case the  $k$ -space region defined by the unoccupied states at the top of the parabola defines hole pockets of Fermi surface. If the electrons fill up a band entirely and a small portion of the bottom of the next band then the enclosed  $k$ -space region is full of occupied electron states. A more complicated periodic potential can result in partially filled hole and electron band parabolas and hence the semi-metal type Fermi surfaces seen in the pnictides.

---

\*See for example chapter 9 in ref. [81] and chapter 7 of ref. [82].

## 2.2 Fermi liquid theory

The nearly-free electron gas model for ordinary metals\* used as the foundation for the dHvA theory in the next section is an extremely coarse approximation to the real situation and yet provides surprisingly good, predictive results in a variety of scenarios even though the electronic lattice potential is ignored. Fermi liquid theory provides the theoretical basis which explains why we can use non-interacting particle models with a simple modification of the masses of the interacting Fermionic particles.

From a mathematical standpoint, Fermi liquid theory considers a gas of non-interacting particles and gradually ‘switches on’ the interactions. Provided the system transitions adiabatically† then the ‘particles’ in the resulting system, which is known as a ‘Fermi liquid’, can be modelled using the same mathematics as the non-interacting system with an adjusted mass. This adjusted mass is known as the ‘enhanced mass’ and encompasses the interactions in the system with the magnitude being an indicator of the interaction strength. The enhanced mass particles are labelled quasiparticles since they no longer share the same mass as an electron at rest and are, arguably, a product of a mathematical abstraction.

At the time of writing, Fermi liquid theory describes what would be considered ‘ordinary’ metals with deviations from Fermi liquid theory generally considered of interest in a number of systems. Moreover the theory behind measurement techniques such as dHvA — described in the next section — rely on the existence of coherent quasiparticles at the Fermi surface to be valid. The reconciliation of observed dHvA oscillations in cuprates with evidence for reduced quasiparticle weight from ARPES data currently provides one of the interesting challenges of high- $T_c$  research.

## 2.3 De Haas-van Alphen oscillation

In this section the phenomenon of dHvA oscillations is described. It is not immediately apparent how a ramping magnetic field could cause oscillations in such a wide range of parameters but Lifshitz and Kosevich provided an explanation through their eponymous equation based on a theoretical basis set out by Landau. This was then used to characterise the Fermi surface of many metals and establish the field of ‘Fermiology’. Strictly, only the oscillations in magnetisation are dHvA oscillations and those in resistance are called Shubnikov-de Haas oscillations. Nonetheless they both originate from the same underlying phenomena of oscillations in the free energy of the system.

\*A model which only considers the kinetic energies of the electrons and Pauli exclusion terms.

†Adiabatic in this context means with no symmetry breaking changes in phase or, in other words, there is a one-to-one mapping of the particles in the initial non-interacting system to the quasiparticles in the final interacting system.

### 2.3.1 Overview

For metals, the majority of the interesting physics occurs at the Fermi level and, provided Fermi liquid theory holds true, the electrons at the Fermi level can be modelled to a high degree of accuracy with the Sommerfeld model — that is a Fermi gas of non-interacting electrons in an infinite box. When a magnetic field is applied, the electrons have their usual grid pattern distribution of plane wave  $k$ -vectors rearranged such that the electrons move around orbital and helical paths. These rearranged  $k$ -vectors form a set of concentric tubes, known as Landau tubes, whose cross-sectional area,  $a$ , perpendicular to the field is given by the Onsager relation:<sup>\*</sup>

$$a_{k\perp} = (r + 1/2) \frac{2\pi eB}{\hbar} \quad (2.3.1)$$

where  $r$  is a quantisation number that sets apart each tube. We can see from the relation that as  $B$  increases, so does the cross-sectional area of the tubes. As the magnetic field is ramped, successive tubes periodically pass the Fermi surface causing a spike in the DOS at the Fermi level and also oscillations in the energy of the system,  $E$ , which, for geometric reasons explained in the next section, are far stronger at the maximal and minimal (extremal) areas of Fermi surface. Thermodynamic quantities such as magnetisation ( $M = \partial E / \partial B$ ) and heat capacity ( $C_V = \partial E / \partial T|_V$ ) or quantities that depend on the DOS at the Fermi level such as electrical resistance all oscillate as the field is ramped. Oscillations in the susceptibility are known as dHvA oscillations, oscillations in the resistivity are known as Shubnikov-de Haas oscillations.

We can relate the ‘frequency’  $F$  (measured in *tesla*<sup>†</sup>) that the tubes pass the Fermi surface to the extremal Fermi surface area using the following application of the Onsager relation,

$$a_{k\perp} = \frac{2\pi e}{\hbar} F \quad (2.3.2)$$

By varying the direction of the field we can obtain a series of maximal and minimal Fermi surface areas in a variety of orientations in order to build a profile of the Fermi surface topology and size. In practice, there are many possible variations that might fit the model based on areas of cross-sectional slices alone and so typically ab-initio DFT calculations — described in section 2.5 — are employed to provide a basis which can be tweaked based on the constraints from the measurements.

A more detailed analysis of this process follows, beginning with an illustrative mathematical treatment for oscillations in the magnetisation.

<sup>\*</sup>Derivations of the Onsager relation are given in several textbooks including pg. 32 of Shoenberg [83] and pg. 272 of Ashcroft & Mermin [81].

<sup>†</sup>It is *tesla* and not  $\text{tesla}^{-1}$  because, as we shall see later, the oscillations are actually periodic in  $1/B$  and not  $B$  so their frequency counterpart is measured in *tesla*.

### 2.3.2 Exploring the origin of the oscillations

We begin by calculating the degeneracy of the Landau tubes i.e. the number of electron states per tube. Because the states under a magnetic field are a one-to-one rearrangement of the states with no field, we can use the Sommerfeld number of states per unit k-space ( $V/4\pi^3$ ) to determine the degeneracy. From the Onsager relation (eqn. 2.3.1) we see that the additional area for successive tubes is  $\Delta a_{k_\perp} = 2\pi eB/\hbar$  which we can convert to a volume by integrating over  $k_\perp$ . This gives a degeneracy per tube therefore of,

$$D_{\text{tube}} = dk_\perp \left( \frac{2\pi eB}{\hbar} \right) \left( \frac{V}{4\pi^3} \right) = \frac{eBVdk_\perp}{\hbar 2\pi^2} \quad (2.3.3)$$

We continue by writing an expression for the energy of the system,  $E$  by summing the energies of the states that lie beneath the cross-sectional area defined by the Fermi surface ( $a_{k_\perp F}$ ) for a given  $k_\perp$ . To do this, we use the Onsager equation to determine  $R_\perp$  — the number of Landau tubes below the Fermi surface at this cross-sectional slice. We then multiply this by the degeneracy of the tubes,  $D$  and the energy for states on that particular Landau tube,  $\epsilon_r$ ,

$$E = D \sum_r^{R_\perp} \epsilon_r = \frac{eBVdk_\perp}{\hbar 2\pi^2} \sum_r^{R_\perp} \epsilon_r \quad (2.3.4)$$

where,

$$R_\perp = \text{floor} \left[ \frac{a_{k_\perp F}\hbar}{2\pi eB} - \frac{1}{2} \right] \quad (2.3.5)$$

where  $\text{floor}(x)$  is the largest integer which is less than  $x$ . To complete the above equation, we need an expression for the energies of each of the Landau tubes. The procedure for the free electron case is to insert the canonical momentum (i.e momentum of a free electron in a magnetic field) into the non-interacting Schrödinger equation and solve to obtain the following eigenvalues for the energies on the Landau tubes. Full derivations can be found in several textbooks\* and so will not be repeated here. Below is the expression for the energy eigenvalues,

$$\epsilon_r = (r + 1/2)\hbar\omega_c + \frac{\hbar^2 k^2}{2m_0} \quad \text{where, } \omega_c = \frac{eB}{m_0} \quad (2.3.6)$$

and is known as the ‘cyclotron frequency’. The summation term in equation 2.3.4 can now

---

\*See for examples pg. 32ff. in Shoenberg [83] or pg. 148ff. in Blundell [84].

be written,

$$\begin{aligned}
 \sum_r^{R_\perp} \epsilon_r &= \sum_r^{R_\perp} \left( (r + 1/2) \hbar \omega_c + \frac{\hbar^2 k^2}{2m_0} \right) \\
 &= \frac{\hbar e B}{m_0} \sum_r^{R_\perp} r + \frac{\hbar e B}{2m_0} \sum_r^{R_\perp} 1 + \frac{\hbar^2 k^2}{2m_0} \sum_r^{R_\perp} 1 \\
 &= \frac{\hbar e B}{2m_0} R_\perp (R_\perp + 1) + \frac{\hbar e B}{2m_0} R_\perp + \frac{\hbar^2 k^2}{2m_0} R_\perp \\
 &= \frac{\hbar e B}{2m_0} R_\perp^2 + \left( \frac{\hbar e B}{m_0} + \frac{\hbar^2 k^2}{2m_0} \right) R_\perp
 \end{aligned}$$

which can be expanded out and finally substituted back into equation 2.3.4 to finally obtain,

$$E = \frac{e^2 V dk_\perp}{4\pi^2 m_0} B^2 \left[ R_\perp^2 + 2R_\perp + \frac{\hbar k^2}{e} \frac{1}{B} R_\perp \right] \quad (2.3.7)$$

Key to the above relation is that, although  $R_\perp$  is inversely proportional to  $B$ , it remains discrete. This gives rise to the saw-tooth like function shown in figure 2.3.1 for some typical experimental parameters. Also plotted is the function against  $1/B$  where we can clearly see that the oscillations are periodic in inverse field hence the frequency being measured in tesla $^{-1}$ .

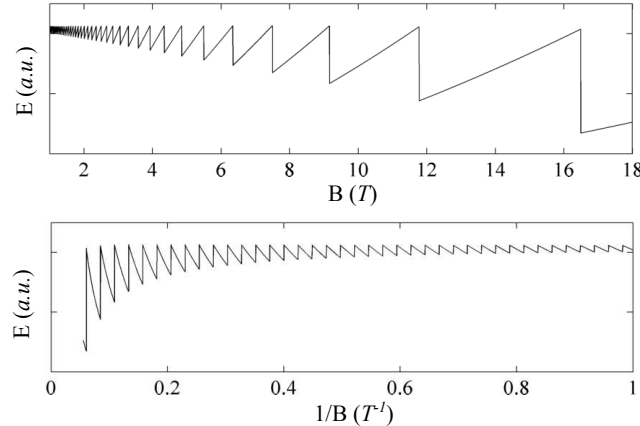


**Figure 2.3.1:** Theoretical energy oscillations for a Fermi surface orbit which is 5% of a 5 Å cubic BZ between 1-18 T. Kinetic energy term is taken to be for an electron at a level half the size of the Fermi surface.

The above is not a rigorous derivation but is nonetheless illustrative of the origin of the oscillation in the system energy and how any thermodynamic value which depends on the energy of the system oscillates as a function of field. To continue we need to include correction factors to the oscillation amplitude due to finite electron scattering rates ( $A_D$ ), temperature ( $A_T$ ), Zeeman splitting of spins ( $A_s$ ), doping ( $A_{\text{dop}}$ ), mosaicity

( $A_{\text{mos}}$ ), warping of the Fermi surface ( $A_{\text{warp}}$ ), inhomogeneity of the magnetic field ( $A_{\Delta B}$ ) as well as adjustments due to the fact that the parameter measured was torque of the sample in a field and not the energy or magnetisation directly ( $A_{\Gamma}$ ). For this, we turn to a more solid foundation that was put forward by Lifschitz and Kosevitch.

### 2.3.3 Lifschitz–Kosevitch equation

The derivation for the full expression for the Landau thermodynamic potential,  $\Omega^*$ , begins in a similar way to the previous illustrative example but frames the sawtooth-like function above as a more mathematically manageable Fourier decomposition which also conveniently makes the technique highly amenable to Fourier analysis. For this reason the equation below features higher harmonics which are denoted with the identifier  $p$ .

$$\Omega = \left( \frac{e}{2\pi\hbar} \right)^{\frac{3}{2}} \frac{e\hbar B^{\frac{5}{2}}}{m_0\pi^2} \left| \frac{\partial^2 a_{\text{ext}}}{\partial k_{\perp}^2} \right|^{-\frac{1}{2}} \sum_{p=1}^{\infty} p^{-\frac{5}{2}} A_{\text{tot}} \cos \left[ 2\pi p \left( \frac{F}{B} - \gamma \right) \pm \frac{\pi}{4} \right] \quad (2.3.8)$$

where,

$$A_{\text{tot}} = A_T A_D A_s A_{\Gamma} A_{\text{mos}} A_{\text{dop}} A_{\Delta B} \quad (2.3.9)$$

The above equation and derivatives of it are known as the Lifschitz–Kosevitch (LK) equation. To obtain the magnetisation the differential with respect to  $B$  is taken to get,

$$M = \left( \frac{e}{\hbar} \right)^{\frac{3}{2}} \frac{e\hbar F V B^{\frac{1}{2}}}{m_0\pi^{\frac{5}{2}}\sqrt{2}} \left| \frac{\partial^2 a_{\text{ext}}}{\partial k_{\perp}^2} \right|^{-\frac{1}{2}} \sum_{p=1}^{\infty} p^{-\frac{3}{2}} A_{\text{tot}} \sin \left[ 2\pi p \left( \frac{F}{B} - \gamma \right) \pm \frac{\pi}{4} \right] \quad (2.3.10)$$

To attain the above equations, it was necessary to perform an integral over  $k_{\perp}^{\dagger}$  which results in a parameter for an extremal Fermi surface orbit area perpendicular to the field given by  $a_{\text{ext}}$ .

#### Attenuation for non-extremal orbits

Quantum oscillation measurement is often described as a probe of the extremal (i.e. the largest and smallest) Fermi surface orbits perpendicular to the magnetic field. However it is not immediately clear how this comes about, nor how some hypothetical Fermi surfaces, such as a perfect cone, would appear in quantum oscillation measurements.

Strictly, all cross-sectional orbits along  $k_{\perp}$  contribute to the system energy as determined in the LK equation and each of these orbits has a particular frequency,  $F(k_{\perp})$ , related to its orbital area by eqn. 2.3.2. Since all these frequencies interfere, the regions of  $k_{\perp}$  where the frequencies vary the least dominate the contribution to the system energy,

---

<sup>\*</sup>Formally defined as the energy in a open system that is in thermal contact with its surroundings.

<sup>†</sup>Similar to the integral in the toy equation from the previous section.

i.e. where  $dF(k_\perp)/dk_\perp$  is smallest. In other words, regions along  $k_\perp$  where there are stationary points in  $F(k_\perp)$  contribute the most to the oscillations in the system energy.

This means for a hypothetical conical Fermi surface with sharp edges, for a field along the cone axis, there would be no stationary points in  $F(k_\perp)$  and there would be no dominant frequency contributing to the oscillations in the system energy *from stationary points*. However it may be possible that a conical Fermi surface can contribute a signal to the Fermi surface that is comparable to a stationary point if the wide end of the conical Fermi surface is comparable in size to the momentum spacing of the Landau tubes — the so called ‘2D limit’. This restricts the field regimes in which extremal oscillations can be examined in isolation\*.

The above is illustrated in figure 2.3.2. The insets shows a cross-sectional slice of the described hypothetical conical Fermi surface as the dashed lines, and a parabolic Fermi surface as a solid line. Assuming field is applied along  $k_z$ , the parabolic Fermi surface has a stationary point at its midpoint, the conical Fermi surface has no stationary points. The main panels each show the result of numerically integrating  $\int \cos(2\pi F(k_\perp)/B) dk_\perp$  where  $F(k_\perp)$  is related to the cross-sectional area of Fermi surfaces in inset through equation 2.3.2. The maximum radii of the hypothetical Fermi surfaces increase in each panel from  $k_r = 0.0075 \text{ \AA}^{-1}$  in the top left panel to  $k_r = 0.05 \text{ \AA}^{-1}$  in the bottom right.

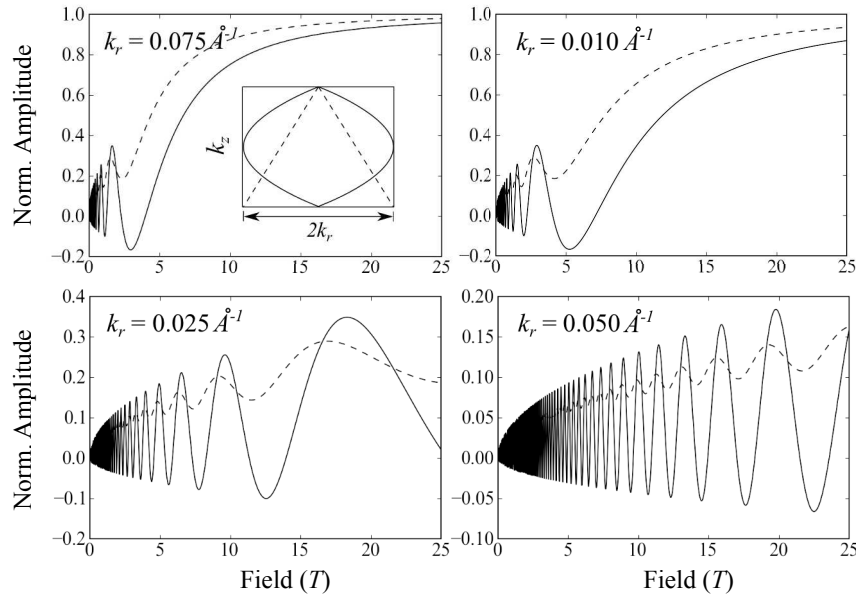


**Figure 2.3.2:** Inset: hypothetical radially symmetric Fermi surface slices in the [110] plane with maximum radius  $k_r$  shown: dashed line is conical, solid line is parabolic. Main panels: Results of  $\int \cos(2\pi F(k_\perp)/B) dk_\perp$  where  $F(k_\perp)$  is related to the cross-sectional area of Fermi surfaces in inset through eqn. 2.3.2, from top left:  $k_r = 0.075, 0.01, 0.025, 0.05$  respectively.

---

\*However, beating effects from similarly sized extremal areas can be employed to measure surface smaller than this limit, see for example [85].

For the cases where the sides of the conical surface are steep, then the associated oscillation is weaker than that from the comparable parabolic Fermi surface as is shown in the bottom two panels of figure 2.3.2. However, for the narrow Fermi surfaces, the top two panels show how above a particular field, where the spacing between successive Landau tubes become large in momentum, the signal from the conical and the parabolic surface become comparable. This makes sense if we consider the Landau tubes as an oscillatory probe — the resolution is limited by wavelength and in this regime the relatively flat conical sides cannot be distinguished from a stationary point.

To measure the finer stationary point features on the Fermi surface (i.e. shallow corrugations or small pockets) attention needs to be paid to the rapidly oscillating low field region. As can be seen in the top two panels, the parabolic signal is much stronger than the conical signal here. However this region is often obscured by technical problems of high frequency Johnson noise, insufficient sample rates and superconductivity.

The data analysis also requires sufficient oscillations for a fast fourier transform (FFT). The top right panel of figure 2.3.2 shows that in the region of 6 T and above, only half an oscillation has occurred meaning FFT is unlikely to give a strong signal. Since data in the dHvA experiment was taken between 6 T and 18 T we should not expect to be able to resolve pockets of radius less than  $k_r \sim 0.01 \text{ \AA}^{-1}$  without resorting to analysis of beating effects [85].

The rate of change of the gradient of the energy dispersion along the electron orbit therefore affects the oscillation amplitude and is accounted for in the second derivative term in equation 2.3.10. The flatter the dispersion, the larger this term will be. In the limiting case where the dispersion in  $k_\perp$  is effectively flat close to the orbit then we get the ‘Yamaji condition’ [86], and the oscillations are greatly enhanced.

We move now to the other attenuating factors listed towards the end of section 2.3.2. The above calculation demonstrated how a distribution of frequencies can attenuate an oscillation. At infinity, interfering oscillations with a distribution of frequencies can be approximated instead as interfering oscillations with a distribution of phases. Because the oscillations we are measuring are in inverse field, once they become resolvable due to the experimental problems of noise, sample rates etc. the infinite oscillation approximation becomes valid. This means we can model each attenuating factor by convolving an appropriate phase distribution function with the cosine oscillatory term. It can be shown\* that this convolution results in a relatively simple multiplication factor — hence the various  $A$  factors listed in the LK equation which we expand upon below.

---

\*See for example, Shoenberg pg 57–59. [83].

### Attenuation due to temperature

To find the appropriate phase distribution function for the temperature dependence we start with the Fermi distribution,

$$f(\epsilon) = \frac{1}{\exp((\epsilon - \mu)/kT) + 1} \quad (2.3.11)$$

The differential of this distribution results in the broadening function (which is proportional to the probability that the Fermi energy  $\mu$  is between  $\epsilon$  and  $\epsilon + d\epsilon$ ),

$$P(\epsilon < \mu < \epsilon + d\epsilon) \propto \frac{d\epsilon}{2kT(1 + \cosh[(\epsilon - \mu)/kT])} \quad (2.3.12)$$

This is convolved with the energy distribution which smears the Fermi surface. Because the Fermi surface is smeared, so is the parameter  $F$  which spreads the Fourier transform peak due to the oscillation in the system energy, leading to an attenuation of the Fourier amplitude. The final attenuation factor due to this smearing is given in Shoenberg pg. 59ff [83] and is reproduced below,

$$A_T = \frac{X}{\sinh(X)} \quad \text{where, } X = \frac{2\pi^2 p k T m_T^*}{e \hbar B} \quad (2.3.13)$$

The above factor includes  $m_T^*$ , the ‘thermal effective mass’ as a term in a function of  $T$ . As a consequence, by studying the temperature dependence of the amplitude it is possible to get a measure of  $m_T^*$  of the electrons at the extremal orbit. Techniques for doing this are discussed in section 3.1.4.

The LK equation arises from a semi-classical approach in that it considers a system of single particle Bloch functions which are manipulated using classical relations. Many-body effects such as electron-phonon and electron-electron interactions were incorporated later in the development of quantum oscillation theory and were shown to affect  $A_s$  and  $A_T$ . In the above case,  $A_T$  is modified by both electron-phonon and electron-electron effects which is manifest through changes to the effective mass term [83]. The effective mass determined in this way is enhanced subject to the same interactions as in heat capacity experiments but are probed for a particular Fermi surface orbit, whereas heat capacity is averaged over the entire Fermi surface. As we will see later the thermal mass enhancement is different to the mass enhancement from spin measurements. For more one this see Rourke *et al.* [77], [83] and references therein.

### Attenuation due to finite quasiparticle lifetime

The ‘Dingle factor’,  $A_D$ , is due to the finite lifetime,  $\tau$ , of the electron quasiparticles due to scattering. Because of this time scale, there is a smearing of the electron energy through

the uncertainty principle with a broadening which is approximately Lorentzian in shape. If we assume  $\tau$  does not change with energy\*, then this can be modelled as a smearing of the Fermi level such that the broadening function is,

$$P(\epsilon < \mu < \epsilon + d\epsilon) \propto \frac{d\epsilon}{(\epsilon - \mu)^2 + (\hbar/2\tau)^2} \quad (2.3.14)$$

and such that after the routine Fourier transform, the end relation is given by,

$$A_D = e^{-\pi pm_b/eB\tau} = e^{-\pi p/\omega_c\tau} \quad (2.3.15)$$

The exponent in the above can be thought of as the number of orbits the electron has completed (i.e. each harmonic  $p$  is another successive orbit) divided by the expected number of orbits it will complete, so evidently we expect to see the higher harmonics having an exponentially lower amplitude. We also expect the tighter, smaller orbits to have a stronger amplitude. The term  $m_b$  refers to the ‘band mass’ which will be discussed in detail later on. Sometimes when discussing the Dingle term, we refer to the Dingle factor which is the factor in the exponential defined as  $\alpha \equiv -\pi pm_b/(e\tau)$ .

### Attenuation due to spin splitting

Applying a magnetic field causes a Zeeman splitting of energy levels of magnitude,

$$\Delta\epsilon = \frac{g\mu_B B}{2} \quad (2.3.16)$$

where  $\mu_B$  is the single electron magnetic moment (the Bohr magneton) and  $g$  is a factor that is  $\approx 2$  for free electrons. Rather than smearing, this can be thought of as two separate Fermi surfaces with separate Fermi energies. The attenuation is given now as,

$$A_s = \cos\left(\frac{\pi pgm_s^*}{2}\right) \quad (2.3.17)$$

where  $m_s^*$  is the ‘spin effective mass’. This is subject to a different set of many-body interactions in comparison to the thermal effective mass – notably only electron-electron correlations and not the electron-phonon interactions. Moreover, whilst the spin effective mass is affected by the many body effects, so is the Landé  $g$  factor and even the shape of the Fermi surface. The spin mass enhancement is related to the standard Stoner enhancement factor,  $S = 1/(1 - IN(E_F))$  by  $m_s^* = (1 + S)m_b$ .

---

\*This is not the case, but at most only a few Landau levels contribute to a particular oscillation and if we assume that the energy does not vary too much between subsequent levels then the assumption is a good one.

### Other attenuating factors

Another attenuating factor is due to slight misalignments in the crystal structure, ( $A_{mos}$ ). A misaligned mosaic polycrystalline structure can be modelled with an appropriate broadening function. Shoenberg suggests a Lorentzian broadening function, which leads to an attenuation term which is similar to 2.3.15, although the actual distribution of misalignments could be any distribution. Given a Lorentzian broadening function, the final form would look like the following,

$$A_{mos} = e^{2\pi p \Delta F_{mos}/B} \quad (2.3.18)$$

where  $\Delta F_{mos}$  is a parameter that determines the degree of overall misalignment.

The final attenuating factors mentioned here are  $A_{\Delta B}$ , the damping due to field inhomogeneity which has an effect depending on the shape of the field and  $A_{dop}$ , which is another Lorentzian-like broadening factor due to the doping inhomogeneity in the sample. Neither of which will be considered in the thesis — the material studied is undoped, and the magnet is suitably large as to have an essentially constant field profile — and so will not be explored further\*

### 2.3.4 Band mass

So far, three different electron masses have been defined, the thermal effective mass, the spin effective mass and the free electron mass. We now define the ‘band mass’. This the effective mass determined from the bandstructure generated by our DFT calculations. It is calculated as follows,

$$m_b^* = \frac{\hbar}{2\pi} \oint_{\text{Orbit}} \frac{d\mathbf{k}}{v_F(\mathbf{k})} = \frac{\hbar^2}{2\pi} \frac{\partial a_{k_\perp}}{\partial \epsilon} \quad (2.3.19)$$

Mass enhancement comes from any kind of interactions the electron has with its environment — e.g. external fields, other electrons and nuclei — resulting in the free electron mass  $m_e$  becoming enhanced (renormalised). The band mass is determined from DFT calculations and so the resulting enhancement is therefore a product of interactions as modelled by the mean-field approximations used in the DFT calculation. However, as we will see in section 2.5, DFT calculations typically do not model correlation effects well or dynamic interactions at all meaning that the band mass only approximates the effects of correlations and is only valid for  $T = 0$  K. We know that both the thermal effective mass and the spin effective mass, determined from measurements, are enhanced according to the actual band structure plus a unique set of interactions specified previously. Figure 2.3.3 details how each of the quasiparticle masses become more refined starting from the crude free-electron mass approximation on the left and ending with the actual enhancements due to particular interactions on the right.

---

\*If you do want to consider these factors, ref. [77] has a passage on doping homogeneity and pg. 64 of Shoenberg discusses field inhomogeneity [83].

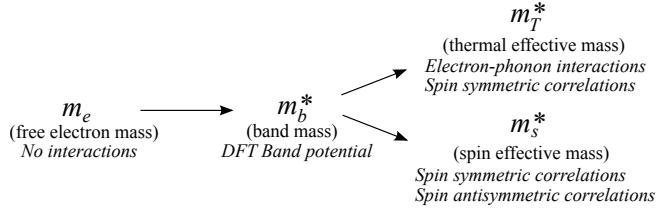


**Figure 2.3.3:** A diagram showing a progression in refinement of the interactions represented in the enhanced electron masses. Additional interaction effects are listed in italics.

The band mass is a result of calculation and so is only as good as the DFT band-structure. However it provides a good baseline from which to compare the thermal and spin effective masses in order to get a sense of the strength of their respective particular interactions.

### A 2D Approximation

Although none of the attenuating factors above have an explicit angle dependence, they do vary as a function of angle through the band mass. A common approximation to simulate the dependency in layered systems is to assume the Fermi surface has a flat dispersion along the  $k_z$  direction — i.e. is ‘two dimensional’ — and therefore appears cylindrical in a three dimensional BZ. The cross sectional area of a cylinder is given by,

$$a = \frac{a_0}{\cos \theta}, \quad (2.3.20)$$

where  $\theta$  is the angle from the cylinder axis. Increasing the Fermi energy by  $\Delta\epsilon$  will cause the cross section at zero angle to change by amount  $\Delta a_0$ , then the band mass is given by,

$$m_b^* = \frac{\hbar^2}{2\pi} \frac{\partial a_{k\perp}}{\partial \epsilon} = \frac{\hbar^2}{2\pi} \frac{\partial}{\partial \epsilon} \left( \frac{a_0 + \Delta a_0}{\cos \theta} - \frac{a_0}{\cos \theta} \right) = \frac{\hbar^2}{2\pi} \frac{\partial a_0}{\partial \epsilon} \frac{1}{\cos \theta}, \quad (2.3.21)$$

therefore

$$m_b^* = \frac{m_{b0}^*}{\cos \theta} \quad (2.3.22)$$

This means that under this approximation, any factor that includes the band mass, explicitly or implicitly\* can be resolved using the zero angle band mass with an angle dependence of  $1/\cos \theta$ .

### 2.3.5 Final theoretical observations

Originally dHvA measurements were performed on elemental metals which, by definition, have a Fermi surface and aside from the  $d$  and  $f$  electron metals are well modelled by Fermi

---

\*Meaning  $m_T^*$  and  $m_S^*$  which are both enhancements of the band mass.

liquid theory. The fact that oscillations have been observed in cuprates and pnictides which have demonstrated distinctly non-Fermi liquid behaviour is therefore remarkable and moreover implies the presence of coherent quasi-particles at a Fermi surface, at least in the presence of a strong magnetic field. States in which these conditions co-incide are usually referred to as ‘generalised Fermi liquids’ which demonstrates some of the hallmarks of Fermi liquid such as a Fermi surface but not others such as an energy squared dependence of the imaginary self energy. For more details see refs. [87] and [88].

## 2.4 Spin density wave instability

Section 1.2 discussed the possibility of high- $T_c$  pairing being due to fluctuations in close proximity to a SDW state. Here we briefly describe the SDW state and some of the theory behind it.

Broadly speaking a SDW is a magnetic state just as ferromagnetism and antiferromagnetism are magnetic states. In its most general sense, a SDW is a periodic modulation of magnetic spins in both space and time hence it being a ‘wave of spin density’. AFM is actually a special case of a SDW which does not vary in time, i.e. is static, and also varies spatially with the periodicity being some multiple of the real-space lattice vector, i.e. is commensurate with the lattice. Ferromagnetism can be thought of as a SDW state with wavevector  $\mathbf{q} = 0$  i.e. it has no periodic variation and so is not really a ‘wave’.

Using the mean field Hartree-Fock approximation (HFA) the following expression gives the stability condition for the SDW state [89],

$$2I\chi_0(\mathbf{q}) > 1, \quad (2.4.1)$$

where  $I$  is the exchange energy between electron bands and  $\chi_0$  is the Lindhard susceptibility. The greater the Lindhard susceptibility, the more stable the state.

### 2.4.1 Lindhard susceptibility

The Lindhard susceptibility models the Stoner excitations (i.e. electron-hole scattering) of a nearly free electron system. To derive the Lindhard susceptibility, we begin with a Fermi liquid i.e. a Pauli excluded but otherwise non-interacting gas of free electrons. We calculate\* the first order perturbative linear response of this gas to a magnetic field given by  $\mathbf{B} = \exp(\mathbf{q} \cdot \mathbf{r} - i\omega t)$ . The resulting equation is often quoted as,

$$\chi_0(q, \omega) = \lim_{\delta \rightarrow 0} \sum_k \sum_{l,l'} \frac{f(\epsilon_{k+q,l'}) - f(\epsilon_{k,l})}{\epsilon_{k+q,l'} - \epsilon_{k,l} - \hbar\omega - i\delta} D \quad (2.4.2)$$

---

\*Not presented here but pg 81 ff. of Dressel [90] has a full derivation.

where,

$$D = |\langle k + q, l' | V | k, l \rangle|^2 \quad (2.4.3)$$

and is the matrix transition element for the scattering process. The numerator term contains two Fermi functions — the same as equation 2.3.11 — which ensure that the susceptibility is finite for states which scatter across the Fermi energy and zero if they do not - consequently, the Lindhard susceptibility models electron-hole scattering (Stoner excitations) in particular. The Fermi functions also smear the susceptibility dispersion as a function of temperature. The third term in the denominator corresponds to the excitation energy of the perturbing field with  $\omega$  corresponding to the temporal frequency of the field. The final term in the denominator is an artefact of the adiabatic approximation used to calculate the perturbation with the completed approximation taking the limit of  $\delta \rightarrow 0$ . The first sum in the Lindhard function is over all  $k$  states in the first BZ, the second sum combines each energy band. The real and imaginary parts of equation 2.4.2 are,

$$\text{Re}\{\chi_0(q, \omega)\} = \lim_{\delta \rightarrow 0} \sum_k \sum_{l, l'} \frac{(\epsilon_{k+q, l'} - \epsilon_{k, l} - \hbar\omega)(f(\epsilon_{k+q, l'}) - f(\epsilon_{k, l}))}{(\epsilon_{k+q, l'} - \epsilon_{k, l} - \hbar\omega)^2 + \delta^2} D \quad (2.4.4)$$

$$\text{Im}\{\chi_0(q, \omega)\} = \lim_{\delta \rightarrow 0} \sum_k \sum_{l, l'} \frac{-\delta(f(\epsilon_{k+q, l'}) - f(\epsilon_{k, l}))}{(\epsilon_{k+q, l'} - \epsilon_{k, l} - \hbar\omega)^2 + \delta^2} D \quad (2.4.5)$$

$$(2.4.6)$$

respectively. The real part is important in the context of instabilities in metals, the imaginary part gives the resonance modes for bosonic excitations such as e.g. plasmons, spin density waves, charge density waves, phonons etc. of energy  $\hbar\omega$ .

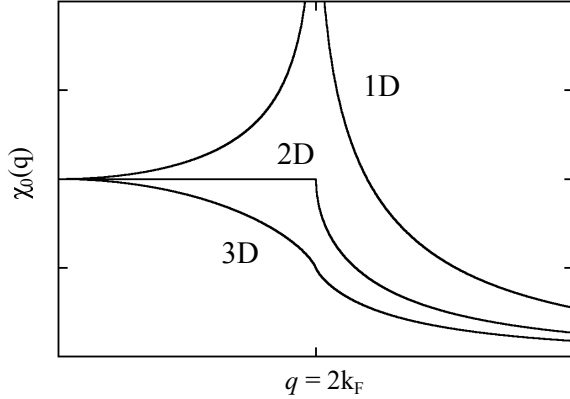


**Figure 2.4.1:** The analytically solved Lindhard susceptibility as a function of  $q$  for the one, two and three dimensional cases for a free electron dispersion. Plotted from formulae derived in ref. [90].

For the case of a free electron gas subject to a perturbing stationary wave (i.e.  $\omega = 0$ ), the Lindhard susceptibility can be resolved analytically. Figure 2.4.1 shows the suscepti-

bility as a function of  $q$  for the one, two and three dimensional cases obtained from ref. [90]. We can see that for the one dimensional case that there is a singularity at  $q = 2k_F$  which, according to equation 2.4.1, would imply a SDW state at that wavevector. For the three dimensional case however the susceptibility peaks at  $q = 0$  which implies a ferromagnetic instability. In the non-free electron case, a SDW state can occur in a three dimensional material when a particular bandstructure condition known as ‘nesting’ is met.

### 2.4.2 Band structure nesting

The nesting condition can be expressed in mathematical terms as follows [91],

$$\epsilon_{\mathbf{k}} = \epsilon_{\mathbf{k}+Q} \quad \text{for} \quad \epsilon_{\mathbf{k}} = \epsilon_F \quad (2.4.7)$$

where  $Q$  is the ‘nesting wavevector’ and is characteristic of the particular nesting condition and  $\epsilon_F$  is the Fermi energy. In geometric terms this corresponds to a mapping, across  $Q$  in the BZ, of a section of Fermi surface onto another section of similar size and shape.

Majlis explores a hypothetical nesting case with a band dispersion of form  $\epsilon_k = -\epsilon_0(\cos k_x a + \cos k_y a + \cos k_z a)$  which results in a nesting vector of  $Q = (\frac{\pi}{a}, \frac{\pi}{a}, \frac{\pi}{a})$  resulting in a ‘perfect’ nesting condition, (see ref. [91] pg. 214). In practice, nesting may only be partial as perhaps only small regions of the Fermi surface satisfy or come close to satisfying the above condition, leading to only modest enhancements of the Lindhard function. It is these regions of nesting however that are of key interest to contemporary research into high- $T_c$  superconductivity, since it is in these regions we find the antiferromagnetic fluctuations that are thought to underlie the pairing mechanism.

### 2.4.3 Spin density wave fluctuations

The left panel of figure 2.4.2 illustrates the pairing potential,  $V$ , due to the retarded response of the ionic lattice to a passing quasiparticle,  $e$ . This mechanism underlies conventional, i.e. BCS model, superconductivity and overcomes the Coulomb repulsion by a combination of ionic shielding of the quasiparticle charge and crucially a separation of the bound electrons in time as well as space.

The right panel of figure 2.4.2 shows the pairing potential due to an antiferromagnetic spin fluctuation — a precursor to the magnetic ordering that is found in the fully formed SDW state. Here the Coulomb potential is overcome by separating the bound quasiparticles over space by a wavevector  $Q$ . The inset to figure 2.4.2 illustrates a 2D representation of the pairing potential at neighbouring sites and shows how in some regions the pairing potential is attractive and in some regions the pairing potential is repulsive.

Cox *et al.* offers an explanation of how the potential due to the spin density fluctuation can be understood in terms of the nascent SDW order propagating spin alignment in the background electronic medium [93]. An electron moving through an electronic background

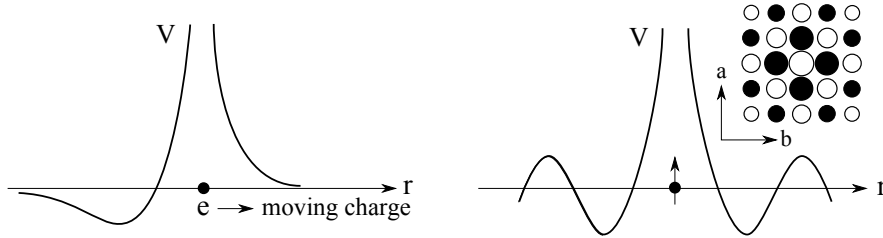


**Figure 2.4.2:** Schematic plots of the pairing potential in real-space. Left: the potential due to a retarded response of the ion lattice to a passing electron as captured in the BCS model. Right: the potential due to a spin fluctuation. Inset: the real-space locations of the attractive potentials (filled circles) and repulsive potentials (empty circles). Adapted from ref. [92].

couples via correlation to an electron in the background with wavevector  $\mathbf{k}$  causing the spin of the background electron to anti-align. Another electron in the background at wavevector  $\mathbf{k} + \mathbf{Q}$  also flips due to an antiferromagnetic spin fluctuation\*. Because of the polarised nature of the background electron at  $\mathbf{k} + \mathbf{Q}$ , correlation makes the conditions favourable to spins of opposite alignment, hence the attractive potential for the quasiparticle necessary to create a bound singlet state.

#### 2.4.4 Notes on practical calculation

Taking the limits of  $\delta \rightarrow 0$  of equation 2.4.6 which is effectively an ever narrowing Lorentzian distribution, results in an expression for the imaginary part of Lindhard susceptibility,  $\text{Im}(\chi_0) \propto \delta(\epsilon_{k+q,l'} - \epsilon_{k,l} - \hbar\omega)$  where  $\delta$  here is the Dirac delta function. In a calculation on a continuous energy dispersion, this results in resonances at excitations which match the difference in energies between states. However, in this thesis, the energy dispersions used to determine nesting conditions are not continuous and instead are based on discrete energies obtained from DFT calculations. As such  $\delta$  will have to remain finite in order to broaden the delta function into a Lorentzian with width comparable to the energy differences between the discrete points – the net result of this will be loss of some fine structure.

Secondly, only bands that lie close to the Fermi energy contribute significantly to the susceptibility. Since the calculations are computationally costly, only bands which are close (within the adiabatic or temperature broadening) to the Fermi energy are input into the calculations.

Finally, we make the assumption that the transition matrix elements are unity. This assumption greatly simplifies the calculations at the cost of some structure and as such should be borne in mind when that the resulting calculations are somewhat broad and should only be used to make qualitative statements about the nesting condition.

\*Presumably this is less likely in a fully formed SDW state due to the stiffness of the state and the energy cost in creating long lived spin excitations.

## 2.5 Density functional theory

The interpretation of the dHvA measurements presented later in this thesis rely to some extent on the ab-initio calculation of the energy bands of BaFe<sub>2</sub>P<sub>2</sub> using the WIEN2k code [94] — the technique used to find these energy dispersions are based on a DFT scheme. The following is broad overview of DFT which is drawn from notes from a series of summer school lectures by M. Lüders [95] and the ‘ABC of DFT’ by K. Burke [96].

Although implementations of DFT rely on various approximations, DFT itself has been shown to be exact and mathematically rigorous. It comprises of a set of theorems developed and proven by Hohenberg, Kohn and Levy [97, 98] and a methodology for solving to obtain the ground state energies developed by Kohn and Sham. The principle theorem outlined by Hohenberg-Kohn (HK) shows that the ground state external potential,  $v_{\text{ext}}(\mathbf{r})$ , of a system can be determined by the ground state density,  $n(\mathbf{r})$ , alone and vice-versa. A second HK theorem outlines a minimisation condition which expresses the ground state energy as follows,

$$\frac{\partial F[n]}{\partial n(\mathbf{r})} + v_{\text{ext}}(\mathbf{r}) = \mu, \quad (2.5.1)$$

where,

$$F[n] = T[n] + V_{\text{ee}}[n] \quad (2.5.2)$$

$F[n]$  is the ‘universal’ functional\* and  $T[n]$  and  $V_{\text{ee}}[n]$  are the kinetic and correlation functionals respectively.  $\mu$  is the chemical potential which is introduced as a normalisation term that ensures that there are an appropriate number of electrons in the charge density. The universal functional is so called because the system is completely defined in the external potential term alone and so  $F[n]$  is common to all systems, nonetheless it still requires approximation. For this reason as well as the fact that there are no clues from the HK theorems as to a good starting form for  $n$ , still means the problem is intractable.

Kohn-Sham developed a method to find a good starting form for  $n$  by showing that there exists a pseudo-potential,  $v_{\text{KS}}$ , that satisfies the above equation for a *non-interacting* system, i.e.  $F[n] = T[n]$ , which shares the same  $n$  as the original interacting system. This abstract potential, which takes the place of  $v_{\text{ext}}$  in the above equation, has no strict physical meaning but it allows us to build a common expression for  $n$  in terms of a sum of single particle wavefunctions. It is given as follows,

$$v_{\text{KS}} = v_{\text{ext}}(\mathbf{r}) + \int d^3 r' \frac{n(\mathbf{r}')}{|\mathbf{r} - \mathbf{r}'|} + \frac{\partial E_{\text{xc}}}{\partial n(\mathbf{r})} \quad (2.5.3)$$

where  $E_{\text{xc}}$  is the combined particle correlation and exchange energy terms which is ap-

---

\*A functional maps a function onto a single vector or scalar — typically by integrating over the function — and is commonly denoted with the function parameter in square brackets. Compare this with the definition of a function which maps a series of scalars onto a single scalar or vector.

proximated according to the type of problem to be solved\*. Once an approximate form for the exchange term has been chosen, the above can be used to find the ground state energy by running a self consistency cycle that forms the heart of most DFT codes,

1. Guess an initial  $n_{i=0}$
2. Calculate  $v_{\text{KS}}$  from  $n_i$  using eqn. 2.5.3
3. Minimise the non-interacting (Kohn-Sham) form of eqn. 2.5.1
4. Calculate the new  $n_{i+1}$
5. Repeat from step 2 with  $n_i$  being adjusted by  $n_{i+1}$  until  $n_i - n_{i+1} < \text{some tolerance}$

Simply replacing  $n_i$  with  $n_{i+1}$  can cause the calculation to rapidly diverge and so instead a mixing scheme is used. Typically this incorporates a small fraction of  $n_{i+1}$  with the rest made up of the old  $n_i$ . A more complex mixing scheme can be employed to ensure more rapid convergence, the Broyden mixing scheme for example uses a Newton-Raphson style root finding mechanism on the Jacobian of the  $n_i - n_{i+1}$  [99].

### 2.5.1 The generalised gradient approximation

The correlation term represents the most significant approximation in the calculation of DFT. For the DFT presented in this thesis, the GGA was used which is part of the family of local density approximations (LDAs). The simplest (i.e. lowest order) LDA takes the effects of the electron-electron correlations at point  $\mathbf{r}$  to be constant throughout the system with the magnitude based on the charge density at  $\mathbf{r}$ . This works particularly well for free-electron-like systems with lots of itinerant valence electrons since the electrons are evenly spread throughout — however it does not work so well for highly localised Hubbard-like systems where there is a high density of electrons at atomic sites, but very little density just off the sites. A step towards improving this comes by raising the order of the approximation so that it modifies the constant local density with the rate of change of the local density as you move off the site (i.e. the local charge density gradient). It turns out however that incorporating the gradient results in less accuracy than the simple LDA due to the LDA ‘accidentally’ cancelling a series of so called sum rules. The GGA builds on the higher order gradient approximation by incorporating the cancelling of the sum rules to obtain a reasonably accurate approximation to the correlation potential.

The precise way to express the GGA however is still a matter of debate though with there being multiple implementations [100, 101], each of which may give slightly different results<sup>†</sup>. Nonetheless GGAs tends to perform better than zeroth order LDA with inhomogeneous electron densities.

---

\*Note that in principle, these two terms should be separate but most approximations tend to combine them into a single term.

<sup>†</sup>See for example table 1 in ref. [100]

### 2.5.2 Single particle wavefunction bases

Typically, close to the atom, electrons tends to have a radial symmetry whereas itinerant valence electrons are more planewave-like. Matching each of these to an appropriate single particle basis set dramatically reduces the amount of calculation time. The augmented plane wave (APW) method defines a series of ‘muffin-tin spheres’ which are centred on each of our atoms. Those well inside are described in terms of radial basis orbitals, those well outside are described in terms of plane waves.

Andersen further simplified the radial basis portion of the APW method by approximating the wavefunctions by a first order Taylor expansion with respect to energy [102]. The result is known as linearised augmented plane wave (LAPW).

### 2.5.3 Local orbit wavefunction bases

The standard LAPW method can be made more efficient by up to an order of magnitude if additional wavefunctions are included with the standard APW wavefunctions which better describe the states close to the edge of the muffin tin spheres known as the ‘semi-core states’.

These additional wavefunctions are known as ‘local orbitals’ and allow the calculation to relax the condition that the standard APW wavefunctions must have a continuous slope at the muffin tin boundary. The local orbit wavefunctions are used to smooth over the kinks where the plane wavefunctions and the radial wavefunctions meet. The functions are radial in nature but are  $\mathbf{k}$  independent. Including these wavefunctions can result in up to 50 % fewer wavefunctions required for convergence and significantly shorter calculation times [103].

### 2.5.4 Code and execution details

Calculations presented in this thesis were performed using WIEN2k version 07.2 (20th Feb 2007) [94] using LAPW without the local orbitals. Unless specified, non-spin orbit calculations are presented although spin-orbit calculations were checked and did not show significant differences. The GGA according to Perdew-Burke-Ernzerhof [100] was used for the exchange correlation functional.

Preprocessing of the WIEN2k data into voxel form as well as the theoretical angle plots were performed using a modified version of MATLAB code written by Dr. E. Yelland. The basis for the code has been thoroughly field tested within the group over a number of years.

## 2.6 Hall effect

The Hall effect is a consequence of the Lorentz force on a moving charge. To first understand this we look to the Boltzmann transport equation which allows us to use a semi-classical approach to incorporate the effects of magnetic field to find expressions for single electron transport and in particular the conductivity tensor  $\rho$ . The Boltzmann transport equation is expressed as follows,

$$\frac{\partial f}{\partial t} + \mathbf{v} \cdot \nabla_r f + \mathbf{F} \cdot \nabla_k f = \left. \frac{df}{dt} \right|_{\text{coll}}, \quad (2.6.1)$$

where  $f = f(\mathbf{r}, \mathbf{k}, t)$  is the occupation distribution for single electrons at position  $\mathbf{r}$ , in state  $\mathbf{k}$  at time  $t$  and  $\mathbf{v}$  is the electron velocity,  $\mathbf{F}$  is the force on the electron and the term on the right is the rate of change of the occupation due to collisions. The Boltzmann transport equation arises from the notion that, classically, the chance of occupation of a particular state  $f$  at  $t$  is equivalent to the probability of occupation of a state at  $f - df/dt$  at time  $t - dt$ . The fact that the equation employs classical dynamics with quantum mechanical Bloch waveforms makes this a semi-classical equation.

The collision term on the right is generally complicated and is usually approximated by the ‘relaxation time approximation’,

$$\left. \frac{df}{dt} \right|_{\text{coll}} = \frac{f - f_0}{\tau}, \quad (2.6.2)$$

where  $f_0$  is the equilibrium occupation distribution to which  $f$  tends towards exponentially if the system is perturbed. The rate of the exponential convergence is determined by the relaxation time,  $\tau$ , with the decay rate of the discrepancy being proportional to  $e^{-t/\tau}$ .

As discussed in section 2.3.1, electrons at the Fermi surface subject to a magnetic field are confined to orbits of a particular area around the Fermi surface due to the Lorentz force. Dealing solely with the simpler case of closed orbits we make an approximation of a steady state and uniform distribution so the first two terms of equation 2.6.1 are zero. We then incorporate the Lorentz force,  $\mathbf{F} = q(\mathbf{E} + \mathbf{V} \times \mathbf{B})$ , in the third term. Finally through some manipulations [104] and on assuming that  $k_b T \ll E_F$  so the Fermi distribution is a step function, then we can obtain an expression for the conductivity tensor elements,  $\sigma_{ij}$ , as the Shockley-Chambers tube integral form of the Boltzmann equation,

$$\sigma_{ij} = \frac{e^2}{4\pi^3 \hbar^2} \int d\mathbf{k}_B \int_0^{2\pi} d\phi \int_0^\infty d\phi' v_i(\phi) v_j(\phi - \phi') \frac{m^*}{\omega_c} e^{\phi'/(\omega_c \tau)} \quad (2.6.3)$$

where  $\phi$  and  $\phi'$  are angular integration variables around the orbit. From this integral it is possible to determine the conductivity tensor for a variety of Fermi surface geometries, however given the shape of the BSCO2201 Fermi surface, we are most interested in the

cylindrical Fermi surface which gives the following conductivity tensor,  $\rho$  for a magnetic field applied along  $z$ ,

$$\rho = \begin{pmatrix} \rho_{xx} & \rho_{xy} & \rho_{xz} \\ \rho_{yx} & \rho_{yy} & \rho_{yz} \\ \rho_{zx} & \rho_{zy} & \rho_{zz} \end{pmatrix} = \begin{pmatrix} 1/\sigma_0 & \omega_c\tau/\sigma_0 & 0 \\ \omega_c\tau/\sigma_0 & 1/\sigma_0 & 0 \\ 0 & 0 & 0 \end{pmatrix} \quad (2.6.4)$$

where  $\omega_c$  is the cyclotron frequency and  $\sigma_0$  is the Drude conductivity given by,

$$\sigma_0 = \frac{ne^2\tau}{m^*} \quad (2.6.5)$$

where  $n$  is the carrier density and  $m^*$  is the effective mass. The off-diagonal resistivity component represents the resistivity perpendicular to the current and in the case of  $\rho_{xy} (= \rho_{yx})$  is also perpendicular to the field then this is known as the Hall resistivity,

$$\rho_{xy} = \frac{\omega_c\tau}{\sigma_0} = \left( \frac{eB}{m^*} \right) \tau \frac{m^*}{ne^2\tau} = \frac{B}{ne} \quad (2.6.6)$$

The Hall resistivity can be understood if we consider an electron (hole) moving along a rectangular slab subject to a perpendicular magnetic field. The electrons (holes) are deflected to one side of the slab due to the Lorentz force on the charged particle. Eventually the charge density on one side becomes high enough that the Coulomb repulsion force of the density on subsequent charge carriers balances the Lorentz force and an equilibrium voltage between either side of the slab is reached. This voltage is known as the Hall voltage,  $V_H$  and is given by,

$$V_H = -\frac{I\rho_{xy}}{d} = -\frac{IB}{ned} \quad (2.6.7)$$

where  $I$  and  $B_\perp$  are the current and perpendicular magnetic field and  $n$ ,  $e$  and  $d$  are the carrier density, charge and slab thickness respectively.  $V_H$  is what is measured in our experiment. This is usually further abstracted to the Hall coefficient,  $R_H$ , which encapsulates the carrier density for a metal as follows,

$$R_H = \frac{V_H d}{IB} = \frac{1}{ne} \quad (2.6.8)$$

Provided the magnetic field is small, meaning  $\omega_c\tau \ll 1$ , then scattering prevents the formation of Landau tubes described in section 2.3.1. This is known as the low field limit. The high field limit leads to effects such as the quantum Hall effect and quantum oscillations.

### 2.6.1 Effects of Fermi surface topology

Ostensibly, a hole-like Fermi surface would be expected to demonstrate positive Hall coefficient and an electron-like Fermi surface a negative, however it is possible to obtain the exact opposite due to the curvature of the Fermi surface [71].

For a 2D metal in the weak field semiclassical limit, Ong determined that the transverse conductivity,  $\sigma_{xy}$  from which  $R_H$  is derived can be obtained by integrating the mean free path vector,  $\mathbf{l}_k = \mathbf{v}_k \tau_k$  over the Fermi surface ( $\mathbf{v}_k$  is the Fermi velocity and  $\tau_k$  is the momentum dependent scattering rate). This is illustrated in figure 2.6.1 which integrates over a Fermi surface with a long mean free path in the  $(\pi, \pi)$  direction and shows how the resulting  $\mathbf{l}_k$  traces two loops in opposite directions giving rise to a larger ‘negative’ loop from the negative curvature even though the overall surface has a positive curvature. Narduzzo *et al.* argues that this illustrated scenario is close to what we find in LSCO at

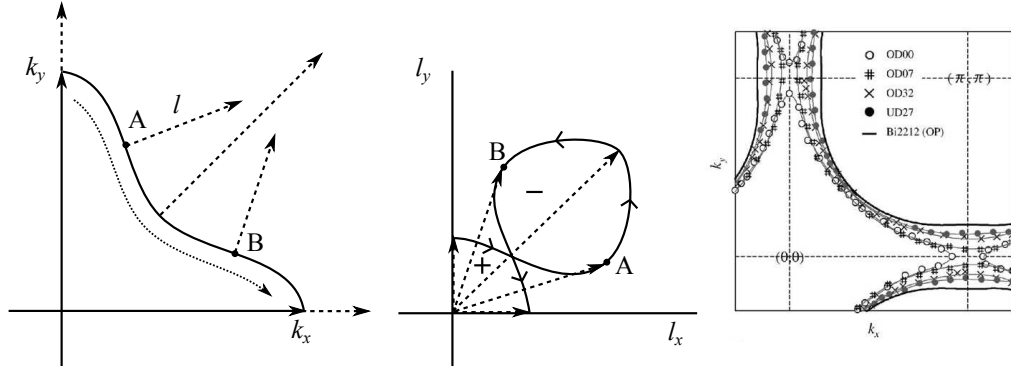


**Figure 2.6.1:** Left illustrates a negatively curved Fermi surface with a long mean free path along the  $k = (\pi, \pi)$  portion and the integral progressing along the dotted line. Middle shows how the mean free path vector changes along the integral line tracing two loops of opposite direction. Adapted from ref. [71]. Right shows the progression of the BSCO2201 Fermi surface about the van-Hove singularity. Adapted from ref. [80].

high doping [71]. Here the mean free path is affected by the anisotropic scattering rate detailed in the introduction section and the proximity of the van-Hove singularity leads to negative curvature in the long flat sides of the Fermi surface as it changes between hole-like and electron-like, as shown for BSCO2201 in the right side panel of figure 2.6.1, adapted from ref. [80].

The form of the equations set out originally by Ong [105] for a 2D metal derives a relation for the transverse conductivity,  $\sigma_{xy}$  from the Boltzmann model are as follows,

$$\sigma_{xy} = \frac{e^2}{h} \frac{2\phi}{\phi_0} \quad \text{where} \quad \phi = A_l B \quad (2.6.9)$$

where  $A_l$  is the ‘Stokes’ area traced in the centre panel of figure 2.6.1 and  $\phi$  is the flux through the Stokes area and  $\phi_0 = h/e$  is the flux quantum. The Hall coefficient  $R_H$  is

given by,

$$R_H B = \rho_{xy} = \frac{\sigma_{xy}}{\sigma_{xx}\sigma_{yy}} \quad (2.6.10)$$

where, assuming symmetric scattering along the  $x$  and  $y$  directions of the conductivity tensor then,

$$\sigma_{xx} = \sigma_{yy} = \frac{e^2}{4\pi^2\hbar} \int_0^{2\pi} k_F(\theta)l(\theta)d\theta \quad (2.6.11)$$

Contributions from isotropic scattering which affect  $\sigma_{xy}$  are cancelled in  $R_H$ , however anisotropic scattering at regions of Fermi surface of particular curvature do contribute to the Hall coefficient.



# Chapter 3

# Experimental and Computational Methods

---

This chapter begins with descriptions of how the dHvA measurements were performed, the equipment used and the analysis. Next, a description of the methods and code used to calculate susceptibility is supplied and finally descriptions of the magnetotransport measurements and analysis are detailed.

---

## 3.1 De Haas-van Alphen torque measurement

In this section the measurement of dHvA oscillations by the torque method is described. For decades, the measurement of dHvA oscillations provided the principal method of characterising the Fermiology of a material with only relatively recent competition from techniques such as positron annihilation and ARPES in particular. Whilst ARPES can provide direct maps of Fermi surfaces within the BZ, dHvA has some advantages such as the fact that it is insensitive to surface effects such as crystal reconstruction, can determine cross-sectional areas with a relatively high resolution and also provides useful secondary measurements such as effective masses of the quasiparticle carriers. Some disadvantages of the technique include the fact that dHvA cannot locate particular cross-sectional orbits within the BZ (thus relies on secondary knowledge such as DFT calculations) and also that the high magnetic fields could potentially affect the Fermi surface, for example by splitting the energy levels. Regardless dHvA continues to be a reliable technique for Fermi surface characterisation.

### 3.1.1 Experimental apparatus

Much of the experiment apparatus has already been described in great detail by Dr. C. Andrew in her thesis [106]. Here we recap and also detail the points of difference.

#### Torque cantilever

A highly sensitive measure of torque is required to pick up the moments experienced by the sample due to the field. For this reason a commercial piezoelectric AFM cantilever, provided by Seiko corporation, was repurposed to measure this. The sample was placed

onto the topside of the lever above the AFM tip. Previously this would be epoxied in place but for these measurements we tried successfully with using vacuum grease which freezes the sample in place at low temperatures. This has the added benefit of still being adjustable and removable when warmed back to room temperature. Moreover, when it comes to rotate the sample in the basal plane, this was possible by nudging the sample gently without having to move the cantilever and risk breaking the lever with the sample permanently affixed. Care should be taken not to get grease on the pivot point of the levers since this will freeze the lever in place at low temperatures. The cantilevers feature

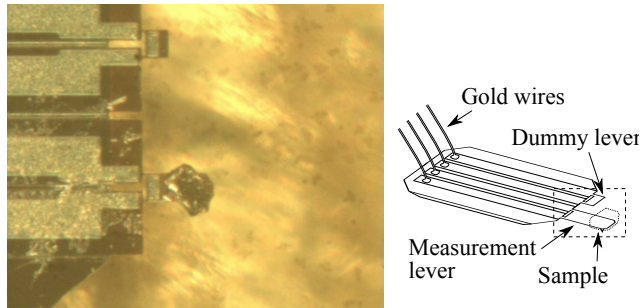


**Figure 3.1.1:** Photo of the  $\text{BaFe}_2\text{P}_2$  sample mounted on the measurement lever along with a schematic showing the full cantilever assembly. N.b. the  $\text{BaFe}_2\text{P}_2$  crystals often cleave along the [110] plane and so despite the apparent  $45^\circ$  rotation, the sample is aligned such that the lever flexes in the [100] plane.

a second dummy lever alongside the principal lever where the sample was mounted. Instead of measuring the voltage across the principle lever alone, we measure the difference of the voltages between the two levers using a Wheatstone bridge which is balanced using two  $500\ \Omega$  resistors. This enables some degree of correction due to vibrations and fluctuations in measurement current and also allow for correction of magnetoresistance effects within the levers. The circuit is balanced using a variable resistor and is zeroed as best as possible within the noise before each measurement run.

The voltage is supplied and measured using Stanford SR830 lock-in amplifier. The input supplied to the Wheatstone bridge first passes through a  $10\ \text{k}\Omega$  resistor with an excitation voltage of 1 V unless otherwise stated. The output is first amplified using an EG&G 5113 pre-amplifier with a gain of  $\times 1000$  with a band pass filter which was suitably set for the lock-in amplifier excitation frequency. All of the circuitry mentioned above, aside from the cantilevers and leads, is kept outside of the dilution fridge at room temperature and is away from the field centre by approximately 2-3 m.

### Sample stage

The cantilever is mounted onto the sample stage which is a one axis Swedish rotator fabricated entirely from Hysol epoxy resin. This is moved by an external stepper motor

controlled by a computer.

The angle of the stage in relation to the field is determined by one of two orthogonal pick-up coils mounted on the sample stage. A weak, oscillating magnetic field is generated by a coil which is wound concentrically around the inside of the main magnet coil. The AC coil induces a voltage in these orthogonal pick-up coils on the stage which is proportional to the sine of the angle they are at with respect to the field. The pick-up coil voltage is measured by a second Stanford SR830 lock-in amplifier after passing through a custom amplifier set to  $\times 100$ . The lock-in amplifier also drives the oscillating field after passing a custom built current source. The modulating coil is designed to generate an oscillating field of a few tens of Gauss whilst the main coil is in persistent mode [107].

### 20.5 T ‘Yellow’ magnet

Measurements of the oscillations were all performed in Bristol on what is informally referred to as the ‘Yellow magnet’ system. This system was built by Oxford Instruments and can nominally operate up to 20.5 T with use of the lambda plate, an additional cooling system for the magnet coil, although is more typically operated up to 18 T. The bulk of

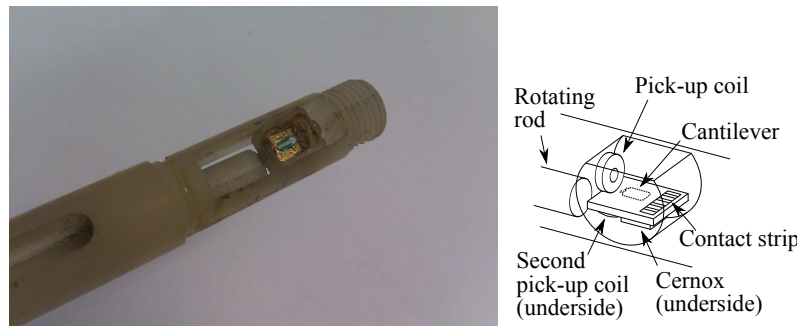


**Figure 3.1.2:** A photo of the Swedish rotator sample stage with cantilever in place and protective cap removed.

the cryostat sits in a bath of  ${}^4\text{He}$  which takes the temperature down to the helium boiling point of 4.2 K, and then the sealed sample space is additionally immersed in  ${}^3\text{He}$  gas in a Heliox system. This system condenses the  ${}^3\text{He}$  gas at the base of the chamber and pumps on it using a charcoal sorbtion pump to lower the sample stage temperature to  $\sim 0.3$  K for several hours before it has to be re condensed. Figure 3.1.3 demonstrates the condensing cycle. In general measurements are taken at base temperature but higher temperatures can be achieved by heating the charcoal sorbtion pump thus lowering the pumping rate on the  ${}^3\text{He}$  bath. This technique allows access to temperatures up to approximately 2.1 K. Temperatures greater than this are possible by heating the sample through an electric heater mounted on the magnet, however with our setup we do not accurately control temperature as the field ramps because of complications due to magnetoresistance effects in

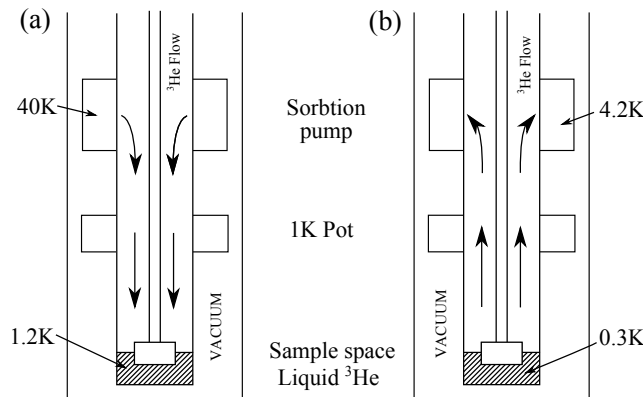


**Figure 3.1.3:** The  $^3\text{He}$  condensing cycle for the 20.5 T Yellow magnet system Heliox. (a) The sorption pump is heated so the  $^3\text{He}$  it contains is released and condenses into a fluid on reaching the 1 K pot. (b) Once a significant proportion of the  $^3\text{He}$  is condensed, then the pump heater is switched off which pumps on the liquid causing additional cooling around the sample stage to  $\sim 0.3\text{ K}$ .

the measurement thermometers. Temperature is monitored at the sample by a Cernox thermometer on the sample stage, and a RuO<sub>2</sub> thermometer which is mounted in the sample space on the cryostat but is in thermal contact with the tip of the sample stage when the stage is properly seated. Care should be taken that this is the case to ensure effective pre-cooling of the sample. Further thermometers are situated on the 1 K pot, the sorption pump and sat on top of the magnet coil although the latter is only monitored when initially cooling the magnet from room temperature. All thermometers and heaters were controlled using two Neocera LTC-21 temperature controllers.

Data are collected by a Windows PC running custom Delphi software which queues measurements and records data only. No analysis is performed in the collection software. Data are saved to text files.

### 3.1.2 Data analysis

#### Angle correction

To perform angle dependent measurements, we need to first of all measure accurately the angle between subsequent measurements and second we need to determine the angle of the field compared to the basal planes of the crystal.

In order to tackle the first problem, the pick-up coils sampling the AC field described earlier are used with the measured voltage begin proportional to the sine of the angle between the coil and the AC field. By monitoring this voltage, accurate determination of the angle between the sample platform and the field can be made and therefore the angle between subsequent measurements.

The absolute angle between the large DC field and the crystal planes in the sample were determined using a post-measurement correction. Since the frequency of the quantum oscillations are field dependent with turning points at the  $B \parallel [001]$  direction for approximately two dimensional samples, an even termed polynomial up to fourth order was fitted to the peaks. From the minima of the fits an angular offset was obtained which gave the final correction to the above coil measurements.

The basal angle was aligned on the cantilever by eye. This was coupled with x-ray diffraction (XRD) measurements which determined how the visual features corresponded to the crystal axes. This leads to an estimated error in basal plane alignment of around  $5^\circ$  although we found evidence for greater misalignment in one case, detailed in the results.

### Temperature correction

Effective mass measurements on particular extremal orbits rely on accurate temperature determination at all stages of the field sweep. On the Yellow magnet system, temperature from base of  $\sim 0.3$  K to  $\sim 2$  K is controlled by adjusting the  $^3\text{He}$  sorbtion pump temperature and is largely independent of field effects since the thermometer regulating the sorbtion temperature is outside of the strong field core. However if we consider figure 3.1.4, it is evident that there are magnetic field effects on the  $\text{RuO}_2$ , which is mounted in the base of the magnet but thermally linked with the sample, and the Cernox thermometer that sits on the sample stage. Readings from both thermometers were taken with field sweeps from zero field up to 18 T at steady temperatures 0.30 K, 0.53 K, 0.64 K, 1.06 K and 1.34 K. By interpolating between the data\*, the two thermometers can be corrected to agree within  $\sim 0.01$  K. This interpolation is however limited to temperatures below approximately 1.45 K as is shown in the figure for readings at around 1.6 K. In these cases, the less reliable method of extrapolating the readings back to zero field using a second order polynomial fit are used as demonstrated with the solid lines in figure 3.1.4. In these cases the temperature is taken to be the mean of the two extrapolated values with the differences defining the error.

### Self heating effects

The resistance across the piezo-electric lever is read by driving an AC current through it and reading the voltage across it using the Stanford lock-in amplifier. Larger currents are less prone to noise problems, however too much current results in self heating and subsequently the sample platform and sample could be at a higher temperature than the nearby thermometers suggest. To ensure that this is not the case we measure oscillations at constant temperature with a variety of driving currents. Small currents should not affect oscillation amplitudes, but at some current threshold self heating effects will become

---

\*Interpolated using multiquadric radial basis functions from the Scipy Python library.

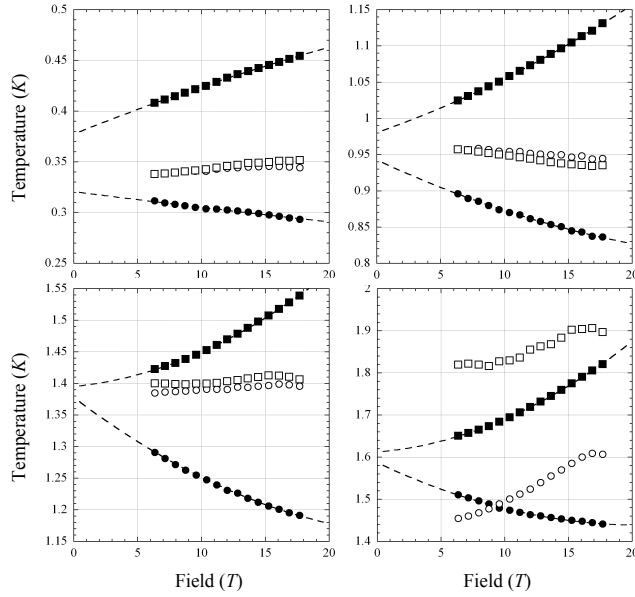


**Figure 3.1.4:** Some example temperature readings (filled symbols) set using the sorbtion pump heater. Also shown are corrections (open symbols) by interpolating to known values. RuO<sub>2</sub> thermometer is shown as circles, Cernox stage thermometer is shown as squares. Second order polynomial fits to the data are shown as lines extrapolated to zero to get a rough estimate of the zero field temperature value.

apparent and the oscillations are damped as if the entire system was operating at a higher temperature. We then resume measurements using a driving current below this threshold.

When performing this intial test, ideally the base temperature should be chosen to be where the attenuation due temperature given by equation 2.3.13 changes rapidly with temperature so that even small changes in temperature manifest in observable changes in the oscillation amplitude.

### Torque measurement factor

An extra factor affecting the amplitude of the LK oscillations occurs due solely to the nature of the torque oscillation measurement. The factor is given by,

$$A_{\Gamma(\text{gen})} = \frac{1}{F} \frac{dF}{d\theta_{\perp}} B \quad (3.1.1)$$

where  $\theta_{\perp}$  is the angle from the field direction. This can be simplified for a quasi 2d metal to,

$$A_{\Gamma} = |\sin(\theta)|B \quad (3.1.2)$$

where  $\theta$  is the angle from the cylinder axis (usually in the  $c$  direction). This means that at along the cylinder axis there will be no oscillations as  $A_{\Gamma} \rightarrow 0$ .

### Background removal

Previous standard practice was to remove a background polynomial fitted to the field or inverse field from the raw data before taking the FFT. With reference to figure 3.1.5, raw torque data taken over a range of angles\* and a strong  $B^2$  component can be observed as a result of the  $A_\Gamma$  term in the LK equation at angles away from  $90^\circ$  and  $0^\circ$ . Figure 3.1.6 shows in the centre and right panels that subtracting a second order polynomial fitted to the *inverse* field leaves a large artificial angle-dependent oscillation in  $1/B$  in the residual which may be misconstrued as a signal from a low frequency Fermi surface orbit, especially since there is an apparent angle dependence – no such peak is seen for the flat curves at  $0^\circ$  and  $90^\circ$ . For this reason it is recommended to subtract a second order polynomial fitted to field rather than inverse field for torque measurements.

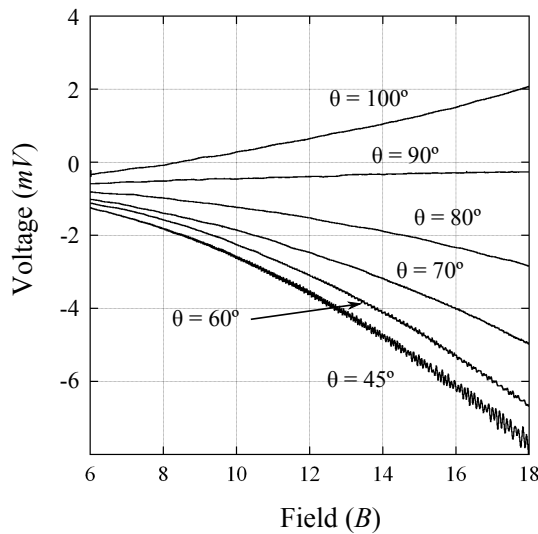


**Figure 3.1.5:** The angle dependence of the raw torque data clearly showing a negative  $B^2$  background at  $45^\circ$  and for  $\theta < 90^\circ$  and a positive  $B^2$  background for  $\theta > 90^\circ$ .

### 3.1.3 Measuring the spin mass

Other than beating effect from similar frequencies, the only terms in the LK equation that cause the amplitude to drop to zero as a function of angle are the torque term,  $A_\Gamma$  which causes a single zero when the field is parallel with the cantilever arm and the spin term  $A_S$ <sup>†</sup>. By examining the amplitude as a function of angle it is possible to determine the spin effective mass. A good determination requires more than one spin zero (i.e. a zero not due to the torque term) to be measured since the oscillatory nature of the  $A_S$  term gives multiple solutions if we only have measured a single zero. We use  $n$  to label each of

\*See section 4.3 for full details.

<sup>†</sup>The angle dependence of  $A_S$  comes from variations in the band mass.

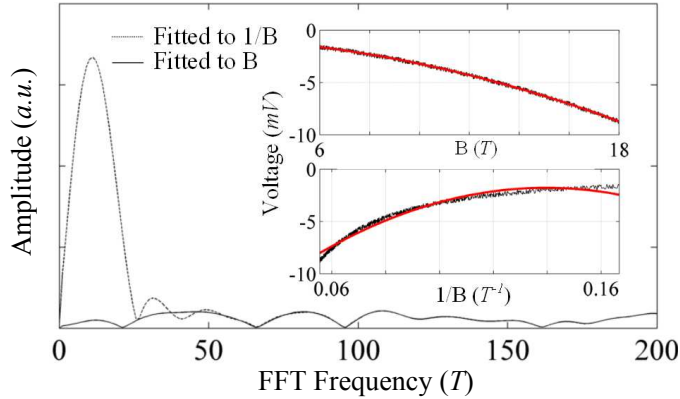


**Figure 3.1.6:** Insets show a 2nd order polynomials fitted to simulated  $B^2$  background with  $\sim 0.5$  mV of noise, similar in scale to that of  $45^\circ$  in figure 3.1.5. Upper inset is fitted to field and lower to inverse field. The main figure shows the resulting FFTs.

the zeros from the  $A_S$  oscillations.

In practice, fitting the overall shape requires all of the LK terms to be considered which makes free parameter fitting very difficult to converge. For these reasons, spin mass for this investigation is found from ansatz guesses for the values which are then fitted by inspection. Upper and lower bounds for the estimations are provided.

To the first approximation, the cylindrical approximation is used to describe the band mass in  $A_S$ , however the form of the spin term is relatively sensitive to small deviations and so fits would be much better using a more accurate variation of band mass with angle. Band mass was extracted from DFT results and was performed using MATLAB code which locates the extremal areas from the corrected BZ energy dispersion at a particular angle. Once located a small shift in energy is applied and the corresponding shift in area is used to determine the band mass using eqn. 2.3.19. A polynomial of appropriate order is then fitted to the curve and used in the fitting routine in place of the band mass. The MATLAB code determines the masses with some spread in the values which caused higher order polynomial fits to oscillate at low angles within the noise. To alleviate this, a mean value was determined for each angle.

One final note is that the absolute value of the  $A_S$  term is used to fit the data since we analyse the height of the FFT peaks of the oscillations which are always positive and not the oscillations directly.

### 3.1.4 Extracting effective mass from the temperature dependence

Of all the damping terms in the LK equation, only  $A_T$  (eqn. 2.3.13) is temperature dependent and so is used to determine the thermal effective mass. By measuring oscillations at a fixed angle but with varying temperatures, the effective mass can be determined in a number of ways.

### Basic LK formula fitting

The simplest technique to extract the thermal effective mass is to extract the amplitude of the oscillations from FFTs of the data at various  $T$  and then perform a least squares fit to eqn. 2.3.13. A particular problem with this approach is that it is not clear what value of  $B$  should be used since the FFTs needs to span a field range when ostensibly the oscillation should be measured at a particular  $B$  value. Generally the simplest thing to do is to take the FFTs over a small a range as possible and then take the field to be equal to the averaged inverse field, i.e.  $B_{\text{av}}^{-1} = \frac{1}{2}(B_{\min}^{-1} + B_{\max}^{-1})$ .

There are two conflicting problems with this approach. First the amplitude tends to decreases with narrowing field range meaning weak oscillations may require larger field intervals. Secondly wider field ranges mean other attenuation factors — which are also functions of  $B$  — affect the amplitude across the field sweep. The primary problem in this case is the Dingle term which has an exponential dependence on  $B$ . Although the Dingle term is not temperature dependent, the exponential dependence on the Dingle factor changes the amplitude of the oscillations over the field range necessary for the FFT which can affect the final amplitude. Nonetheless, simple LK fits are usually the first port of call and serve as a first approximation to the final result. For this investigation though, since we found some disagreement within the data, we employed a couple of additional techniques described below to overcome this shortcoming.

### Retrofitting ansatz LK formulae

One of the primary field-dependent contributions to the oscillation amplitude is the Dingle term scattering (eqn. 2.3.15) which has an exponential dependence with temperature. The Dingle factor,  $\alpha \equiv -\pi pm_b/e\tau$ , can be determined by fitting a simplified version of the LK equation,

$$\Gamma_{\text{sim}} = A_D(\alpha, B)\sqrt{B} \sin\left(\frac{2\pi F}{B} + \phi\right) \quad (3.1.3)$$

to oscillations which have been band pass filtered to reduce the number of contributions from other extremal orbits and hence the number of necessary fitting parameters. Once we have the Dingle term and also the peak frequency for a particular orbit, simulated oscillations are generated using the same equation but including the temperature term,  $A_T(m_T^*, B)$ , for a range of ansatz effective thermal masses. We then fit this to the LK equation as described in the previous section. The mass that results from the fit is different from the actual effective mass used as the LK fit has been affected by the Dingle term contribution. When we find a simulated oscillation that outputs the same effective thermal mass as the plain LK fit on the actual data we then take the ansatz thermal mass for that matching fit to be the corrected thermal mass.

The filtering used to originally separate out the frequencies is band pass FFT using

a Hanning window. This is adjusted in size and roll off width according to the peak. Occasionally, the peaks are too close together to effectively filter out individually and so two or three peaks were fitted at a time using a linear combination of the simplified equation above.

The initial fits were filtered using an existing Delphi program and fits to find  $\alpha$  were performed in Kaleidagraph. Ansatz fits were found using a binary search technique using a Python script.

### ‘Microfitting’ the LK formula

A second technique is to filter out the individual orbit frequency by again using an FFT filter and a Hanning window, and this time fitting small sections of sine curve ( $\sim 1.5\text{--}3$  wavelengths) directly to the filtered torque data. This gives a field dependent value for the amplitude which can then be fitted to the standard  $A_T$  form for many values of  $B$ . The result is a plot of mass values against  $B$ . Theoretically, these should plateau to give a constant value for the effective thermal mass.

Calculations were performed using a Python script to filter the data, perform the ‘microfits’ and then perform the LK fits. The script was tested using simulated data.

## 3.2 Calculating susceptibility

Code to calculate the Lindhard susceptibility was written in MATLAB \* and early versions were tested with free electron cases in 2 and 3 dimensions with results shown in figure 3.2.1. This matches the analytical results<sup>†</sup>. One caveat when dealing with the free electron case is that the energy dispersion is not periodic and as such needs to be truncated at some point in a spherically symmetric way. This truncation affects the final calculation but provided it occurs far enough from the Fermi surface then the difference is minimal. The results shown are for a calculated region that was a sphere of radius 1 with a Fermi surface radius of 0.3. Values for  $\delta(=1\text{e-}9)$  and  $\omega(=1\text{e-}9)$  are somewhat arbitrary given that the dispersion is simplified with  $\hbar^2/2m = 1$  but are given here for posterity.

The code was adapted to accept pre-generated energy dispersions as calculated with the WIEN2k DFT software and post-processed with MATLAB code. In this case, the dispersion is periodic and energies at the scattering vector  $q$  are obtained by simply ‘rolling’ the 3D matrix of energy values. Testing on this adapted code was performed by re-creating WIEN2k calculations on LaFeAsO<sub>0.1</sub>F<sub>0.9</sub> performed by Mazin *et al.* [36] and then comparing our own susceptibility calculations with those in the Mazin paper. A temperature smearing of 1 mRy was quoted which equates to a temperature of 157.88 K. A similar number of points ( $55 \times 55 \times 26$ ) were also used.

---

\*Full code is found in appendix B.

<sup>†</sup>See, for example, page 126 of ref. [90] and Appendix F of the same reference.

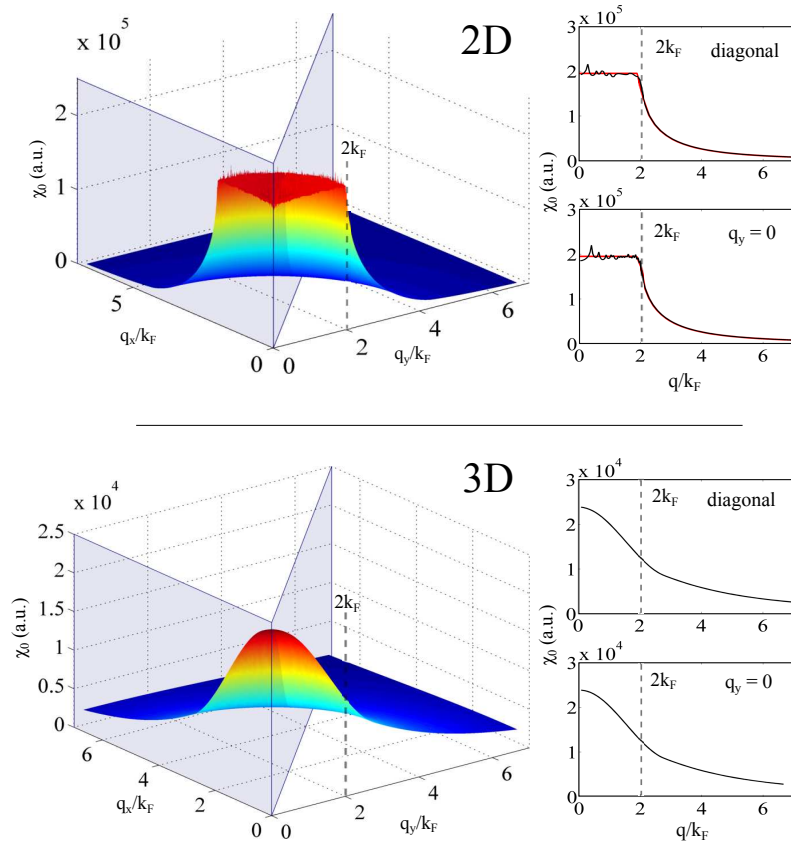


**Figure 3.2.1:** The real part of the Lindhard susceptibility calculations for a free electron model at  $T=0$  K using the MATLAB `calc_x0.m` code. Top panels are for the 2D case over a  $500 \times 500$  point grid, the bottom panels are for the 3D case taken over a  $100 \times 100 \times 100$  point grid. Panels to the right correspond to slices through the surface plots on the left with red lines corresponding to the analytical form found in ref. [84]. Calculations in the 3D case are at  $q_z = 0$ .

Figure 3.2.2 show comparisons of  $\text{Re } \chi_0(q, \omega)$  and  $\text{Im } \chi_0(q, \omega)$  with the published results. For these calculations the values of  $\delta = 1\text{e-}4$  and  $\omega = 1\text{e-}6$  were determined to give the closest results from a series of trials\*. The comparison shows that some of the finer structure from the Mazin paper is missing from our own calculations, for example the depression in the real part at the  $\Gamma$  point, however the overall shape is very similar.

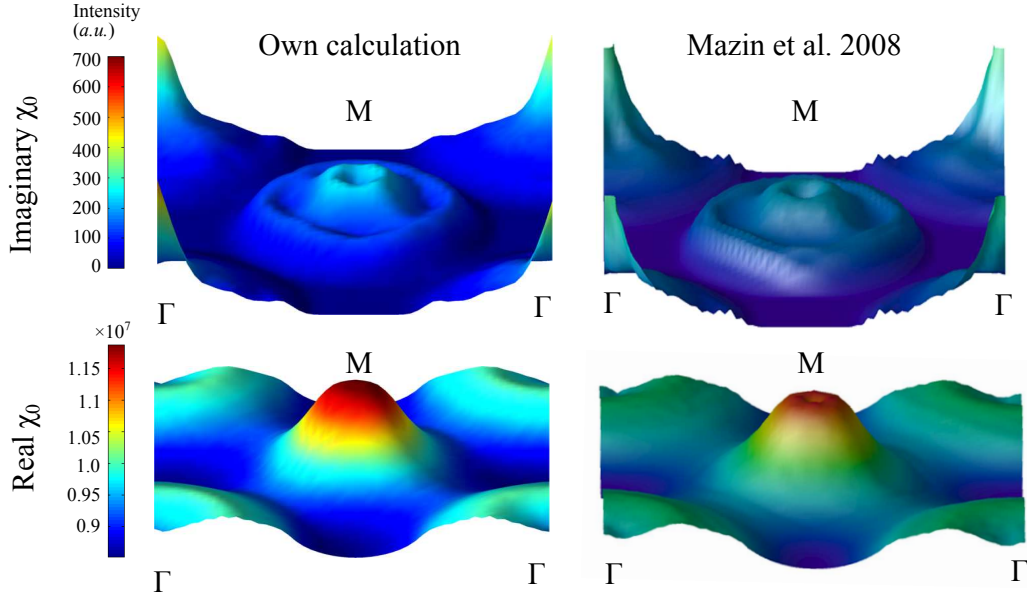


**Figure 3.2.2:** Right hand panels show the real and imaginary parts of Lindhard susceptibility calculations on  $\text{LaFeAsO}_{0.1}\text{F}_{0.9}$  by Mazin *et al.* for  $q_z = \pi/c$ , right panels show the same calculation performed using our own MATLAB code.

The Lindhard function is very sensitive to details close to the Fermi surface and finite sampling of the energy data can cause imperfect cancellation in the calculation — particularly in the imaginary part. Applying a temperature smearing to the function is useful to gloss over the finite element size in the calculation which can cause significant spikes in the results. Figure 3.2.3 shows the smearing at a series of temperatures and that a temperature of 158 K corresponds approximately to a smearing over 2 grid intervals at the Fermi surface. An appropriate choice of temperature depends on the granularity of the model as well as the expected fine detail of the results. The Mazin investigation was into a similar quasi two-dimensional pnictide material that used a comparable number of data points and so we also opted to use 158 K for the temperature smearing.

Smearing also occurs when a finite quasi-particle lifetime,  $\delta$ , is factored in and when the perturbing field is oscillatory with frequency,  $\omega$ . These values are also not known a priori and so we again look to the energy scale of the spacing between grid points close to the Fermi surface for guidance.

---

\*There is no indication in the paper as to the values of  $\delta$  and  $\omega$  used in their own calculations although we know that they are likely to be of the order of the temperature energy scale (1 mRy) or less.

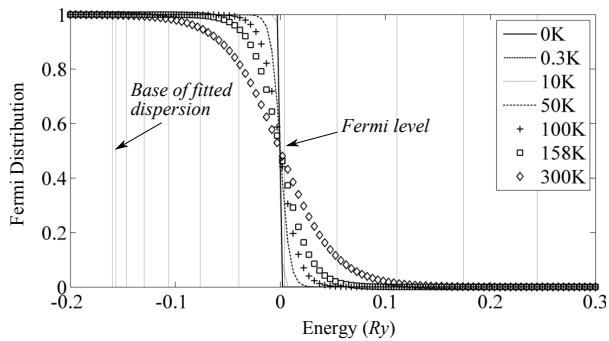


**Figure 3.2.3:** The Fermi distribution plotted at various temperatures. Vertical lines represent typical grid energy spacings for a free electron distribution fitted to a portion of bandstructure for  $\text{LaFeAsO}_{0.1}\text{F}_{0.9}$  which rounds out just below the Fermi surface. We can see that for 158 K, the smearing spans approximately 2 grid intervals at the Fermi energy.

### 3.3 Measuring charge transport

In this section the Hall measurement technique and analysis of the BSCO2201 samples is described. Transport measurements on superconductors have been performed for over a century now and was the technique by which superconductivity was first discovered. The relative technical simplicity of the measurements makes transport measurements highly appealing considering the wealth of information that can be extracted from a resistance curve.

#### 3.3.1 Experimental apparatus

##### Six probe technique

For accurate measurement of voltage, and hence resistance, across a sample, two wires are not sufficient. The wires and contacts themselves have a resistance which is comparable or often larger than the resistance of the sample being measured. A solution to this problem is to instead supply the current for the voltage reading via one set of wires, and then take the voltage reading from another set meaning that a minimum of four wires and four contacts on the sample are required. To measure magnetoresistance we require the voltage wires to be placed upstream and downstream of the current contacts, to measure the Hall effect we require the wires to be placed transverse to the current. Moreover it is useful to be able to take two transport measurements on opposite sides of the sample so as to get an idea for the homogeneity of the sample and as well to provide some redundancy in case of breakage. Since the BSCO2201 samples that we studied were to have both measurements, six connection points were placed on each sample as shown in figure 3.3.1. The connections were made with 20  $\mu\text{m}$  gold wire for the current and 10  $\mu\text{m}$  gold wire for the voltage leads and attached with DuPont 4929 conductive silver paint which dries at

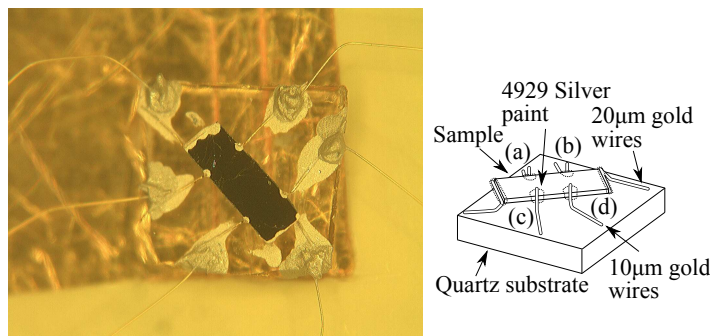


**Figure 3.3.1:** An example BSCO2201 crystal mounted on the quartz substrate. Voltage legs are labeled (a), (b), (c) and (d).

room temperature. As shown in the figure, the sample is raised from the quartz substrate so that when the temperature drops and the wires and sample thermally contract at low temperatures, there is some give so that the ensemble does not pull itself apart due to thermal contraction.

With the four voltage legs a variety of configurations can be achieved. Measuring across (a) and (b) is the magnetoresistance configuration, (a) and (c) is the Hall configuration. It is also possible to measure across (a) and (d) and provided the field is reversed from positive to negative, both the Hall and the magnetoresistance across the sample can be extracted.

Because the connections may not be exactly aligned and because the silver paint in practice tends to wet over the edge of the sample, magnetoresistance contributions may be found in the Hall configuration and vice-versa. For this reason it is generally advised to sweep both with a positive field to obtain  $R_{\text{pos}}$  and a negative field to obtain  $R_{\text{neg}}$  where  $R$  is the resistance and separate the two out using the technique described in the analysis section.

Later as the samples have been measured many times and thermal cycling had caused the silver paint to become brittle, it was necessary to attach short,  $\sim 2$  mm, secondary gold wires to each of the contact pads using silver paint and then attach the probe flying leads to the end of these wires. When removing the samples from the probe, this allowed the joins to be immersed in solvent held in the tip of a pair of metal tweezers at a safe distance from the sample ensemble meaning the connection could be dissolved without flexing the contact pads unnecessarily. This was done for the later measurements in the 16 T ‘Polo’ magnet where the minimisation of wire loops was not so important.

### 16 T ‘Polo’ magnet

The system informally referred to as the ‘Polo’ magnet is a cryostat from Cryogenic Ltd. containing a variable temperature insert (VTI) refrigeration device that allows temper-

**Table 3.1:** Operating the VTI under various temperature regimes.

Temperature range	Practice
1.4 K – 4.2 K	Fill VTI chamber with helium, close off needle valve and adjust the pumping rate to tune the temperature.
4.2 K – 300 K	Empty the VTI of helium and open the needle valve slightly, only pump a small amount and use the sample heater to set the temperature.

ature from  $\sim 1.4$  K to room temperature to be achieved. The VTI system is a vacuum sealed chamber in to which the sample probe is inserted and sealed at the top. This chamber is insulated from a bath of  ${}^4\text{He}$  in the main cryostat by a vacuum jacket.  ${}^4\text{He}$  is admitted into the VTI chamber from the bath via an adjustable needle valve and is pumped through the chamber and over the sample by an external roughing pump. By almost closing off the needle valve entirely and applying a heater on the sample stage the full range of temperatures can be achieved. In practice, a couple of temperature ranges are defined which require different operational techniques and are specified in table 3.1. The VTI chamber itself has an electric heater which can be operated separately and is good for rapidly heating the system up to room temperature but is in general too coarse for measurements.

Heating is controlled by a Lakeshore 340 temperature controller with the sample stage heated from the heater output and the VTI heater controlled from the analogue output which has been boosted via a custom built amplifier unit. Sample temperature is monitored by a Cernox mounted onto the sample stage and VTI temperature from a thermometer mounted inside the VTI chamber.

The sample stage can be rotated by an external stepper motor which is supplied from a custom power source. All the instruments mentioned are controlled from a custom PC running a Delphi program written by Dr. M. French which queues runs, records and displays data. Some calculated values based on the raw data values are generated by the software, however these were not configured with the appropriate inputs. For this reason the angle and the current fields should be ignored and instead determined from raw data.

For twin voltage measurements, two Stanford SR830 lock-in amplifiers were used with one supplying the current and measuring voltage and the second synchronised to the first and also measuring a voltage. The current supplied was supplied through a  $1\text{ k}\Omega$  buffer resistor in order to approximate the supply to a current source\*. The resulting

---

\*A current source can be approximated if  $(R_{\text{sample}} + R_{\text{wires}}) \ll R_{\text{buffer}}$  at all  $T$ . The current is then given by  $V_{\text{excitation}}/R_{\text{buffer}}$ .

voltages were passed through two passive Princeton Applied Research model 1900 low noise amplifiers set to  $\times 1000$  before measurement although the actual amplification for typical resistances of  $10\text{--}100\Omega$  at 33 Hz is  $\times 980$ .

The sample probe has a rotating stage and so after aligning the sample roughly by eye, a shallow angle sweep in a low field, typically 1 T, was performed before each measurement to make sure the sample was positioned perpendicular to the field. Some samples have an anisotropy in the transport terms and in the case of the Hall component, the effective field drops with the cosine of the angle of misalignment.

The magnet is superconducting and has a limit of 14 T or 16 T when using the additional cooling of the Lambda plate. For this thesis the measurements were only taken to 13 T to minimise the risk of a quench. The field was ramped at 1.4 T/min. The measurements presented in this thesis from the 16 T Polo magnet are all taken in the Hall configuration and are obtained by averaging both sets of contacts as described in the analysis section.

As of Feb 2012 it was determined using a Cu sample that a positive reading of the magnet power supply current (and field) with the leads wired up correctly (i.e. positive to positive, negative to negative) corresponds to the magnetic field,  $B$ , in the Polo magnet pointing upwards. This was verified with a magnetic compass.

### **HFML Nijmegen**

To access the normal state of the higher  $T_c$  materials we require fields larger than the 13 T available in the Polo magnet at Bristol. The High Field Magnet Laboratory (HFML) facility in Nijmegen has available a continuous field Bitter magnet which can reach 33 T. Data from Nijmegen in this thesis was taken in May 2010 by Dr. X. Xu, I. Mouzoupoulou, Dr. P. Rourke and Dr. A. McCollam.

The magnet used at the HFML sweeps at a rate of typically 3 T/min meaning the temperature can drift significantly. The necessary heating supply for temperature control was alternated between a Lakeshore 340 temperature controller which uses input from a Cernox thermometer and a PID algorithm to supply an appropriate current or a Keithley current source which supplies a fixed current. The current source was selected on a sweep-by-sweep basis depending on which gave more stable temperatures. The analysis compensates for small drift using a simple correction described later.

The samples were measured using Stanford SR830 lock-in amplifiers which were supplying via  $1\text{ k}\Omega$  resistors with a  $10\Omega$  shunt resistor. A 1 V excitation voltage was used for all samples except for B00KOD1a and B16KOD1a where 2 V excitation was used instead. The excitation frequency is set to one of the ‘magic’ frequencies\* which in this case were 33 Hz, 77 Hz, 113 Hz and 123 Hz.

---

\*Frequencies that do not fall near common sources of noise or their harmonics e.g. 50 Hz from mains supply.

Field is monitored using a calibrated Hall sensor mounted on the probe which is measured using another Stanford SR830 lock-in amplifier.

### LNCMI Toulouse

To obtain the highest fields we took measurements at the Laboratoire National des Champs Magnétiques Intenses (LNCMI) pulsed field facility in Toulouse over the course of two separate visits. Here large capacitor banks are discharged through liquid nitrogen cooled copper resistive magnets to achieve short (few tens of microseconds) but strong fields of up to 60 T. Pulses at the stronger end of the scale have more potential for damaging the magnet and take longer to cool down before the next pulse can be taken and so careful consideration is required to the magnitude of pulse undertaken. Typically the cooling time is around 15 to 30 minutes. The field is measured using a calibrated pick-up coil. The first trip took place in June 2009 and involved B. Arnold, Dr. P. Rourke, Dr. B. Vignolle and Prof. C. Proust. the second trip occurred in February 2010 and involved Dr. P. Rourke, Dr. J. F. Mercure, Prof. N. Hussey, Dr. B. Vignolle and Prof. C. Proust.

The results are recorded using a pair of Stanford SR830 lock-in amplifiers after passing through an active INA103 pre-amplifier set to a gain of  $\times 200$ . The raw signal for the pulse duration is recorded and the lock-in algorithm is post-processed in software to avoid wasted pulses due to incorrect settings. The driving current is supplied by the lock-in amplifier and unless otherwise noted is 5 V through a  $1\text{ k}\Omega$  resistor giving a current source of 5 mA. The driving frequency is typically very high to sample the data over the relatively short pulse time and for these experiments is typically 60 kHz. The data is streamed via an optical link along glass fibres (so the chamber remains electrically isolated for safety during a pulse) to an external PC.

Cooling down to  $\sim 1.4\text{ K}$  is possible by pumping on the helium in the magnet bath. Higher temperatures could be achieved by pumping out the exchange gas and heating via a Lakeshore 340 temperature controller. Although pulses are very short lived, there is a risk of the rapidly changing field inducing a current in the leads and sample which cause heating of the sample during the pulse. For this reason great care is taken to minimise current loops by minimising the non-twisted portion of the wires leading to the sample. Furthermore, the sample is physically jolted by the high field which can adversely affect the data, for this reason, vacuum grease is carefully applied to the sample ensemble to reduce movement.

For the first Toulouse visit, the measurements were taken in the magnetoresistance configuration, the second Toulouse visit measured the samples in the diagonal configuration.

### 3.3.2 Sample size determination

The length and the width of the samples were determined from calibrated optical microscope screen captures. The thickness was determined post transport measurements with the help of Dr. P. Heard using a FIB. This images samples by rastering a focused beam of ions onto the sample surface and measuring the amount of ejected electrons or ions from the image. This process causes electrical charging of the surface which can in turn adversely affect the path of the highly focused incoming ions and so the sample to be imaged must be earthed in order to remain electrically neutral. For these samples, a line of 4929 silver paint was drawn between the contacts and the sample mounting puck.

### 3.3.3 Data Analysis

#### Isolating Hall and magnetoresistance (MR) components

When measuring transport in a sample, there will always be contributions from both the MR and the Hall components due to imperfect geometry of the voltage pick up points. Since the Hall component reverses sign as the polarity of the field reverses whereas the MR component is independent of field polarity, the Hall and MR components can be separated out using the following relations,

$$R_{\text{Hall}} = \frac{1}{2}(R_{\text{pos}} - R_{\text{neg}}) \quad (3.3.1)$$

$$R_{\text{MR}} = \frac{1}{2}(R_{\text{pos}} + R_{\text{neg}}) \quad (3.3.2)$$

where  $R_{\text{pos}}$  and  $R_{\text{neg}}$  are the resistances measured for the positive and negative field polarities. This requires data to be taken from the positive field maximum down to the negative field maximum and so for example with the Toulouse pulsed field apparatus, two pulses are required for each measurement.

#### Correcting for temperature variations

Figure 3.3.2 shows a comparison of typical field sweeps for the LNCMI and Nijmegen facilities and the Polo magnet. The LNCMI pulse length is  $\sim 150$  ms and as such is not typically subject to slow temperature drift throughout the duration of the pulse. However the positive and negative pulses are typically taken with at least a 30 min interval in-between pulses meaning the positive and negative pulses may not be at precisely the same temperature. As such, a small offset is applied to bring the zero field data into line between positive and negative pulses. For the longer sweeps such as the Nijmegen data sets, an additional offset was applied to the measurement which is proportional to the temperature as detailed below,

$$R_{\text{corr.}} = R_{\text{meas.}} + F(T_{\text{base}} - T_{\text{meas.}}) \quad (3.3.3)$$

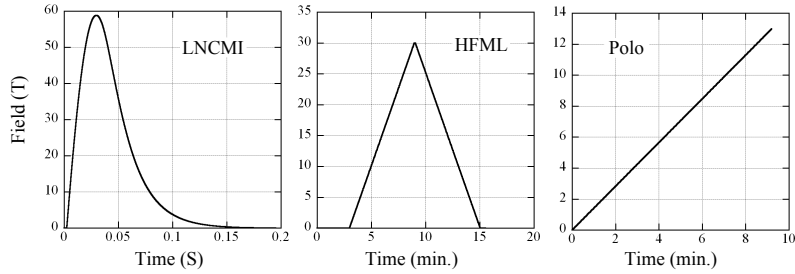


**Figure 3.3.2:** From left to right: Typical field sweep profiles for a pulse at the LNCMI, Toulouse, a continuous positive sweep at the HFML, Nijmegen and single positive upsweep for the Polo magnet, Bristol.

where  $R_{\text{corr.}}$  is the corrected resistance,  $R_{\text{meas.}}$  is the measured resistance,  $T_{\text{base}}$  is the temperature that the resistance values are converged towards and  $F$  is an empirical scaling factor that brings the upsweep and downsweep data into line. The empirical factor was determined by inspection using the following method.

1. Take data where there is a clear component that is due to the temperature drift and find the appropriate factor so that it disappears. Take these data as reference benchmarks.
2. Where the temperature component is not so clear, use the reference data and make an informed estimate of the factor based on resistance vs. temperature curves in zero field and 13 T

The same factor is applied to both the positive and negative sweeps to avoid introducing artificialities into the Hall gradient. For the Polo data the temperature control was such that no correction was necessary.

### Field lag correction

The Polo magnet has no sensor to measure field at the sample, with the field values being calculated from the power supply current. In the data there is evident hysteresis in all sweeps and is illustrated in figure 3.3.3 which suggests that the actual field lags slightly behind the indicated field possibly due to induction effects in the magnet coil and/or the power supply. To correct for this, the upsweeps and downsweeps were shifted towards each other until they overlapped, typically each by around 0.2 T. Any values which were corrected to less than 0 T or more than 13 T were then not used in the analysis.

### Combining up and downsweeps

For all the data values there is an upsweep portion and a downsweep portion which overlap and are averaged together to reduce noise. However many portions of data have regions

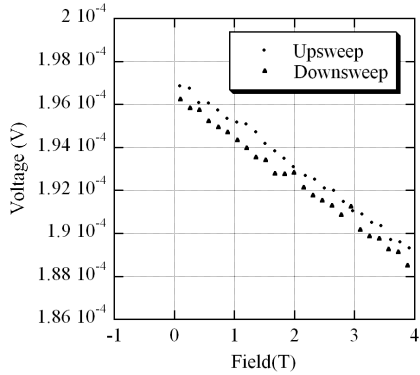


**Figure 3.3.3:** An example of the measured voltage of separate up and downsweeps which demonstrate the lag in actual field compared to the indicated field.

which drift due to changes in the out-of-phase component or anomalies such as spikes and so in these cases the regions are recorded in a configuration file and the scripts that combine the sweeps ignore the problem regions and instead use data from the counterpart sweep in isolation. Similarly, when hysteresis is encountered in the pulsed data, by convention the upsweep is ignored since it is more rapid than the downsweep which generally results in more spikes and out of phase problems.

To obtain the Hall and MR components using equation 3.3.1 we need to obtain comparable data points with shared field values. To do this one of two technique was employed. For the high-field data, this is done by binning the data and taking the average of the values in each of the bins so that they share the same field values. The data taken from the Polo magnet is linearly interpolated to a predefined set of field values.

### Linear fits to Hall data

Hall data for all samples were fitted using a standard linear least squares fit which was performed using Python for the Polo data and Delphi for the high-field data due to the different preprocessing requirements described in the previous section. A cutoff is specified so that only the data above the cutoff is fitted in the region where the linear behaviour is recovered. The cutoff value is found by inspection of the Hall data with reference to the MR component. The precise point where linear behaviour is recovered is not always clear and so two cutoffs were specified which defined the upper and lower bounds for the start of the linear region. The limits contribute to the error in the Hall gradient with the final gradient being taken as the average of the fits from the two cutoff limits.

### Normalising the high field data

The Polo data was taken in the Hall configuration and so corresponds to the true Hall voltage, whereas the data from the first visit to the LNCMI was on sample measured in the MR configuration and so represent some unknown fraction of the true Hall voltage. Moreover, the rest of the high field data was taken in the diagonal configuration meaning the voltage path was over a different portion of the sample to the Hall measurement which again means the Hall voltage is scaled by some factor. For these reasons the Polo magnet measurements were taken as the canonical absolute values for the Hall data, with the high field data scaled so that concurrent data at higher fields aligned, this process along with the variation between fits using the two different cutoff bounds define the error bars in the data.

#### 3.3.4 Determining the doping

Three techniques have been identified for determining the doping for this thesis. The most simple and well known method for determining the doping of a material utilises the so-called ‘universal’ Tallon relation [75] which links  $T_c/T_c(\max)$  to  $p$  as follows,

$$T_c/T_c(\max) = 1 - 82.6(p - 0.16)^2 \quad (3.3.4)$$

This relation was established based on measurements of  $\text{La}_{2-x}\text{Sr}_x\text{CuO}_4$  (LSCO) which exploit the direct relation between Sr content and the doping (assuming stoichiometric oxygen).

The second technique, particular to BSCO2201, was published by Ando *et al.* [76] in 2000 where samples of BSCO2201 were compared with Hall measurements of other cuprates where the carrier concentration is more easily determined, in particular LSCO was used again. The results lead to a very different relation between  $T_c/T_c\max$  which confined superconducting samples to a much narrower range of dopings\* and is given by the following relation,

$$T_c/T_c(\max) = 1 - 254.3(p - 0.16)^2 \quad (3.3.5)$$

which was extracted from the Ando paper based on dopings determined by La concentrations.

There is however some doubt as to whether it is appropriate to compare LSCO and BSCO2201 measurements across the superconducting dome, especially with regards to Hall measurements, given the proximity of the van-Hove singularity in LSCO which should lead to a depression in the apparent carrier density above  $p = 0.18$ .

The final technique is by comparing instead BSCO2201 and Tl2201 which have very

---

\*The justification being that increasing disorder suppressed  $T_c$  as you move away from optimal doping.

similar structures, and van-Hove singularities at much higher doping than LSCO\*. Doping in Tl2201 has been well characterised in the overdoped side through recent dHvA experiments [109] which maps well to where the majority of our BSCO2201 samples lie. Here the doping is determined using the Tallon relation for underdoped to slightly overdoped samples with  $T_c/T_c(\text{max})$  down to 0.71, below this value a linear relation is used:  $T_c/T_c(\text{max}) = 2.390 - 7.696p$ . Again some a priori knowledge of the approximate location (i.e. overdoped or underdoped) on the superconducting dome is required and further investigation may be required to determine which side of the dome a sample lies.

---

\*Tl2201 has a van-Hove singularity at a much higher doping than even BSCO2201. At  $p = 0.26$  (or rather  $p = 1.26$ ), ARPES measurements have shown the van-Hove singularity in Tl2201 lies a few eV below the Fermi energy [108].

# Chapter 4

## dHvA measurements on BaFe<sub>2</sub>P<sub>2</sub>

---

This chapter presents results based on the motivation outlined in section 1.2.4 including definitive measurement of the Fermiology of BaFe<sub>2</sub>P<sub>2</sub> and extensive data and analysis in to the thermal and spin effective masses. The nesting conditions along the  $(\pi, \pi)$  vector were investigated through calculations based on insight gained from the measurements and partial nesting was found along  $q = (\pi, \pi, k_z)$  where  $k_z = 0, \pi/2, \pi, 3\pi/2, 2\pi$ . Given BaFe<sub>2</sub>P<sub>2</sub> is not superconducting this suggests that partial nesting is not a sufficient condition for superconductivity.

---

### 4.1 Sample synthesis

Several samples in the BaFe<sub>2</sub>(As<sub>1-x</sub>P<sub>x</sub>)<sub>2</sub> series were measured using dHvA at Bristol in the ‘Yellow magnet’ system described in section 3.1.1, however this chapter focuses on a sample of BaFe<sub>2</sub>P<sub>2</sub>. The sample is a single crystal and has approximate dimensions 77  $\mu\text{m} \times 54 \mu\text{m} \times 15 \mu\text{m}$  as determined by optical microscope\*. The crystal was grown by T. Shibauchi in Kyoto using the following technique detailed in Kasahara *et al.* [39].

A stoichiometric mixture of Ba flakes and FeP powder was placed in an alumina crucible and sealed in an evacuated quartz tube. It was heated up to 1150–1200 °C, kept for 12 h, and then cooled slowly down to 800 °C at the rate of 1.5 °C/h. Platelet crystals with shiny [001] surface were then preferentially extracted and characterised to find single crystals of high crystalline quality. The size of the sample precludes resistivity measurements, however it was possible to examine the samples though Laue x-ray diffraction.

### 4.2 X-Ray Diffraction

The crystalline axes of the sample were determined by x-ray diffraction (XRD) on a Kappa Apex II single crystal diffractometer by Dr. I. Guillamon and Prof. A. Carrington with the aid of Dr. M. Haddow. The sample was mounted on a glass rod and held in place using vacuum grease. Clear diffraction spots are visible on the example scans shown in figure 4.2.1 although there is some evidence of a second, misaligned phase with the doubling of the spots in a small number of the scans such as the one in the top left panel.

---

\* An image of the crystal mounted on the AFM cantilever is shown in the experimental methods chapter.

There is also further evidence of secondary phases as some peaks are doubled up in the dHvA data presented later. We have no reason to believe however that these speculated misalignments are significantly affecting the rest of the body of results nor that they affect the conclusions in any appreciable way.

Perhaps surprisingly, the straight edge of the crystal was found to lie along the [110] direction and not along the unit cell axis. This was found to be the case for a number of other  $\text{BaFe}_2(\text{As}_{1-x}\text{P}_x)_2$  crystals which were x-rayed later in the year.

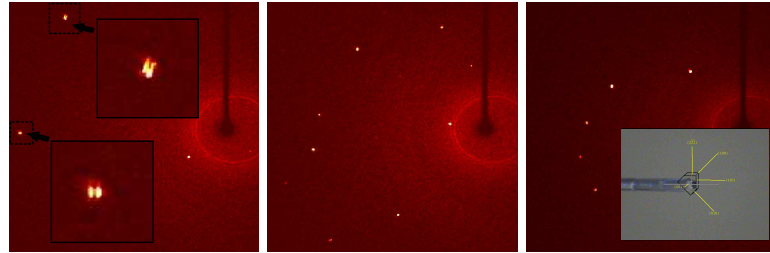


**Figure 4.2.1:** Panels show example diffraction patterns of the  $\text{BaFe}_2\text{P}_2$  sample. Left shows a zoomed portion of doubled peaks indicating that there may potentially be a misalignment within the crystal. Right inset shows the labelled crystal axes superimposed on the sample which is mounted on a glass rod.

Lattice parameters are determined using the Apex II software and are presented in table 4.1 along with comparisons to two previous measurements found in the literature. The result agree within the error.

**Table 4.1:** Lattice parameters from XRD measurements compared with literature.

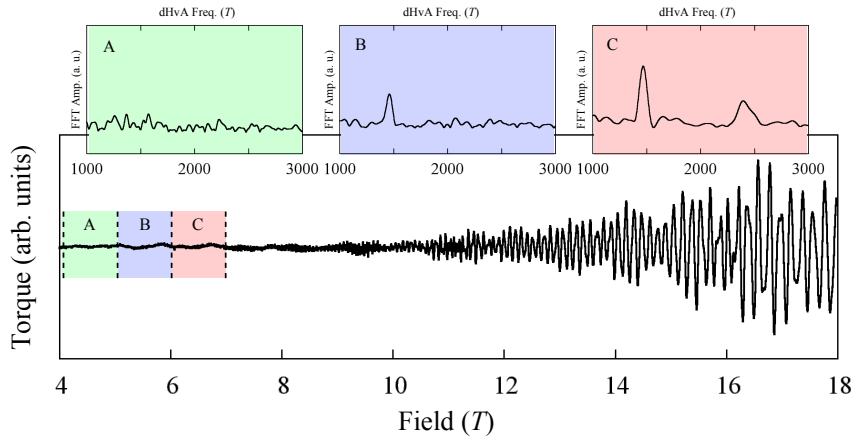
Source	$a$ (Å)	$c$ (Å)	$z_P$ (% $c$ )
X-ray	3.86(4)	12.42(9)	
Rotter <i>et al.</i> [110]	3.8435(4)	12.422(2)	34.59(1)
Mewis <i>et al.</i> [111]	3.8400	12.4420	34.560

## 4.3 Angle dependent measurements

### 4.3.1 Determining experimental parameters

Preliminary measurements showed very strong dHvA oscillations in comparison to other samples which begin at relatively low field with an example of the raw data shown in figure 4.3.1. Since it is not clear from the raw torque data where the oscillations begin, Fourier transforms were taken with small (1 T) field intervals — the interval where a clear signal is present marks the onset of oscillations. An FFT of the data for the ranges 4-5 T,

5-6 T and 6-7 T are shown in the insets of the figure. The range 6-7 T clearly shows the strong peaks at around 1500 T and 2450 T, with the higher frequency peak disappearing in the 5-6 T range and both peaks disappearing in the 4-5 T range. Further refinement suggests the onset of appreciable oscillations is around 5.6 T for the strongest peak. The field was ramped between 6 T and the safe maximum of 18 T for the vast majority of measurements bar some sweeps where the magnet was ramped to or from 0 T following or preceding shut-down of the magnet.



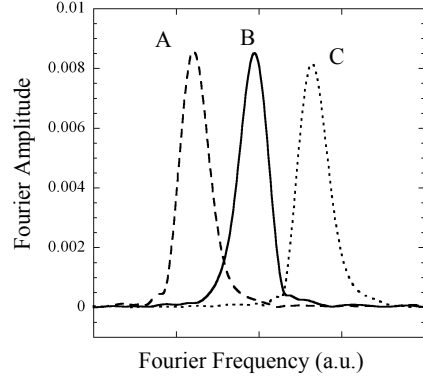
**Figure 4.3.1:** An example of the torque data taken with field aligned at  $26^\circ$  on the reverse side of the [001] to [100] angle sweep detailed later. Insets show a FFTs of the data between 4-5 T, 5-6 T and 6-7 T respectively. These intervals are marked on the main plot as A, B and C.

Figure 4.3.2 shows some example Fourier transforms of data taken at various field sweep rates and plotted with the frequencies shifted arbitrarily for ease of comparison. The difference in amplitude between the sweeps at  $0.05 \text{ Tmin}^{-1}$  and  $0.1 \text{ Tmin}^{-1}$  is less than 1 % whereas the difference when sweeping at  $0.2 \text{ Tmin}^{-1}$  is nearly 5 %. Unless otherwise stated, subsequent sweeps were performed at  $0.15 \text{ Tmin}^{-1}$  at the edge of where the sweep rate makes a significant difference in amplitude.

In order to make a reasonable determination of the Fermi surface of a material, an appropriate number of angle sweeps need to be made to adequately constrain the shape of the Fermi surface. Measurements were taken at one degree intervals from  $H \parallel [001]$  down to  $H \parallel [100]$  and from  $H \parallel [001]$  down to  $H \parallel [110]$  which, in this system of tetragonal symmetry map to six other symmetric directions.

In general, runs were performed with an excitation voltage of 1 V. To ensure that there were no self heating effects, runs were also performed with an excitations voltage of 0.5 V and 2 V at  $T \approx 0.6 \text{ K}$  (where the LK curve is steep) and no change in oscillation amplitude due to heating was observed. All dHvA measurements described on BaFe<sub>2</sub>P<sub>2</sub>were performed by the author at Bristol in the 20.5 T ‘Yellow magnet’ system.

The magnetic field was alternately ramped up and then down meaning subsequent



**Figure 4.3.2:** FFTs showing the peak from the smaller branch of band 3 taken at, A:  $0.05 \text{ Tmin}^{-1}$ , B:  $0.1 \text{ Tmin}^{-1}$  and C:  $0.2 \text{ Tmin}^{-1}$ . The peaks are arbitrarily shifted in frequency for ease of comparison. Measurements taken with  $H$  at  $10^\circ$  from [001] in the [110] direction.

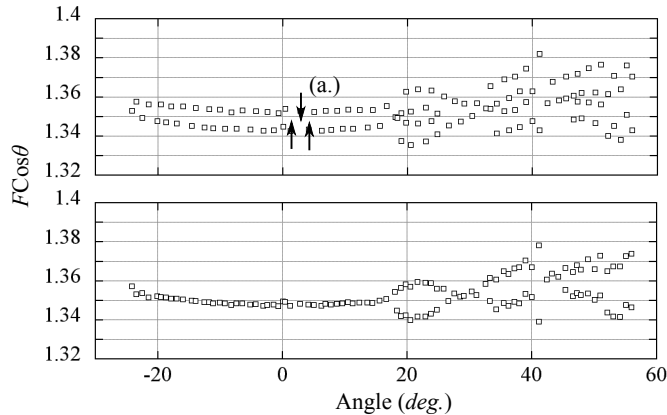


**Figure 4.3.3:** The plots show the  $F \cos \theta$  for the  $\alpha$  branch in the [100] direction. Top panel shows the branch with the hysteresis due to field sweep direction, the bottom panel shows the data after the linear adjustment described in the main text. Arrows at point (a.) show how the points were shifted.

measurements were generally performed with the magnetic field ramping in opposite directions. Although in theory this should not affect the results in any way, subsequent FFT peaks appeared to alternately be shifted by up to  $\sim \pm 21$  T with the magnitude of the shifts being roughly proportional to frequency. Assuming that the shifts were an artefact of the measurements, possibly due to slight shifts in the measured phase due to induction effects in the magnet, a linear correction determined by visual inspection was applied of  $F_{\text{corr.}} = 3 + \frac{10}{8000} F_{\text{meas.}}$  for the sweep in the [100] direction and  $F_{\text{corr.}} = 0 + \frac{21}{8000} F_{\text{meas.}}$  and  $F_{\text{corr.}} = 0 + \frac{18}{8000} F_{\text{meas.}}$  for the two sets of measurements performed to complete the sweep in the [110] direction. Figure 4.3.3 shows an example of these hysteric shifts and the subsequent correction applied.

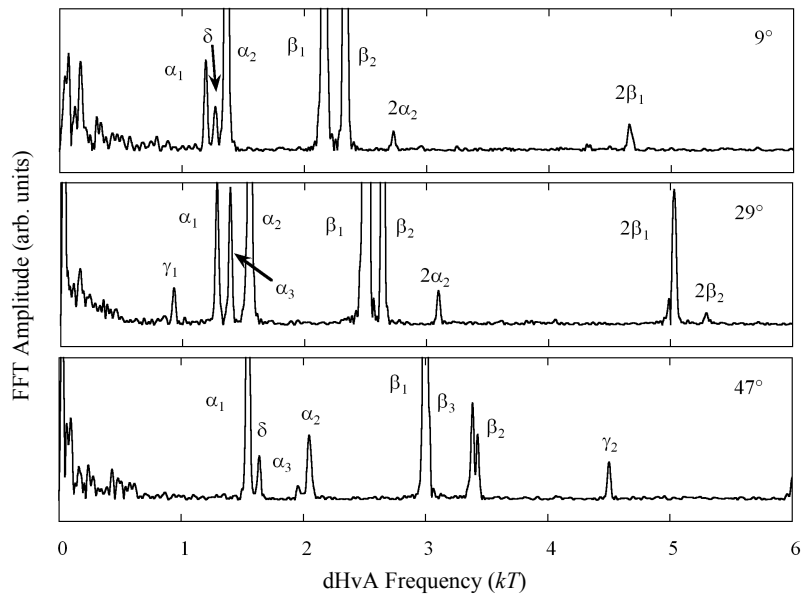


**Figure 4.3.4:** FFT after a second order polynomial background was subtracted at various labelled angles between [001] and [110]. The labels for peak identification are explained in the next section.

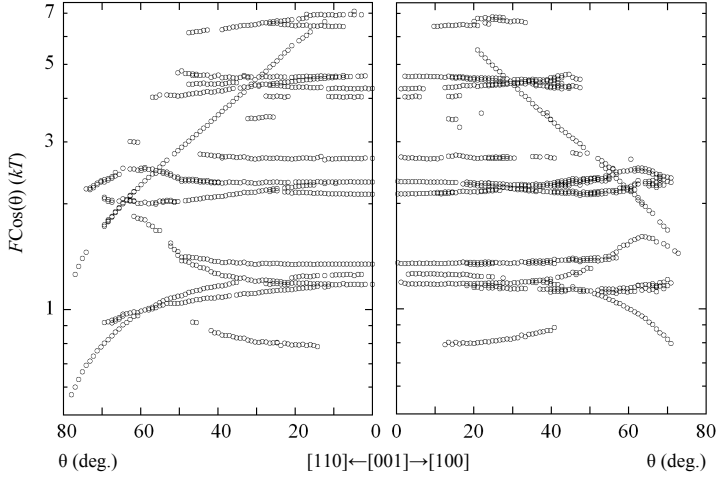
Figure 4.3.4 shows three example FFTs which show peaks from all the principal bands identified the next section. They also show first and second harmonics\*. The low frequency region in figure 4.3.4 shows noise from the cantilever, but according to DFT fits performed in the next section, this region also likely contains signal from the minimum of the inner hole band. Given that the signal from electron bands is generally small due to high scattering rate, we were not able to extract a convincing Fourier peak.

Figure 4.3.5 shows the FFT frequency of peak data multiplied by  $\cos \theta$  after having the angle determined as described in section 3.1.2. Signal can be observed up to relatively high angles with peak observed almost up to  $80^\circ$  in the [110] direction which, along with the observation of third harmonics, and the onset of oscillations in relatively low field is

---

\*Third harmonics were also identified in other FFTs, these are shown in figure 4.3.5.

testament to the high quality of the crystal.



**Figure 4.3.5:** Peaks identified by varying the field range, window type and background polynomial. Left panel shows data taken with the field parallel to [001] down to [110], the right panels shows [001] to [100].

The left panel in figure 4.3.6 shows the measured rotation data (circles) for the plots towards the [100] direction and in addition the data from the  $x = 0.63$  data in the  $\text{BaFe}_2(\text{As}_{1-x}\text{P}_x)_2$  series multiplied by amounts commensurate to the expected shifts in the Shishido paper [20] (black squares). We can see that while the size of the areas changes between the two values, the overall shape of the  $x = 0.63$  data matches reasonably well with the data for  $x = 1$  for bands 2, 3 and 4 at least. Assuming that nothing exotic happens in the intermediate range, we can extrapolate the shape of these Fermi surfaces across the range by applying the known electron Fermi surface areas and the compensation condition. This is explored further in the next section.

### Rigidly shifting the calculated DFT energies

The right panel of figure 4.3.6 shows the DFT calculations performed using the local augmented plane wave method plus local orbitals method including spin orbit coupling as implemented in the WIEN2k package [94]. The calculations in the thesis was from based on calculations originally performed by Prof. T. Carrington and recalculated by the author. The unit cell used was that measured by Mewis *et al.* which are listed in table 4.1 and the subsequent DFT calculations were processed into rotation plots using MATLAB code. Results are shown superimposed over the measured data. By factoring the frequency with  $\cos \theta$  it becomes clearer which of the orbits is a maximal extremum and which is a minimal extrema. Using this knowledge as well as clues from the Fourier amplitude of the measured data, it was possible to separate out individual bands which have been colour coded and labelled — according to literature convention — as specified

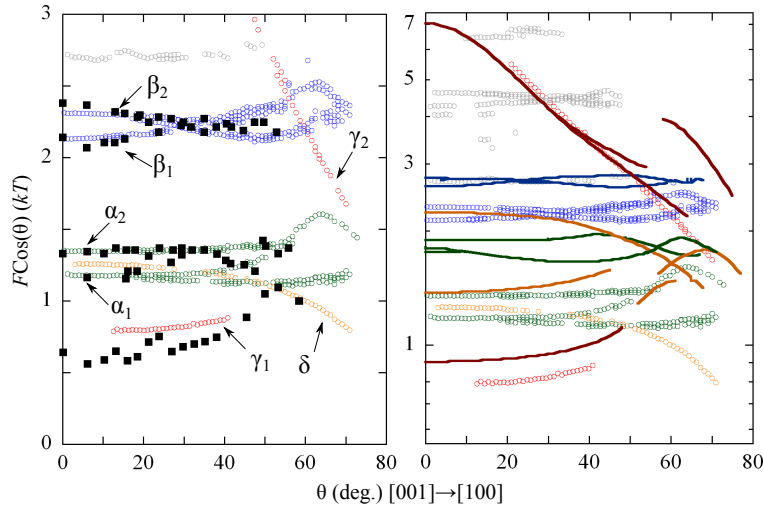


**Figure 4.3.6:** Left panel shows the measured data with points overlaid from  $\text{BaFe}_2(\text{As}_{0.37}\text{P}_{0.63})_2$  [22] with the  $\alpha$  and  $\gamma$  frequencies multiplied by 1.33 and  $\beta$  frequencies multiplied by 1.19 commensurate with known shifts from literature. Right panel shows DFT calculations (lines) overlaid on top of measured FFT data (circles). Data is colour coded according to the corresponding bands. Points in grey are harmonics.

**Table 4.2:** A summary of the Fermi surface labelling used.

Band Num.	Label	Colour	Type
1	$\delta$	Orange	hole
2	$\gamma$	Red	hole
3	$\beta$	Blue	electron
4	$\alpha$	Green	electron

in table 4.2. Minimal extrema are sub-labelled 1, maxima are sub-labelled 2. The points marked in grey are the harmonics which were identified by overlaying the measured data on itself after doubling and tripling of the frequency.

As with previous DFT calculations in the  $\text{BaFe}_2(\text{As}_{1-x}\text{P}_x)_2$  series, the calculated values are consistently higher than the measured values [20]. The exception in this case is  $\gamma_2$  which is not much different from the calculated values.

As is shown in the right panel of figure 4.3.6, the rotation plots from the DFT calculations match up qualitatively with the data but do not match up quantitatively – the calculations overestimating electron bands with respect to the size of the measured extremal orbits.

In order to obtain the correct shape of Fermi surface, the DFT calculations need to be tweaked. One technique is to apply small band-specific rigid energy shifts, which, in most cases is enough to bring the DFT in line with the experimental data. Figure 4.3.7

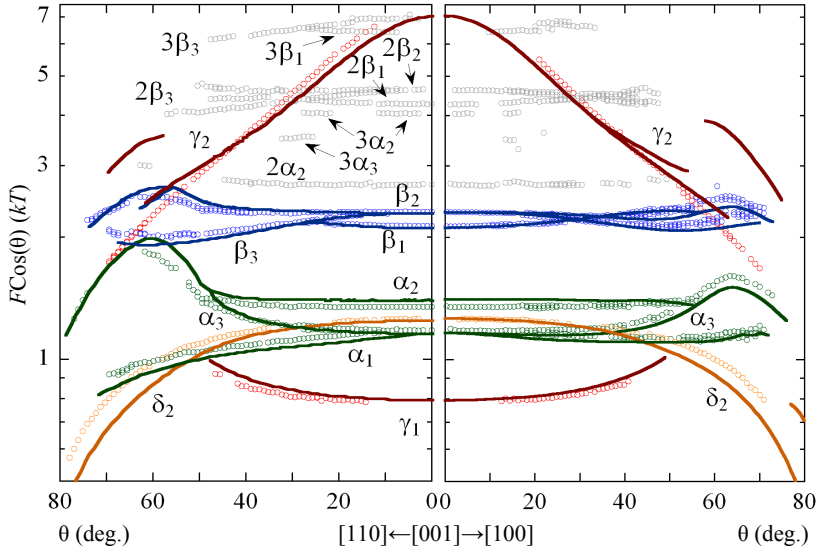


**Figure 4.3.7:** dHvA frequencies multiplied by  $\cos(\theta)$ . Solid lines are rigidly shifted DFT calculations, open circles are measured data.  $H$  field directed along [001] towards (a.) [001]  $\rightarrow$  [100] and (b.) [001]  $\rightarrow$  [110].

**Table 4.3:** Rigid energy shifts required to match the DFT calculations with the measured data.

Band	Energy Shift (Ry)
1	-0.0083
2	Wide 0.0
	Narrow -0.0038
3	0.0043
4	0.0050

shows the rotation plots which rotate towards both the [100] and [110] directions along with appropriately shifted calculations. Table 4.3 lists those energy shifts.

Band 2 in this case has two separate shifts specified in two different regions of the BZ. The rotation plot for the wider orbit located at the edge of the BZ was calculated with no energy shift and the narrow part of the Fermi surface around the  $\Gamma$  point was calculated with a shift of 0.0038 Ry. This provides a reasonable match for the rotation plot where we can apply the shift to the two regions discretely, however this proves problematic when we wish to study intermediate areas since it is not clear how the Fermi surface varies between the two regions. A technique for applying appropriate energy shifts throughout the BZ is explored in the next section.

For the [100] direction it became apparent from the fact that the DFT and the measured curves were qualitatively different that the field was not perfectly aligned with the [100]

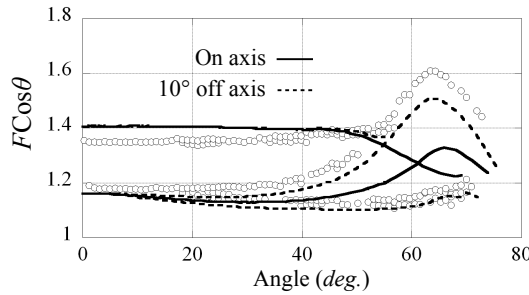


**Figure 4.3.8:** Portion of the measured FFT peaks taken towards the ‘[100]’ direction. Superimposed is angle plots calculated from DFT. Solid is calculated for the field rotating down to [100], dotted is rotated down to  $10^\circ$  off [100] in the basal plane.

axis of the sample. Figure 4.3.8 shows how the measured data (circles) does not align well with the plots calculated for rotations towards [100] (solid) but does align well with plots towards an axis which is rotated  $10^\circ$  within the *ab*-plane from the [100] direction. A  $10^\circ$  misalignment is within the estimated basal alignment error for the microscope images. The data will continue to be labelled as in the (100) plane however for convenience.

In the first place, these shifts were applied as they conveniently and effectively corrected the Fermi surface energies, however the question arises as to whether there is any physical significance to be attached to them. The technique of rigid energy corrections has been applied to previous measurements on LaFePO [8] and SrFe<sub>2</sub>P<sub>2</sub> [11] both of which are highly two dimensional systems that exhibit relatively strong nesting characteristics. This is in contrast with measurements on CaFe<sub>2</sub>P<sub>2</sub> [9] which has a highly three dimensional Fermi surface and no nesting vector. Furthermore the bulbous area of the three dimensional hole surface in BaFe<sub>2</sub>P<sub>2</sub> which does not nest requires no shifting of the Fermi surface to match DFT calculations, whereas the nested neck portion does require a shift. This correlation between nesting and shifts in calculated energy make the spin-density-wave fluctuations that are associated with the nesting phenomena an obvious candidate for the cause of the discrepancy between DFT calculation and experiment.

### Shifting the DFT calculations proportional to orbital character

The WIEN2k package can output weighted contributions to the energy values at a particular  $k$  site in the BZ broken down by orbital character. Figure 4.3.9 shows the orbital character for each of the bands along the path of Fermi surface contour in a (110) slice through the BaFe<sub>2</sub>P<sub>2</sub> BZ as a function of  $k_z$ . The top row of plots show the character broken down by atomic contribution, the middle row is broken down by the *s*, *p*, *d* and *f* contributions to the iron contribution and the bottom row breaks down the iron *d* character into its sub orbitals.

The interstitial regions account for about 20–32 % of the electron band character whilst

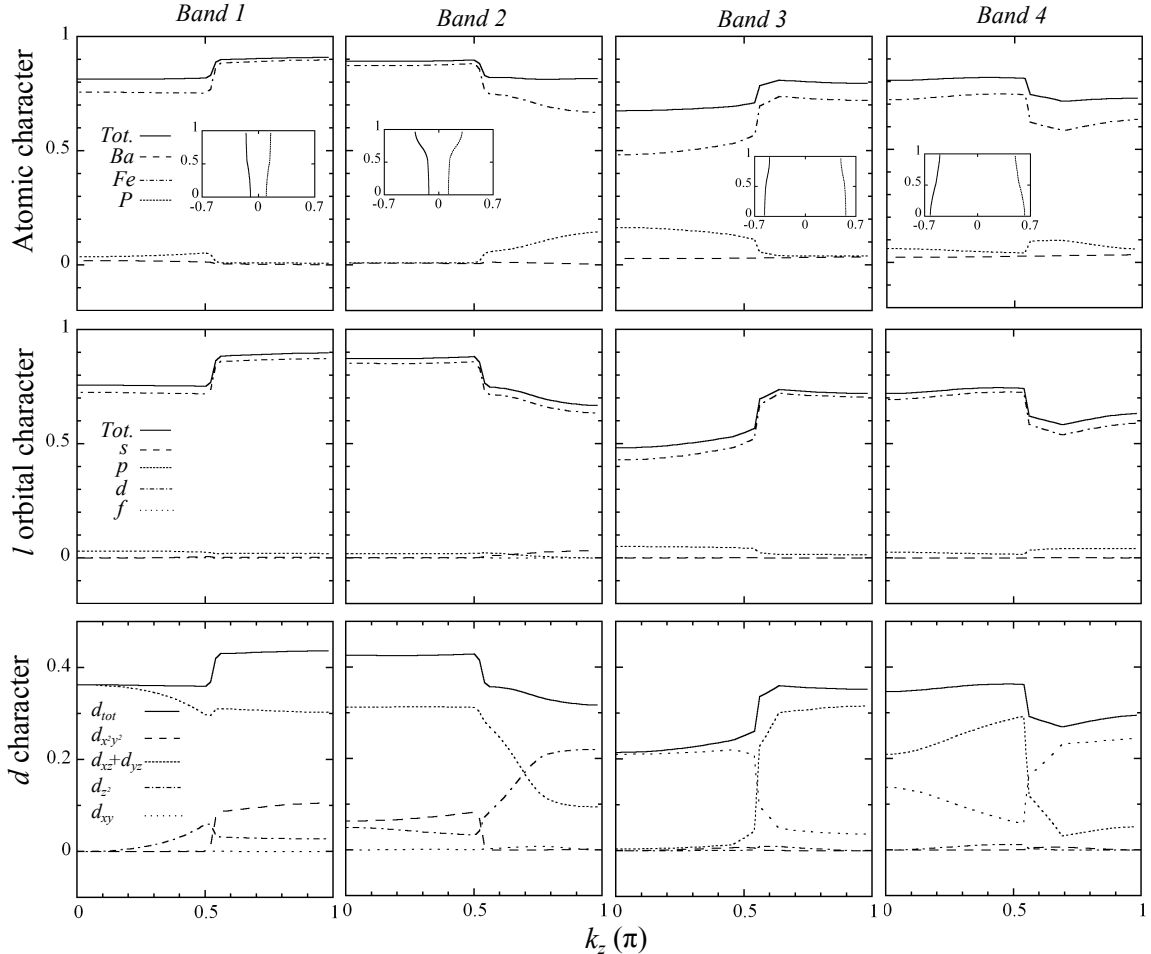


**Figure 4.3.9:** Partial orbital characters along the Fermi surface contour in the (110) slice (shown in insets) vs.  $k_z$ . Top row is the character broken down by each atom, middle row is the iron contribution broken down into the  $l$  orbital contributions, the bottom row is the iron  $d$  orbital contributions broken down into its suborbitals. The leftover region in the top row is made up of the interstitial regions outside of the muffin tin spheres which are not associated with any particular atom.

the hole bands range between 8–18 % with band 1 being more mobile around the  $\Gamma$  point whilst band 2 being higher around the  $Z$  point at the top edge of the BZ.

We can see the vast majority of Fermi surface character is due to the iron atomic contributions with some phosphor for bands 2 and 3 which corresponds well to the notion of FeP conducting planes. For all the bands, the overwhelming majority of the contribution from the iron atoms is from the  $d$  orbitals and so other contributions are ignored.

Band 2 has very little basal-plane  $d_{xy}$  and  $d_{x^2-y^2}$  character close to the Fermi level but shows a significant amount of  $d_{z^2}$  character at the wide region of the Fermi surface and  $d_{xz}+d_{yz}$  character at the narrow region. Evidently, energy shifts could be applied which are scaled to either the  $d_{z^2}$  and  $d_{xz}+d_{yz}$  orbital character in order that we obtain a smooth energy shift transition between the narrow and wide regions discussed previously.

There is a sudden jump in the data for at around the  $k_z = 0.5$  point for the hole bands and at a slightly higher  $k_z$  for the electron bands. This is due to the fact that for non-spin orbit calculations the hole (electron) bands cross at around  $k_z = 0.5$  and  $k_z = 1.5$ , however for the spin-orbit case the bands generally avoid crossing by switching the band assignment to the band that would ordinarily cross over. Hence at  $k_z = 0.5$  the band character for band 1 switches to that of band 2 (and vice-versa) and similarly between bands 3 and 4.

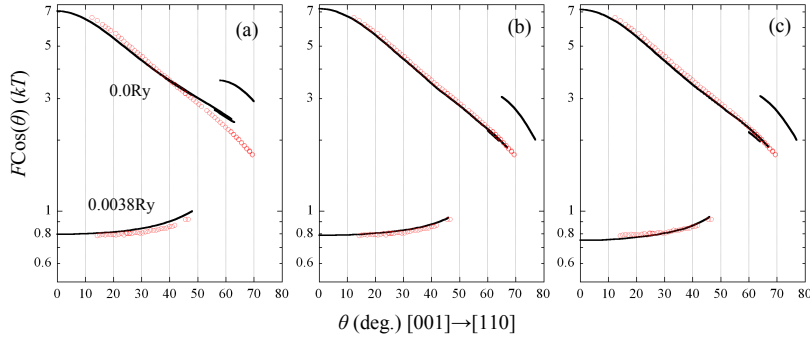
Energy shifts were applied across the full three dimensional BZ for band 2 using the following two scalings which were determined by trial and error fitting of the data,

$$d_{z^2}: \Delta\epsilon = 0.002 - 0.0052 \left[ 1 - \frac{\epsilon - 0.033}{0.2205 - 0.033} \right]$$

$$d_{xz}+d_{yz}: \Delta\epsilon = 0.002 - 0.0052 \left[ \frac{\epsilon - 0.0946}{0.3135 - 0.0946} \right]$$

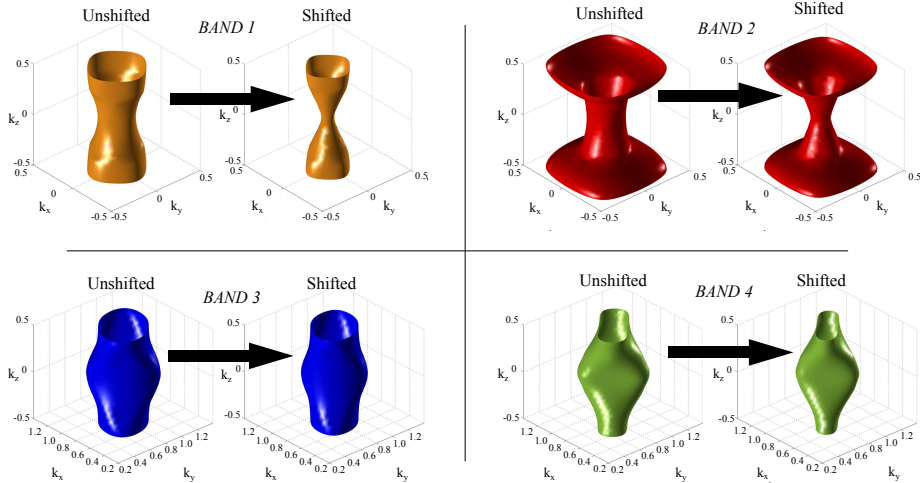
Note that these scalings ensure that the energy shift applied varies between -32 mRy and 2 mRy which are slightly different from the values applied when rigidly shifting the band. This is due to the fact that the Fermi surface area measured in the narrow region is affected more and more by the size of the Fermi surface in the wide region (and vice-versa) as the azimuthal angle gets higher. The calculated area deviates from the measured area which results in the crossing of the calculated rotation plot with the measured rotation plot shown in the first panel of figure 4.3.10. So when the rigid shifts were being determined, values were chosen which best lines up along the full length of the curve – one which will be slightly lower than if we were to match the plots exactly at  $\theta = 0^\circ$ .

The second and third panels of figure 4.3.10 show the rotation plots calculated with the energy shifts applied proportional to  $d_{z^2}$  and  $d_{xz}+d_{yz}$  orbital character respectively. We observe a much better alignment of the measured and calculated data for all angles. Figure 4.3.11 shows the Fermi surfaces before and after shifting using the rigid energy shifts for bands 1, 3 and 4 and using shifts scaled to  $d_{z^2}$  orbital character for band 2.



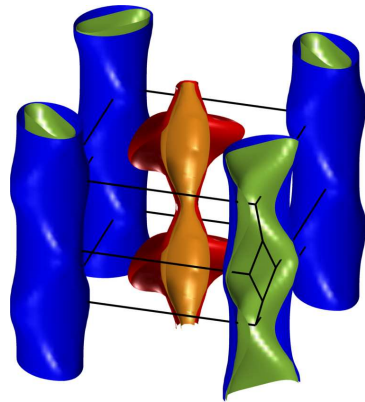
**Figure 4.3.10:** dHvA frequencies for band 2 multiplied by the cosine of the angle of the  $H$  field.  $H$  field directed along  $[001] \rightarrow [110]$ . Open circles are measured data, solid lines represent (a) rigidly shifted DFT calculations, (b) DFT calculations shifted proportional to  $d_{z^2}$  orbital character, (c) DFT calculations shifted proportional to  $d_{xz}+d_{yz}$  orbital character.

Figure 4.3.12 shows the assembled BZ for  $\text{BaFe}_2\text{P}_2$  from the corrected DFT calculations and figure 4.6.1 shows the shifted band structure for the bands that cross the Fermi level.



**Figure 4.3.11:** Comparison of Fermi surfaces according to DFT calculations both before and after shift corrections are applied. Rigid shifts are applied to bands 1, 3, 4 and shifts proportional to  $d_{z^2}$  character are applied to band 2.

The final corrections show the DFT calculations being adjusted in size only for the electron and inner hole surfaces with overall shrinking of volume, the outer hole surface is adjusted in shape as well. Volume calculations as a percentage of the BZ are given for each of the Fermi surfaces before and after shifting in table 4.4, The volumes compensate better before the shifts by a small amount ( $\sim 0.4\%$ ) with the shifts proportional to  $d_{xz}+d_{yz}$  being slightly closer to the unshifted volume.



**Figure 4.3.12:** Fully assembled Fermi surface in the first BZ of  $\text{BaFe}_2\text{P}_2$  as determined by DFT calculations corrected by either rigid energy shifts (bands 1, 3, 4) or shifts proportional to  $d_{z^2}$  character (band 2).

**Table 4.4:** Volumes of the shifted and unshifted Fermi surfaces as a percentage of BZ volume.

Band	Unshifted	Shifted $d_{z^2}$	Shifted $d_{xz}+d_{yz}$
1	5.54%	2.28%	2.28%
2	10.37%	9.74%	9.64%
3	(-)9.58%	(-)7.89%	(-)7.89%
4	(-)6.39%	(-)4.49%	(-)4.49%
Total	-0.065%	-0.352%	-0.450%

#### 4.4 Interpolating the $\text{BaFe}_2(\text{As}_{1-x}\text{P}_x)_2$ series Fermiology

Although dHvA measurements were taken by the author on other members of the  $\text{BaFe}_2(\text{As}_{1-x}\text{P}_x)_2$  series as mentioned at the start of this chapter, clear oscillations were not consistently found for all the electron pockets and no oscillations were found for the hole pockets as was the original aim. For this reason we refer to previous results which have shown convincing measurement of both the hole and electron pockets.

We can use existing literature measurements of the Fermi surface at  $x = 0.38$  from Yoshida *et al.* [24],  $x = 0.63$  from Analytis *et al.* [22] and a range between  $0.4 < x < 1.0$  from Shishido *et al.* [20] to obtain an approximate relation for the size of Fermi surface orbits across the  $\text{BaFe}_2(\text{As}_{1-x}\text{P}_x)_2$  series. Figure 4.4.1 shows the maximum and minimum orbit sizes with the field along the  $c$ -axis from these papers along with data presented in this thesis. It may be possible to apply a linear scaling to determine the intermediate

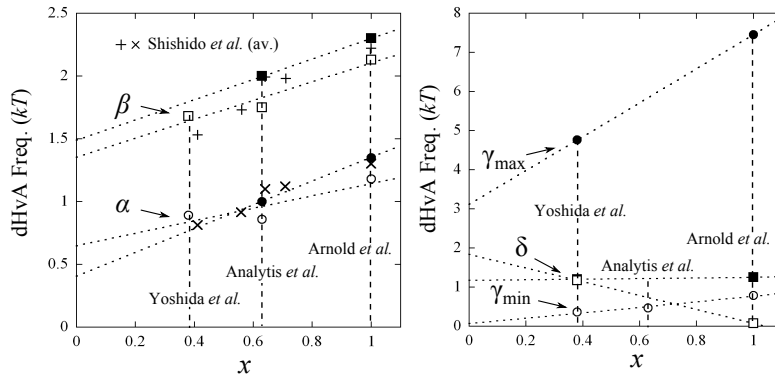


**Figure 4.4.1:** Left panel shows the trend in electron orbit size at  $\theta = 0^\circ$  over the series, right panel show the hole orbit size trends. Dotted lines show linear fits to the data.

orbit sizes however there are a number of assumptions that need to be made.

Firstly we cannot apply Vegard's law beyond a structural transition in the series meaning we cannot extrapolate to the orthorhombic antiferromagnetic state at the low  $x$  end of the phase diagram. The ARPES measurement by Yoshida *et al.* at  $x = 0.38$  roughly coincides with the edge of the orthorhombic transition as shown in figure 1.1.5 but was found to be tetragonal and so we can use to define the lower limit for the extrapolation at low temperatures.

There is also the problem of the third hole surface around the  $\Gamma$  point which appears in DFT calculations. Although it has not been observed in any of the measurements and we might expect smaller orbits to have a stronger signal\*, the hole pockets in these materials have strong  $k_z$  dispersions meaning the  $A_{\text{warp}}$  factor damps the signal. Also it may be

\*Smaller orbits complete a greater number of orbits for a given mean free path as explained in section 2.3.3.

**Table 4.5:** Linear relations to determine orbit sizes. Coefficients are of the form  $F = mx + c$ .

Orbit	$m$	$c$
$\delta_{\max}$	0.081	1.169
$\delta_{\min}$	-1.766	1.841
$\gamma_{\max}$	4.339	3.111
$\gamma_{\min}$	0.698	0.071
$\beta_{\min}$	0.749	1.352
$\beta_{\max}$	0.811	1.489
$\alpha_{\max}$	0.495	0.646
$\alpha_{\min}$	0.946	0.404

close in size and shape to other hole surfaces making it difficult to pick out with current ARPES resolution.

It also should be noted that a linear extrapolation of  $\delta$  suggests that it will become more three dimensional as it goes below  $x = 0.38$ , however this does not appear to be supported by the DFT results which show it remaining quasi-two dimensional.

With the above (many) caveats in mind, we can determine a series of linear laws which would approximately determine the orbit sizes for  $0.38 < x < 1.0$  by applying fits to the data in figure 4.4.1. The results of these fits are given in table 4.5.

## 4.5 Harmonic parametrisation of the Fermi surface

An analytic form for the Fermi surface can be obtained using a harmonic expansion of sin and cosine functions as described by Bergemann *et al.* [112]. Primarily this was done so as to provide a convenient way to reconstruct the Fermi surface without necessitating DFT calculations for future use in models. The expansion is as described as,

$$k_F(\phi, \kappa) = \sum_{\substack{\mu, \nu \geq 0 \\ \mu \text{ even}}} k_{\mu\nu} \cos \nu \kappa \begin{cases} \cos \mu \phi & (\mu \bmod 4 = 0) \\ \sin \mu \phi & (\mu \bmod 4 = 2) \end{cases} \quad (4.5.1)$$

where  $k_F$  is the Fermi surface in k-space,  $\kappa = ck_z/2$ ,  $c$  is the unit cell height and  $\phi$  is the polar angle. A slightly different set of functions would be necessary to fit the electron Fermi surface in the adjacent corners due to the screw symmetry, however only one electron sheet was fitted.

The two dimensional fits were performed using a least square fitting routine using MATLAB on the DFT data shifted as described in the previous section. The number of terms for the fits were increased until the residuals ceased to change appreciably. Fit parameters are presented in table 4.6. Due to the skewed nature of the  $k_z$  dispersion of

the outer hole surface 20 terms were necessary to obtain a reasonable fit to the corrected DFT data however electron surfaces could be fitted well with 9 terms and the inner hole surface with 10 terms. The final analytical function was then used to create an ‘energy dispersion’ on a discrete grid of  $k$ -points such that plotting an isosurface at  $\epsilon = 0$  Ry correctly recreated the Fermi surface\*. Using this dispersion in the existing MATLAB code, extremal orbits were then calculated as a check of how well it matches the original data. The results of this are presented in figure 4.5.1. As you can see, although the fits were to the modified DFT calculations, the fits are also reasonably accurate at modelling the measured data.

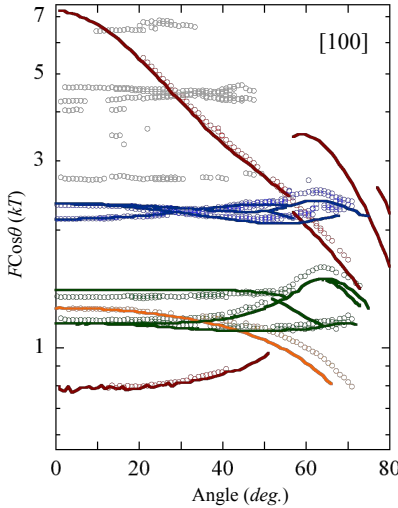


**Figure 4.5.1:** Rotation plots for the harmonic fits calculated from the c-axis down towards [100].

## 4.6 Susceptibility calculations

To verify that we do get enhanced susceptibility, which may lead to a spin-density wave state, the  $q$ -dependent susceptibility – described in section 2.4.1 – was calculated using code developed by the author and listed in appendix B. Since the Lindhard function takes the sum over all energies in the BZ, there may be some concern that the rather crude adjustments to the DFT calculations performed in the previous section – which have only been verified to be correct for energies at the Fermi surface – may give erroneous results. However the nature of the Lindhard function means that far greater weight is given to energies that are near the Fermi surface. Figure 4.6.1 shows the ‘spaghetti plot’ with the energies tweaked as described in the previous section. We see that there are discontinuities

---

\*The resulting dispersion was not physical and simply served as a computational structure to pass the shape of the Fermi surface to the MATLAB code, energy values at  $k$ -point away from the Fermi surface are somewhat arbitrary.

**Table 4.6:** Harmonic expansion fit parameters performed on the shifted DFT Fermi surfaces.

Factor	$\alpha$	$\beta$	$\gamma$	$\delta$
$k_{00}$	1.90796e <sup>-1</sup>	2.59538e <sup>-1</sup>	2.58282e <sup>-1</sup>	1.35031e <sup>-1</sup>
$k_{02}$	-1.32049e <sup>-2</sup>	-1.01956e <sup>-3</sup>	0	0
$k_{04}$	9.24279e <sup>-4</sup>	4.28603e <sup>-4</sup>	-1.01085e <sup>-2</sup>	1.95065e <sup>-3</sup>
$k_{20}$	4.30196e <sup>-4</sup>	-1.51226e <sup>-4</sup>	-1.46090e <sup>-1</sup>	-6.75502e <sup>-2</sup>
$k_{22}$	3.23365e <sup>-4</sup>	1.91896e <sup>-4</sup>	0	0
$k_{24}$	-9.30815e <sup>-2</sup>	-4.23320e <sup>-2</sup>	1.13859e <sup>-2</sup>	-5.31077e <sup>-3</sup>
$k_{40}$	-1.64499e <sup>-2</sup>	5.02893e <sup>-3</sup>	6.15148e <sup>-2</sup>	-5.70262e <sup>-3</sup>
$k_{42}$	-1.49159e <sup>-2</sup>	-7.07858e <sup>-3</sup>	0	0
$k_{44}$	-6.14076e <sup>-4</sup>	-2.86767e <sup>-4</sup>	-9.49526e <sup>-3</sup>	5.28982e <sup>-3</sup>
$k_{60}$	0	0	-1.85170e <sup>-2</sup>	-1.22242e <sup>-3</sup>
$k_{64}$	0	0	-9.04247e <sup>-4</sup>	-2.82851e <sup>-4</sup>
$k_{80}$	0	0	-6.79607e <sup>-3</sup>	-2.22767e <sup>-3</sup>
$k_{84}$	0	0	1.61746e <sup>-3</sup>	-1.90500e <sup>-3</sup>
$k_{100}$	0	0	1.07007e <sup>-2</sup>	0
$k_{104}$	0	0	7.97948e <sup>-4</sup>	0
$k_{120}$	0	0	-3.89161e <sup>-3</sup>	0
$k_{124}$	0	0	-1.57292e <sup>-3</sup>	0
$k_{140}$	0	0	-1.81052e <sup>-3</sup>	0
$k_{144}$	0	0	3.81207e <sup>-4</sup>	0
$k_{160}$	0	0	3.04268e <sup>-3</sup>	0
$k_{164}$	0	0	1.14420e <sup>-3</sup>	0
$k_{180}$	0	0	-1.07753e <sup>-3</sup>	0
$k_{184}$	0	0	-4.92181e <sup>-4</sup>	0

in band 2, most notably between  $Z$  and  $\Sigma_1$ , due to the correction applied proportional to the  $d_{z^2}$  character, however these are reasonably far from the Fermi level and so should not affect the calculations significantly.

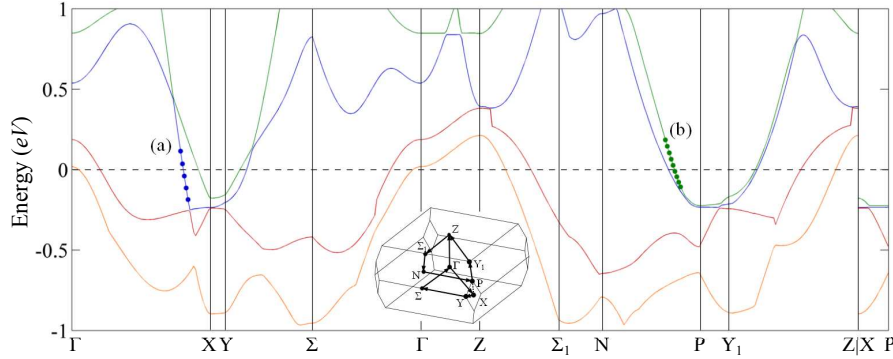


**Figure 4.6.1:** Band structure for the bands that cross the Fermi surface shifted to fit the dHvA data. (a) and (b) give an idea of the  $k$ -point mesh density of the WIEN2k calculation at the Fermi surface. Inset shows the path around the BZ.

Calculations were performed using the `calc_x0.m` code described in section 3.2 using a  $93 \times 93 \times 93$  grid of energy values that covered the first BZ. We will need to smooth over the granularity of the WIEN2k band model since for the imaginary part at least, the calculation is very sensitive to slight imperfections in cancellation near the Fermi energy. Referring to figure 4.6.1, there are two regions in the marked (a) and (b) which show points around the Fermi level as they are spaced in the  $93 \times 93 \times 93$  model. (a) is particularly steep and has  $\Delta\epsilon/\Delta\text{pt.} = 0.0760$  eV and (b) is more typical of the gradient at the Fermi level and has  $\Delta\epsilon/\Delta\text{pt.} = 0.0368$  eV. So the energy scale that will need to compensated is  $\sim 2.5 \times 10^{-3}$  Ry.

Susceptibility was calculated for a wide range of magnitudes of  $\delta$  and  $\omega$  in order to gauge qualitative behaviour with the resulting plots shown in figure 4.6.2. Both the real and imaginary parts undergo qualitative changes as the parameters are adjusted above the spacing corresponding to the typical gap in energy between points. The imaginary part also undergoes a qualitative change when  $\omega$  falls below  $1 \times 10^{-5}$  Ry and there is also an increase in noise when  $\delta$  falls below a similar energy threshold. We continue using  $\delta = 1 \times 10^{-3}$  and  $\omega = 1 \times 10^{-3}$  which correspond approximately the energy scale of the spacing as well as the energy scale of the temperature smearing.

The upper panel of figure 4.6.3 shows the quantified plots for the real and imaginary parts of the susceptibility at the chosen values of  $\delta$  and  $\omega$ . The contour plots in the insets show the two-fold symmetry due to the choice of  $k_z = \pi$ . Unlike LaFeAsOF where the two dimensional approximation is a good one, this is not necessarily the case for  $\text{BaFe}_2\text{P}_2$  which features a strongly three-dimensional hole band and some warping of the electron bands. The lower panels present the same calculation performed at  $k_z = 0$  which shows

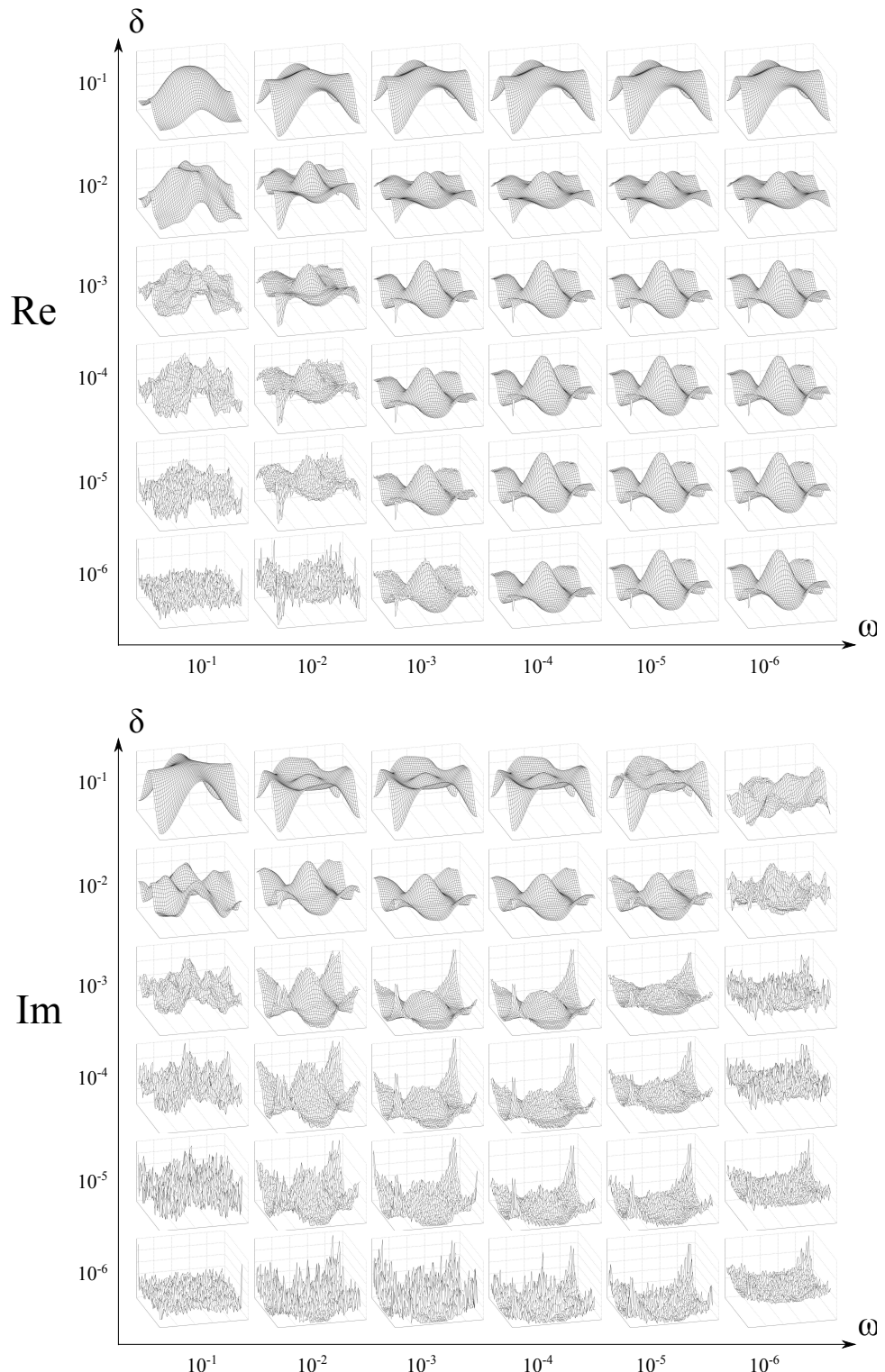


**Figure 4.6.2:** Qualitative plots of the real and imaginary part of the Lindhard susceptibility calculated at  $k_z = \pi$  for  $T = 157$  K and a range of  $\delta$  and  $\omega$  values.

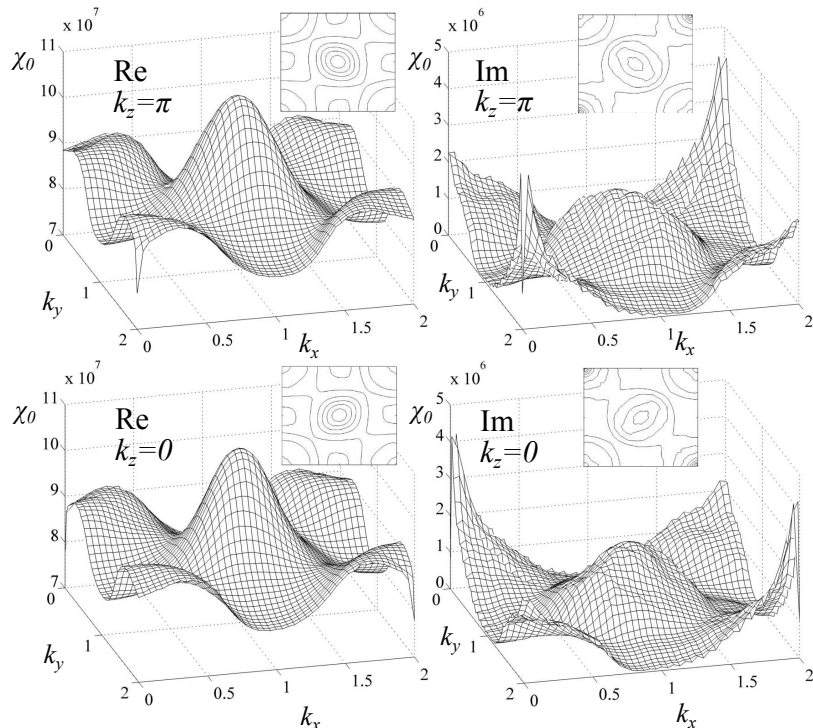


**Figure 4.6.3:** Real and imaginary part of the Lindhard susceptibility are plotted on the left and right respectively. Upper panels are at  $k_z = \pi$  and lower are at  $k_z = 0$ . For these calculations  $\delta = 1 \times 10^{-3}$ ,  $\omega = 1 \times 10^{-3}$  and  $T = 157.88$  K. Insets show contour plots for the respective surface plots.

little change other than a rotation of the susceptibility bias due to the screw symmetry of the electron bands.

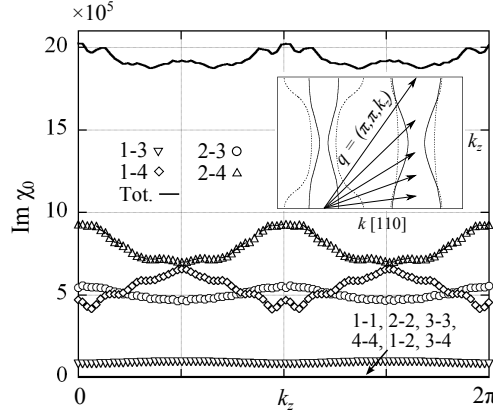


**Figure 4.6.4:** Left panel shows the imaginary part of the Lindhard susceptibility between bands summed with their reciprocals for  $q = (\pi, \pi, k_z)$  over the height of the BZ. We see enhancements at  $k_z = \pi/2, 3\pi/2$  for bands 1-4 and 2-3 and at  $k_z = 0, \pi, 2\pi$  for bands 2-3 and 2-4.

To verify that there is indeed a nesting conditions at some  $k_z$  for  $q = (\pi, \pi, k_z)$  figure 4.6.4 presents the imaginary part of the susceptibility vs.  $k_z$  for a range of nesting vectors. Each coupling of bands is summed both ways — e.g. 4-1 is summed with 1-4 — and plotted in order to obtain the residual difference due to  $\omega$ . Unsurprisingly, we see that self coupling results in very little weight with hole-hole and electron-electron coupling also resulting in little weight. The strongest component is due to bands 2-4 which also demonstrates a strong enhancement of around 25% at  $k_z = 0, \pi, 2\pi$ . Band 2 also couples strongly with band three at the same  $q$  vectors with around a 17% enhancement. Band 1 couples strongly with band 4 but at  $k_z = \pi/2, 3\pi/2$  with the largest enhancement of around 38%. Band 1 also couples less strongly with band 3 at the same  $k_z$  with an enhancement of around 15%. The total susceptibility is determined mostly by the coupling of band 2 but only has a relatively moderate enhancement of around 7.4% at  $k_z = 0, \pi, 2\pi$ .

Figure 4.6.5 shows cross sections of the final corrected Fermi surfaces showing the basal-plane at the bottom of the BZ ( $k_z = 0$ ), quarter of the way up, ( $k_z = 0.25$ ) and halfway up ( $k_z = 0.5$ ). The inner hole surface (band 1) at  $k_z = 0.5$  directly matches the size and shape of the inner electron surface (band 4) at  $k_z = 0.25$  which is the likely cause of the strong enhancement observed in the susceptibility. Moreover, the bands share similar predominant  $d_{xz} + d_{yz}$  orbital character. The strong enhancements between bands 2 and 4 are also shown in the figure as a dashed arrow.

These enhancements at  $q = (\pi, \pi)$  show that partial nesting does indeed occur in this material demonstrating that this condition alone is not sufficient for superconductivity to occur. This concludes the Fermiology results, we now move onto the mass enhancements.

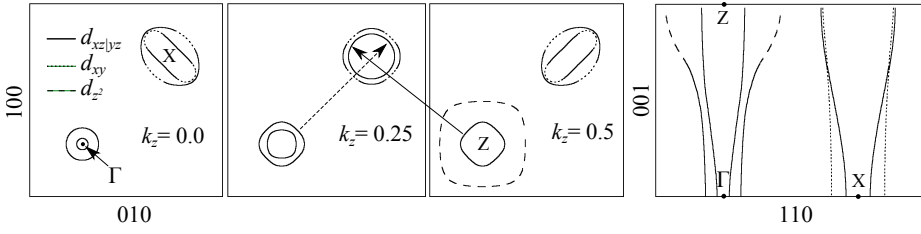


**Figure 4.6.5:** Cross sections of the corrected Fermi surface in the *ab* plane (panels 1, 2 and 3) and in the [110] plane (panel 4). Markings correspond to the orbital character of the Fermi surface slices. Two nesting vectors are shown as long arrows.

## 4.7 Determining the spin effective mass

Following the method in section 3.1.3, only a couple of portions of the data are suitable for analysis in that they feature more than one identifiable zero in the oscillations due to the spin term which are suitably strong and well separated from other data. These are a maximal area of the  $\alpha$  curve in the [100] direction and a maximal area of the  $\beta$  curve in the [110] direction.

We begin by looking at the  $\beta$  data by using the cylindrical approximation and then move onto using an expression for  $m_b^*$  derived from a polynomial fit to band masses calculated from DFT. Figure 4.7.1 shows the two fit forms for the band mass used — an eighth order polynomial and the cylindrical approximation — used as well as in the inset the particular portion of the  $\alpha$  band data that was used in the following investigation. As we can see from the inset, we use a relatively small portion of the measured data curve. Detailed in the panels to the right of the figure are the parameters for the two equation forms for the band mass. Beginning with the cylindrical approximation, figure 4.7.2 shows

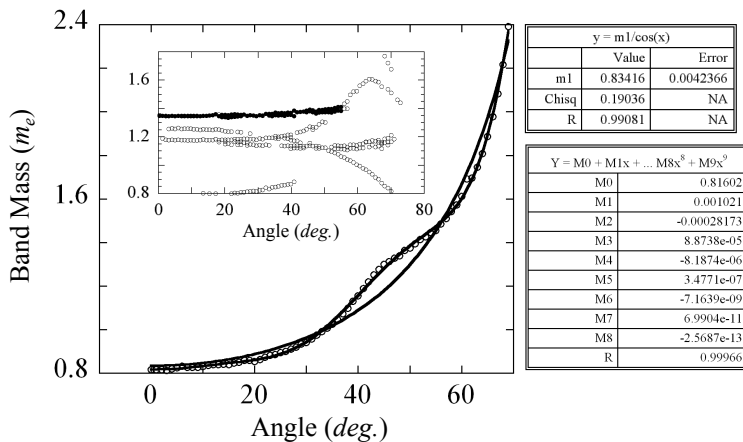


**Figure 4.7.1:** Band masses calculated from DFT of band 4 taken over a range of angles rotating towards the [100] direction. A fit to an order 8 polynomial is shown as well as a comparative fit using the cylindrical approximation.

the FFT amplitudes for the said portion of the  $\alpha$  electron pocket over a range of angles towards the [100] direction as open circles. The shaded areas delimit where we believe the amplitudes go to zero as determined by inspecting the overall shape of the curve and the splitting of the peaks. The upper panel shows the  $n = 5$  oscillation, with dotted lines showing the bounds using the cylindrical approximation for the band mass. The  $n = 5$  oscillation most closely matches the zeros in the data with the  $n = 6$  oscillation which fits reasonably well presented in the middle panel. The lower panel shows the next ( $n = 7$ ) and previous oscillations ( $n = 4$ ) in order to demonstrate that the  $A_S$  curves (given by eqn. 2.3.17), no longer align well with the data. We note that for negative angles (i.e. where the sample was rotated back beyond  $B \parallel [001]$ ) the amplitude is not symmetric as expected. This has been observed previously for measurement using a similar technique [77] and the cause has not yet been fully determined. Some possible explanations could be changes in the resistance response of the cantilever as are transitions from flexing upwards to flexing downwards however further investigation will be required to determine this. Taking  $g = 2$ , the spin masses obtained using the cylindrical approximation from the presented curves are  $5.01 \pm 0.05 m_b^*$  for  $n = 5$  and  $6.07 \pm 0.06 m_b^*$  for  $n = 6$ . We now contrast this with a spin mass determination using a band mass calculated from DFT. Figure 4.7.3 shows the revised curves with the upper panel showing  $n = 4$  to be the best fitting with the lower panel demonstrating  $n = 3, 5$  do not fit well to the measured data. Now the fit values gives a spin mass of  $4.02 \pm 0.06 m_b^*$ . The second suitable portion of data analysed is that of the maximal extrema of  $\beta$  where the field is rotated towards the [110] direction. The DFT calculations do not follow exactly the shape of the measured data and leads to a discontinuous jump in the band mass if we strictly follow the maximal orbits — for this reason we elect to only use the cylindrical approximation since the portion shown appear relatively two-dimensional. Figure 4.7.4 shows the reasonable fits for  $n = 4$  and  $n = 5$  with the lowest panel showing the oscillations  $n = 3$  and  $n = 6$  are clearly not aligned with the measured data. The oscillations  $n = 4$  and  $n = 5$  correspond to spin masses of  $3.46 \pm 0.02 m_b^*$  and  $4.44 \pm 0.03 m_b^*$  respectively.

## 4.8 Determining the thermal effective mass

### Basic LK formula fitting

A series of field sweeps were taken with  $H$  at  $12^\circ$ ,  $28^\circ$  and  $46^\circ$  from [001] in the [110] direction. These were performed at a variety of temperatures from base ( $\approx 0.3$  K) to above 2 K. Corrections were applied as detailed in section 3.1.2. Figure 4.8.1 shows the Fourier amplitude of various peaks as a function of temperature along with fits to equation 2.3.13. The field range for the FFT was necessarily large enough that individual peaks did not overlap and also could be observed across a reasonable range of temperatures but also

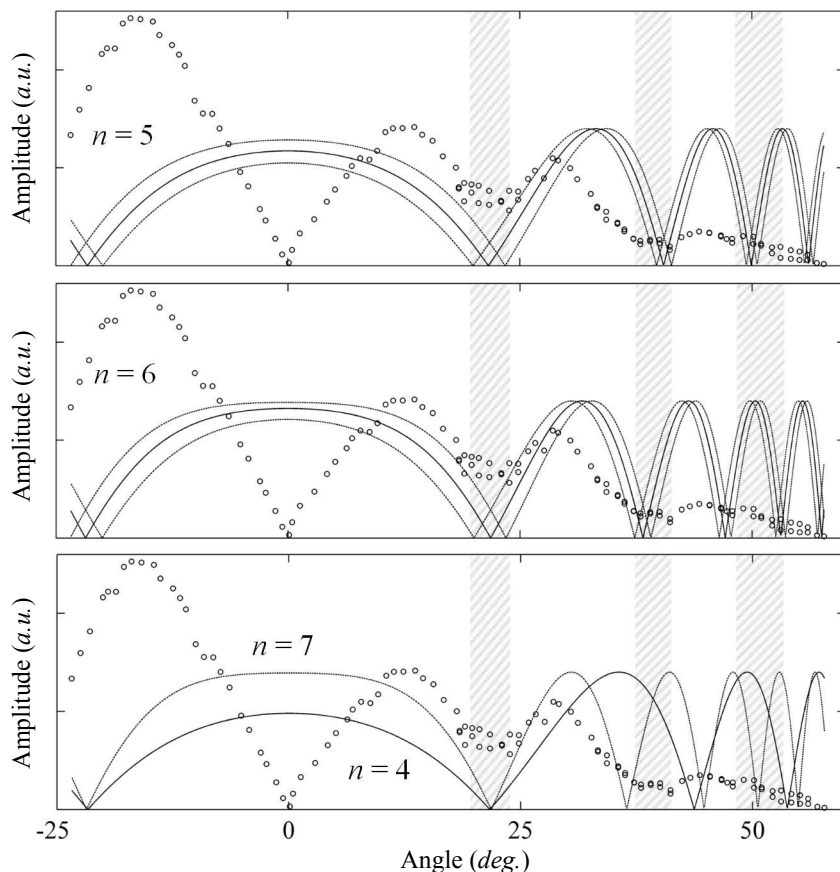


**Figure 4.7.2:**  $A_S$  curves calculated for various oscillations using the cylindrical approximation. Open circles are FFT amplitudes for  $\alpha$  band rotating towards the [100] direction.

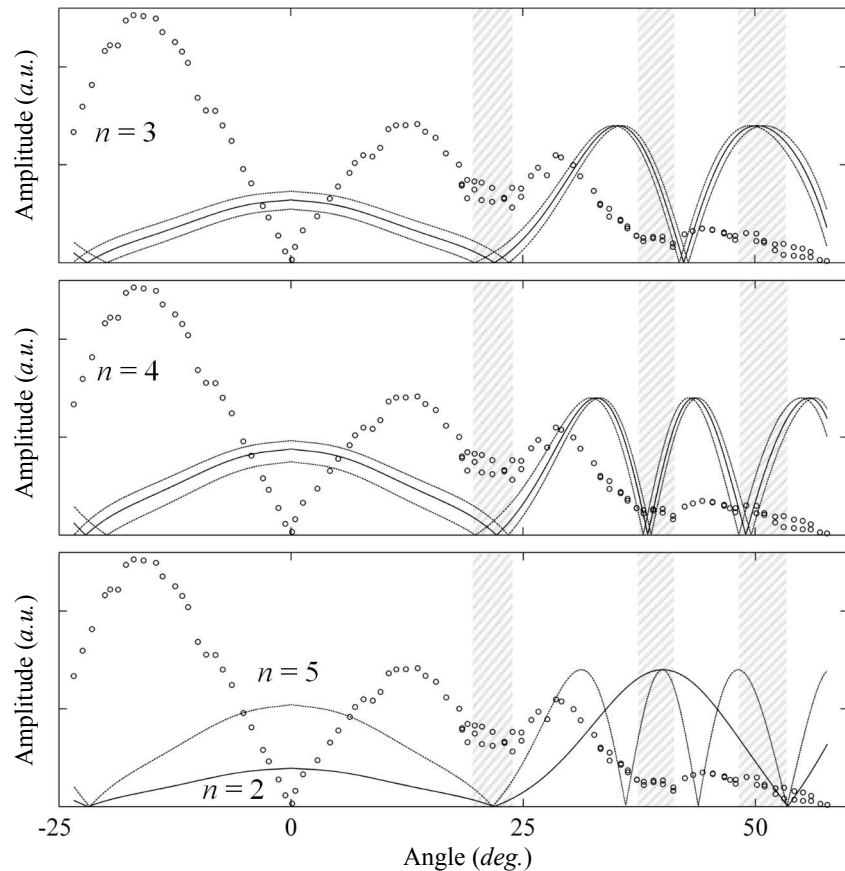


**Figure 4.7.3:**  $A_S$  curves calculated for various oscillations using the polynomial fit to DFT calculated band masses. Open circles are FFT amplitudes for  $\alpha$  band rotating towards the [100] direction.

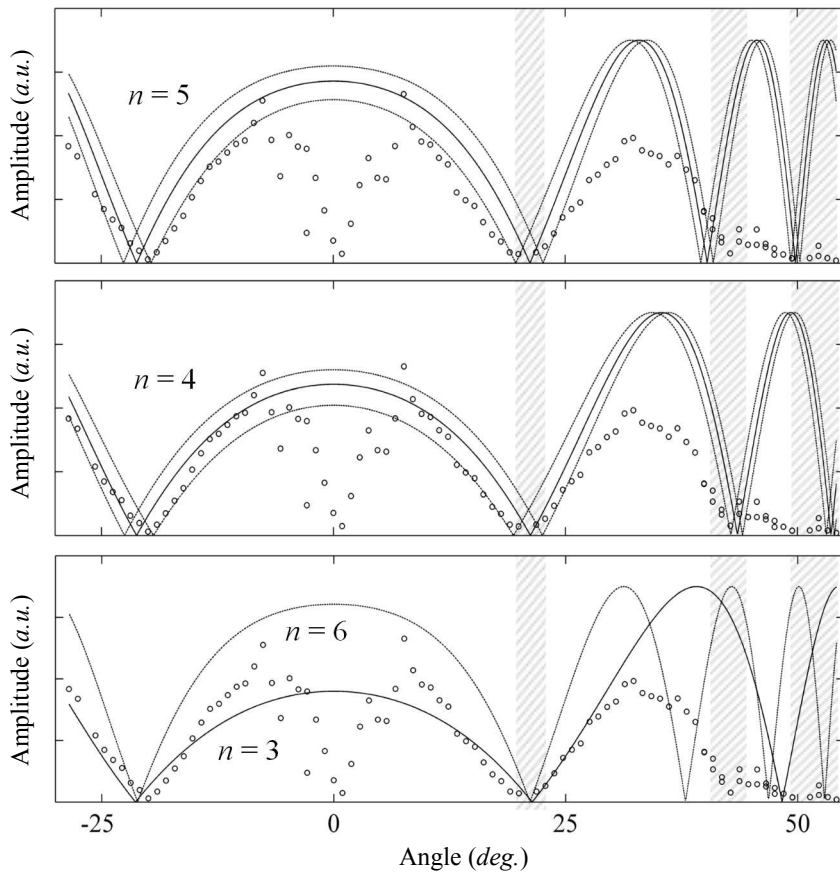


**Figure 4.7.4:**  $A_S$  curves calculated for various oscillations using the cylindrical approximation. Open circles are FFT amplitudes for  $\beta$  band rotating towards the [110] direction.

small enough so that the  $B$  dependent Dingle factor did not play too large a role and so an average  $B$  field can be assumed. The results from these fits are shown in table 4.7 along with the fit ranges. All FFTs in the plot were taken over an interval of 12-18 T with the exception of the  $\gamma_2$  fit which was taken between 16-18 T so as to attain an appreciable peak. The standard deviation was calculated by randomly varying the temperature values by the estimated error (0.06 T) 1000 times and then taking the standard deviation of the fitted  $m^*$  values. Table 4.7 also shows gives a result, marked with a dagger, taken with a

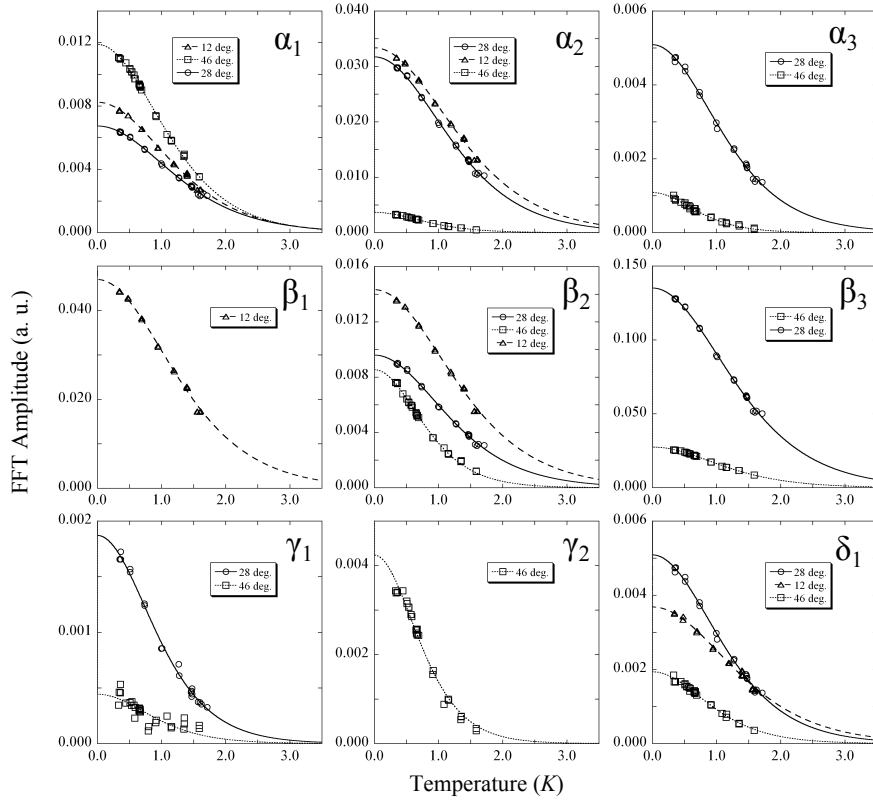


**Figure 4.8.1:** Fits to the temperature dependent term of the LK formula,  $A_T$ .

different field range. These fits give quite different values for the effective mass, indicating that the average field approximation is not a valid one.

### Retrofitting ansatz LK formulae

The measurements presented in the previous section were further refined using the ansatz LK formulae as described in section 3.1.4. Figure 4.8.2 shows some sample fits used to extract the Dingle terms used in the ansatz fit functions. Table 4.7 lists the extracted Dingle terms for each peak of the Fermi surface and the subsequent results of the retrofitted calculations for the effective masses. The various field limits were chosen in order to either obtain a clearly delimited peak in the lower field cases or to obtain a signal from a weak

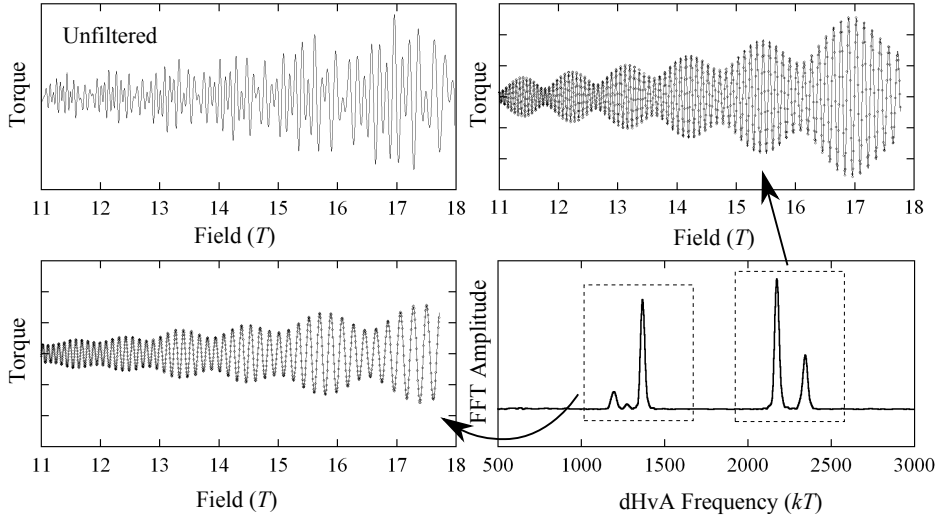


**Figure 4.8.2:** Top left panel shows torque data for data taken at 12° towards the [110] direction at 0.35 T with a polynomial background subtracted. Bottom right shows the FFT and the two filter windows to produce the filtered torque plots in the top right and bottom left. Filtered plots are fitted to extract the Dingle term for each frequency.

peak in the higher field cases.

### 'Microfitting' the LK formula

A second attempt at refining the LK fits was performed by applying the microfit technique described in section 3.1.4 with 1.5 sinusoidal oscillations fit at a time. Filtering the data beforehand is not always straightforward due to close proximity of neighbouring peaks. The stronger peaks from the  $\alpha$  and  $\beta$  Fermi surfaces show banding of the masses and a clear trending of the results to one of a few values which have been highlighted in yellow. Data in these regions were averaged to give the values in table 4.7.

All filtered using function  $F_{\text{filt}}(x) = F(x) \times 1/2[\tanh(\pi(x - x_{\text{low}})/w) + \tanh(-\pi(x - x_{\text{high}})/w)]$  where  $F$  is the Fourier transform of the torque data,  $x$  is the dHvA frequency,  $x_{\text{low}}$  and  $x_{\text{high}}$  are the lower and upper limits of the filter range respectively and  $w$  determines the trail off slope of the filter function. For all measurements  $w = 10$ .

## 4.9 Conclusions

The BaFe<sub>2</sub>P<sub>2</sub> crystal and the subsequent angle dependent dHvA measurements are of very good quality as evidenced by a number of traits including the presence of second and third harmonics in the FFTs, the hole orbits showing up over a wide angular range, the early onset of oscillations at 6 T and the observation of the Zeeman splitting of the FFT peaks. The crystal appears to be a very clean single crystal although there is some evidence of some misaligned domains, for example from some of the Bragg spots doubling

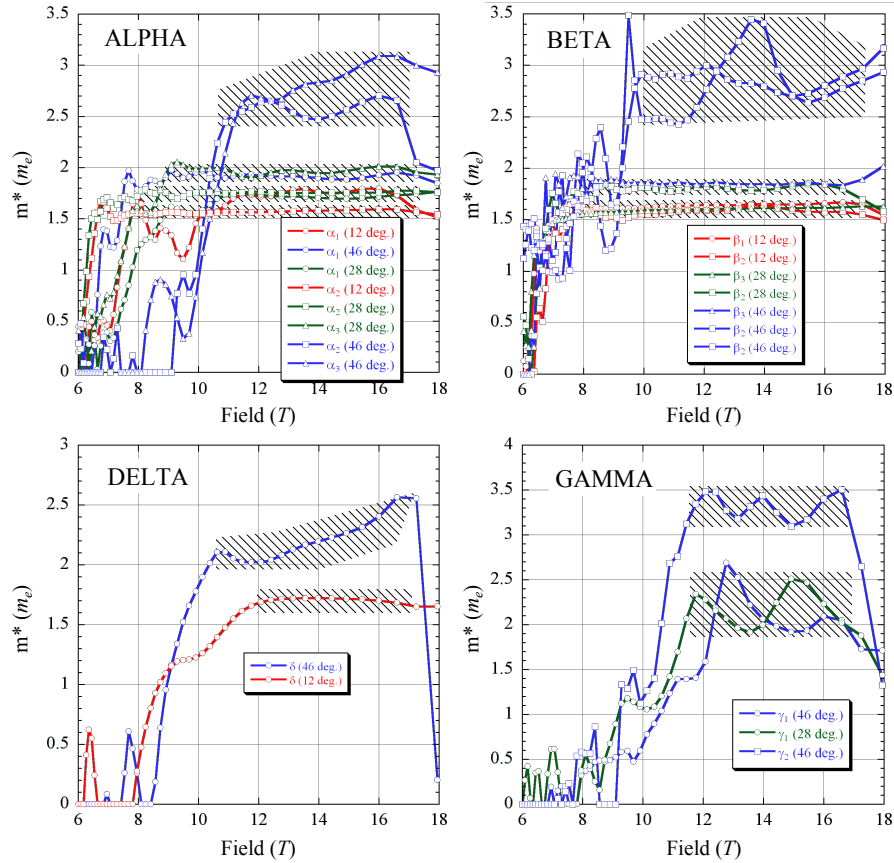


**Figure 4.8.3:** Effective temperature dependent masses extracted from sine wave fits to between one and three dHvA oscillations in the measured data. See Appendix A for a full list of parameters for each set of fits.

**Table 4.7:** Comparison of the three effective mass calculation techniques. First grey band shows the plain LK fitted results, following white band details the retrofitted effective mass calculations, following grey band details the microfitted results, and the final band details the band masses from DFT calculations and the three results normalised to these band masses. Result marked with a dagger is repeated with a different field range. Entries marked 'NA' had a signal too weak to extract an  $\alpha$  value and so microfitting was not possible.

Angle	Freq.	Label	$m_{\text{LK}}^*$	$m_{\text{ret.}}^*$	$\alpha$	$B_{\min.}$	$m_{\text{mic.}}^*$	$B_{\max.}$	$B_{\min.}$	Filt.	Width	$m_{\text{b}}^*$	$\frac{m_{\text{LK}}^*}{m_{\text{b}}^*}$	$\frac{m_{\text{ret.}}^*}{m_{\text{b}}^*}$	$\frac{m_{\text{mic.}}^*}{m_{\text{b}}^*}$
12	1210	$\alpha_1$	1.49(2) <sup>†</sup>	1.69	58.68	8	NA	NA	NA	NA	NA	1.04	1.43	1.63	NA
12	1210	$\alpha_1$	1.71(3)	1.75	58.68	12	1.75(3)	17.0	11.0	1100–1240	1.04	1.64	1.68	1.68	
28	1269	$\alpha_1$	1.64(2)	1.68	59.60	12	1.72(2)	17.0	11.0	1200–1310	0.90	1.83	1.88	1.92	
46	1532	$\alpha_1$	1.86(3)	1.90	48.79	12	1.92(2)	17.0	9.0	1430–1585	1.00	1.86	1.90	1.92	
12	1372	$\alpha_2$	1.54(2)	1.58	45.99	12	1.57(1)	17.0	8.0	1320–1440	0.84	1.83	1.88	1.86	
28	1530	$\alpha_2$	1.69(2)	1.74	72.35	12	1.75(2)	17.0	8.0	1450–1650	0.93	1.81	1.87	1.88	
46	2017	$\alpha_2$	2.49(5)	2.56	61.06	12	2.55(11)	16.8	10.5	1970–2100	1.83	1.36	1.40	1.40	
28	1365	$\alpha_3$	1.85(3)	1.93	115.49	12	1.97(3)	17.0	9.5	1320–1440	1.18	1.56	1.63	1.67	
46	1930	$\alpha_3$	2.87(7)	3.04	149.39	12	2.75(24)	17.0	10.7	1890–1970	1.00	2.87	3.04	2.75	
12	2180	$\beta_1$	1.61(2)	1.65	51.12	12	1.63(2)	17.0	8.0	2100–2270	0.98	1.64	1.68	1.66	
12	2350	$\beta_2$	1.56(3)	1.62	102.36	12	1.57(3)	17.0	9.0	2270–2450	0.86	1.81	1.88	1.82	
28	2605	$\beta_2$	1.30(2)	1.87	102.36	6	1.81(2)	17.0	8.5	2555–2670	1.03	1.68	1.71	1.76	
46	3347	$\beta_2$	1.73(2)	1.76	34.08	12	2.86(8)	17.3	10.0	3250–3370	1.80	1.44	1.50	1.59	
46	3381	$\beta_2$	2.59(6)	2.69	94.57	12	2.78(32)	17.3	10.0	3365–2500	1.80	0.88	0.90	1.55	
28	2475	$\beta_3$	1.58(2)	1.61	48.81	12	1.59(2)	17.0	8.0	2400–2560	0.93	1.95	2.00	1.71	
46	2970	$\beta_3$	1.82(3)	1.86	40.03	12	1.86(1)	17.0	8.5	2850–3100	1.03	2.07	2.15	1.80	
28	912	$\gamma_1$	2.13(5)	2.22	104.38	12	2.17(18)	16.8	11.3	850–970	-1.49	-1.03	-1.10	-1.46	
46	1320	$\gamma_1$	2.19(3)	2.30	129.82	12	2.00(37)	16.8	11.3	1270–1370	-2.04	-0.91	-0.95	-0.98	
46	4497	$\gamma_2$	3.31(8)	3.32	91.06	16	3.31(13)	16.8	12.2	4400–4600	-1.89	-1.17	-1.23	-1.75	
12	1270	$\delta$	1.54(2)	1.64	173.00	12	1.71(1)	17.0	12.0	1250–1310	-0.91	-2.41	-2.53	-1.88	
28	1370	$\delta$	1.85(3)	1.93	115.49	12	NA	NA	NA	-0.98	-1.89	-1.97	NA		
46	1626	$\delta$	2.22(4)	2.33	126.02	12	2.17(15)	17.0	10.5	1590–1690	-1.10	-3.00	-3.01	-1.96	

up in the XRD and multiple peaks observed in the FFT at particular angles – see for example  $\alpha$  towards the [100] direction above  $\sim 20^\circ$  in figure 4.3.5. There are approximately half a dozen separate peaks observed at this location which implies a similar amount of misaligned domain orientations. This misalignment however does not appear to affect the overall data which largely does not resolve the extra domains.

The Fermiology is largely solved by the angle plots with only a few minor ambiguities. The  $F \cos \theta$  angle dependent plots clearly show approximately level curves for the two hole Fermi surfaces demonstrating that  $\alpha$  and  $\beta$  are approximately two-dimensional. The hole surface,  $\gamma$ , deviates at high angles and  $\delta$  is strongly three dimensional. Although we cannot say for certain whether  $\gamma$  is pinched off or not, based on the rigidly shifted DFT we expect that the minima to be small but not zero and was not observed due to low frequency noise in the oscillations.

Previous dHvA measurements on  $\text{BaFe}_2(\text{As}_{0.37}\text{P}_{0.63})_2$  by Analytis *et al.* [22] shown in figure 4.3.6 identified the branch of the dHvA angle data at around 500 T as the neck of the 2D hole pocket. In our own analysis, it made much more sense to attribute this curve to the neck portion of the 3D hole band, with the neck of the 2D pocket being buried in the low frequency noise. These two different statements are not necessarily incompatible. Since the DFT data for the entire series suggests that whilst the 2D hole pocket retains the same shape along the  $\text{BaFe}_2(\text{As}_{1-x}\text{P}_x)_2$  series, the 3D hole pocket narrows considerably at the  $\Gamma$  point and switches from being concentric with the 2D pocket at  $x = 1$  to crossing through the 2D pocket as  $x$  is reduced. However when the spin-orbit interaction is considered in the DFT calculations, the crossing of the surfaces causes the bands to be redefined such that the bands do not actually cross, in which case there would not be a Yamaji point as specified in the Analytis paper since the similarly sized orbits at  $50^\circ$  angle are not from the same band. An attempt was made to see if there was an enhancement of the oscillation amplitude at the corresponding putative Yamaji point in the  $\text{BaFe}_2\text{P}_2$  data but the close proximity of the strong oscillations from the electron pockets made this intractable with this particular data set.

Although the Fermi surface appears to nest at the  $q = (\pi, \pi, \pi/4)$  as shown in figure 4.6.5, the corresponding imaginary part of the susceptibility data shows stronger enhancements at the  $q = (\pi, \pi, \pi/2)$  vector, primarily due to the nesting between the 3D hole Fermi surface and the inner electron surface. However the susceptibility calculations do not take into account the orbital character of electrons at these nesting vectors. The dominant character at  $q = (\pi, \pi, \pi/2)$  is between regions of  $d_{xz} + d_{yz}$  on the narrow portion of the 3D surface and regions that switch between  $d_{xy}$  and  $d_{xz} + d_{yz}$  on the electron surface. This will suppress the scattering between the two due to considerations of angular momentum. Nonetheless the susceptibility shows there are significant enhancements of the imaginary part of the susceptibility response between the electron and hole surfaces and the partial nesting conditions required for spin fluctuations are satisfied. Given that that

the system becomes more two dimensional as we approach the superconducting region, this suggests that the nesting is enhanced and the fluctuations become stronger.

Like previous measurements of band structure by dHvA in the  $\text{BaFe}_2(\text{As}_{1-x}\text{P}_x)_2$  materials, the Fermi surfaces are smaller than predicted by DFT calculations [20, 22]. Ortenzi *et al.* [113] posits an explanation based on interband scattering which leads to shrinking of the electron and hole pockets and an enhancement of the effective mass based on relaxing an assumption on the chemical potential being far\* from the electron/hole band edges. Similar moderate effective mass enhancements to what we found in  $\text{BaFe}_2\text{P}_2$  of around  $1.4m_e$  were calculated — albeit modelled on a more two dimensional pnictide, LaFePO — along with the fact that the theory predicts stronger shifts where interband coupling occurs is supported by the  $\text{BaFe}_2\text{P}_2$  data. The nested portions of the 3D  $\delta$  hole band, for example, is strongly shifted where it nests with the electron band but the bulge which does not nest with anything is not shifted at all. Similar shifts between the measured data and calculations were observed for the sister 122 compound  $\text{SrFe}_2\text{P}_2$  [11] which is also a partially nested material and yet shifts are notably absent for the non-nested 122 pnictide compound  $\text{CaFe}_2\text{P}_2$  [9] which matched the DFT calculations with no adjustments to the energies.

It is not clear at this stage whether the shifting of the Fermi surface proportional to the electron character for the 3D hole  $\delta$  band performed in section 4.3.1 represents anything physical or is simply a convenient and reproducible way to obtain the correct band topology. Settling this question will require further investigation. However it is interesting to note that the energy shifts for the 3D hole surface are proportional to the  $d_{z^2}$  and  $d_{xz}+d_{yz}$  characters, suggesting there may be a link between the  $k_z$  scattering component and energy enhancements. Recalling that we expect to see the strongest nesting component between the 3D hole surface and the inner electron pocket, this also suggest that the scattering between layers may play a part in suppressing superconductivity.

The wide bulge in the 3D hole surface ensures that several terms are needed for the harmonic fits represented in section 4.5. For this reason, the harmonic fits simply represent a convenient way to obtain the Fermi surface topology in the case of the 3D hole pocket.

---

\*‘Far’ in this case means greater than the scattering boson energy scale.

# Chapter 5

## Hall measurements on BSCO2201

---

Low (1.5 K) to high (300 K) temperature Hall measurements are presented on BSCO2201 over a wide doping range spanning the slightly underdoped to the far overdoped. The Hall and resistivity data is modeled using the Ong construction to determine the relative magnitudes of the scattering terms and is found to match the resistivity data within a factor of 2.5 in the underdoped samples. In addition a novel doping assignment scheme based on new Tl2201 dHvA results is trialled and was found to give slightly higher dopings than the Ando method which compares room temperature Hall data to LSCO and the Presland/Tallon method which scales normalised  $T_c$  values to a ‘universal’ parabola.

---

### 5.1 Sample growth

The samples were grown by Prof. Takeuchi’s group in Sendai University, Japan in May 2009 using the floating zone technique. Here powders of the correct stoichiometry are compacted into a rod and fed slowly through a furnace. A region towards the centre of the furnace heats the powders into a viscous melt, just below this region is a seed crystal. As the end of the rod passes through the melt region, it meets the seed crystal below and solidifies epitaxially onto it. The impurities are held in the melt portion of the crystal by a thermodynamic energy gradient. The rod continues to be slowly passed through the melt region, continually solidifying into the single crystal below until the entire rod has passed through and the growth is over. The end portion, containing the impurities is then removed. Samples from the same growth batch have previously been studied using ARPES and STM by members of the Sendai group [74, 114–119].

Table 5.1 lists the nominal stoichiometries of the samples grown as well as the annealing conditions. Also listed are the *nominal*  $T_c$  values for the source crystals which are used to name the samples, the actual measured  $T_c$  values of individual samples for the purposes of doping determination are slightly different due to different definitions of  $T_c$ \*.

---

\*The source crystals were defined based on the zero value  $T_c$ , the  $T_c$  for doping purposes is defined as the mid-point of the transition with an error based on the difference between the mid-point and the zero-point.

**Table 5.1:** Growth details for the BSCO2201 samples. OD, OP and UD stand for over, optimally and under doped respectively.  $T_c$  values are nominal.

Nominal composition								
Bi	Pb	Sr	La	Cu	O	$T_c$	Reg.	Annealing conditions
1.72	0.38	1.85	0.0	1.0	6+d	<2	OD	400 °C, 96 h in 2.5 atm. O <sub>2</sub>
1.72	0.38	1.85	0.0	1.0	6+d	7	OD	750 °C, 24 h in air
1.72	0.38	1.85	0.0	1.0	6+d	16	OD	550 °C, 72 h in flowing N <sub>2</sub>
1.35	0.85	1.47	0.38	1.0	6+d	30	OD	As grown
1.35	0.85	1.47	0.38	1.0	6+d	32	OP	650 °C, 72 h in flowing N <sub>2</sub>
1.2	0.90	1.30	0.55	1.0	6+d	30	UD	As grown
1.2	0.90	1.30	0.55	1.0	6+d	28	UD	650 °C, 72 h in flowing N <sub>2</sub>

The samples are named according the convention,

B< $T_c$ >K<UD/OP/OD><Crystal No.><Sample No.>

where UD/OP/OD stands for underdoped, optimally doped and overdoped respectively. So for example ‘B00KOD2A’ refers to the sample ‘A’ taken from the crystal ‘B00KOD2’ — the second overdoped crystal with a nominal  $T_c$  of 0 K.

## 5.2 Size determination

Thicknesses were determined for some of the samples using the FIB or the optical microscope as described in the methods section. These measurements were performed with the help of Dr. P. Heard. The thicknesses used to calculate absolute values of  $R_H$  are listed in table 5.2 and are marked in grey. FIB results are given for areas as close to the two voltage contacts that were visible in the scans. As can be seen in the example scan shown in figure 5.2.1, there is some variation in the depth along the sample length.

The two scans shown are of good quality, however for the purpose of estimating errors in the thickness some of the scans presented problems. Samples B26KOD1A, B28KUD3A, B30KOD2 and B30KUD3 were obscured with the grease applied as part of the pulsed field measurements. Other samples were not correctly earthed such as B28KUD3B which made the images dark, whilst samples B07KOD2 and B32KOP3 were very flaky under close scrutiny. A scan of B30KOD3 showed that it was partially split in the ab plane which may contribute to systematic error in thickness estimate. In all these cases, the estimate in the thickness error was adjusted accordingly to compensate. A more comprehensive set of FIB scans, including images of the split in the layers can be found in Appendix C.

The oblique view of B30KOD3 in figure 5.2.1 shows a clear misalignment of the voltage legs to the right of the image. This illustrates why it is necessary to take both positive and negative field sweeps in order to separate the magnetoresistance from the Hall components.

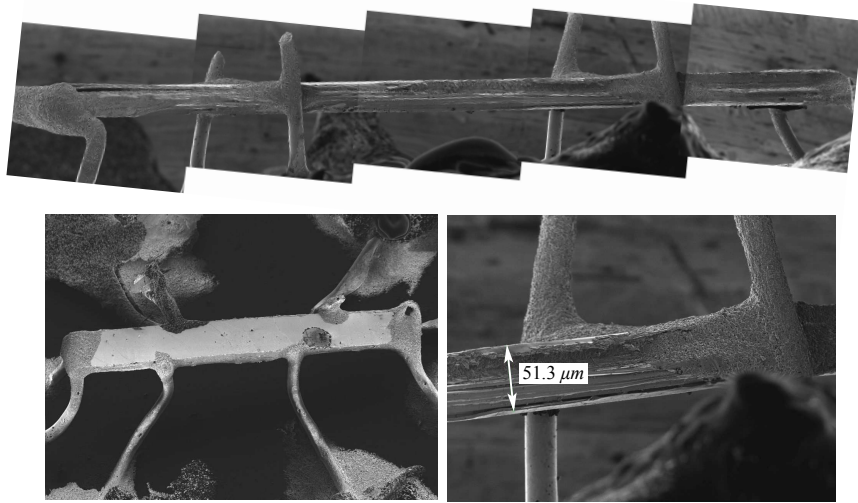


**Figure 5.2.1:** Top shows an image composited from several FIB scans along the length of sample B00KOD1A, with bottom right showing a detail of the right voltage leg. Bottom left shows an oblique top down view of sample B30KOD3.

This also explains why the length and width determinations were subject to large errors which affects the absolute value of the in-plane resistivity calculations.

### 5.3 Temperature sweeps

Figure 5.3.1 shows the in-plane resistivity,  $\rho(T)$  for each of the samples in zero field taken in the VTI in the 16 T ‘Polo’ magnet. Samples were mounted as described in section 3.3.1 for measurement using the six probe technique. The typical contact resistances were of the order of  $1\ \Omega$  to  $10\ \Omega$ . All measurements taken in the Polo magnet were taken by the author. From this plot we can characterise the  $T_c$  of the samples and find the residual resistivity,  $\rho_0$  as well as the linear and quadratic resistivity terms. This is done by using second order polynomial fits to  $\rho = \rho_0 + \rho_1 T + \rho_2 T^2$  to the data above the transition temperatures and extrapolate back to zero. Towards the overdoped side the resistivity is affected by a second linear region which signifies the onset of the pseudogap and so a reduced region is fitted which is marked in figure 5.3.2 which is found by examining the derivative of the resistivity. Table 5.3 show the fit parameters for each of the samples. The residual resistivities are very good with only one being above  $100\ \mu\Omega\text{cm}$  and most below  $70\ \mu\Omega\text{cm}$  which has been cited as being exceptionally good for BSCO2201 [78]. Moreover the  $T_c$  of the optimally doped sample is 36 K which is amongst the highest reported [78] which again is testament to the crystal quality.

The mid-transition  $T_c$  values were extracted from the plots with the error determined

**Table 5.2:** Sample measurements as determined by optical microscope measurements and thickness as determined by FIB. Samples highlighted in grey were used for determining absolute values of  $R_H$ . A and B refer to each of the two contacts visible to the FIB scan.

Sample	Length (μm)	Optical Width (μm)	Thick. (μm)	Contact A (μm)	FIB Contact B (μm)
B00KOD1A	$781 \pm 123$	$157 \pm 49$	N/A	$45 \pm 1$	$50 \pm 5$
B00KOD1B	$627 \pm 49$	$196 \pm 44$	$39 \pm 5$	$43 \pm 1.5$	$45 \pm 1.5$
B07KOD1	$1277 \pm 74$	$392 \pm 49$	$29 \pm 10$	N/A	N/A
B07KOD2	$1061 \pm 69$	$333 \pm 74$	N/A	$20 \pm 5$	$30 \pm 1$
B16KOD1A	$795 \pm 34$	$299 \pm 34$	N/A	$24 \pm 1$	$24 \pm 1$
B16KOD2A	$358 \pm 29$	$172 \pm 54$	$9 \pm 1$	N/A	N/A
B16KOD3	$1122 \pm 44$	$368 \pm 83$	N/A	$25 \pm 2$	$24 \pm 2$
B30KOD1	$436 \pm 34$	$250 \pm 44$	$21 \pm 2$	N/A	N/A
B30KOD2	$344 \pm 44$	$137 \pm 29$	$20 \pm 5$	$15 \pm 4$	$15 \pm 4$
B30KOD3	$255 \pm 49$	$98 \pm 25$	N/A	$16.5 \pm 1.5$	$19 \pm 1$
B32KOP1	$658 \pm 83$	$397 \pm 34$	N/A	$6.5 \pm 1.5$	$6.5 \pm 1.5$
B32KOP2	$441 \pm 25$	$226 \pm 20$	$10 \pm 1$	N/A	N/A
B32KOP3	$437 \pm 34$	$118 \pm 20$	N/A	$6 \pm 1$	$6 \pm 1$
B32KOP4	$427 \pm 74$	$137 \pm 39$	N/A	$9 \pm 3$	$9 \pm 3$
B30KUD1A	$622 \pm 49$	$447 \pm 25$	$36 \pm 3$	N/A	N/A
B30KUD1B	$828 \pm 34$	$471 \pm 64$	$35 \pm 3$	N/A	N/A
B30KUD2	$545 \pm 69$	$152 \pm 39$	N/A	$5 \pm 1$	$5 \pm 1$
B30KUD3	$476 \pm 49$	$118 \pm 34$	N/A	$7 \pm 2$	$7 \pm 2$
B28KUD2A	$657 \pm 29$	$250 \pm 39$	$11 \pm 1$	N/A	N/A
B28KUD3A	$633 \pm 49$	$142 \pm 34$	N/A	$16 \pm 3$	$16 \pm 3$
B28KUD3B	$653 \pm 44$	$216 \pm 49$	N/A	$16 \pm 3$	$16 \pm 3$

**Table 5.3:** Fit parameters to  $\rho = \rho_0 + \rho_1 T + \rho_2 T^2$  for zero field resistivity data above  $T_c$  as well as  $T_c$  values determined from the same plots. Fits are shown in figure 5.3.2.

Sample	$\rho_0$ (mΩcm)	$\rho_1$ (mΩcm/K)	$\rho_2$ (mΩcm/K <sup>2</sup> )	$T_c$ (K)	$T_c/T_c(\max)$
B00KOD1A	$5.070 \times 10^{-2}$	$2.634 \times 10^{-4}$	$6.172 \times 10^{-7}$	$0 \pm 1.0$	$0.00 \pm 0.03$
B07KOD2	$9.042 \times 10^{-2}$	$7.433 \times 10^{-4}$	$8.733 \times 10^{-7}$	$11 \pm 3.8$	$0.31 \pm 0.11$
B16KOD1A	$6.012 \times 10^{-2}$	$6.775 \times 10^{-4}$	$5.092 \times 10^{-7}$	$17 \pm 1.0$	$0.47 \pm 0.03$
B30KOD3	$2.151 \times 10^{-2}$	$4.911 \times 10^{-4}$	$2.427 \times 10^{-7}$	$29 \pm 0.5$	$0.81 \pm 0.01$
B32KOP1	$6.602 \times 10^{-2}$	$5.483 \times 10^{-4}$	$1.401 \times 10^{-6}$	$36 \pm 1.0$	$1.00 \pm 0.03$
B32KOP4	$6.041 \times 10^{-2}$	$1.619 \times 10^{-3}$	$2.041 \times 10^{-6}$	$35 \pm 2.0$	$0.97 \pm 0.06$
B30KUD3	$1.234 \times 10^{-1}$	$2.128 \times 10^{-3}$	$1.085 \times 10^{-6}$	$32 \pm 1.0$	$0.89 \pm 0.03$
B28KUD3A	$2.379 \times 10^{-2}$	$7.237 \times 10^{-4}$	$5.979 \times 10^{-7}$	$32 \pm 1.0$	$0.89 \pm 0.03$

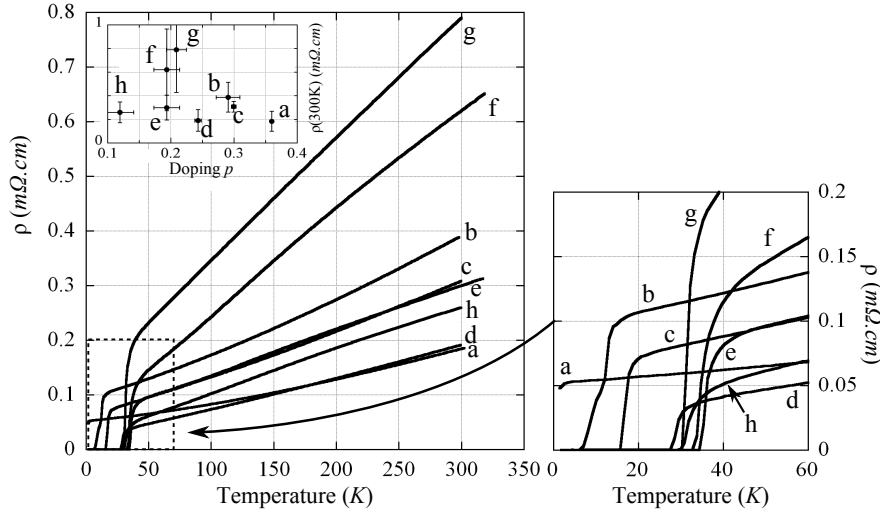


**Figure 5.3.1:** The in-plane resistivity measured in zero field. From nominally overdoped to underdoped, samples are (a) B00KOD1A, (b) B07KOD2, (c) B16KOD1A, (d) B30KOD3, (e) B32KOP1, (f) B32KOP4, (g) B30KUD3, (h) B28KUD3A. Right panel shows a zoomed portion of the curves at the transition temperatures along with continuations of fits to portion of the curve above  $T_c$  in red. Inset shows  $\rho(300\text{ K})$  vs. doping (as determined by matching Rh with that of Tl2201, see section 5.5) with errors due to size determination.

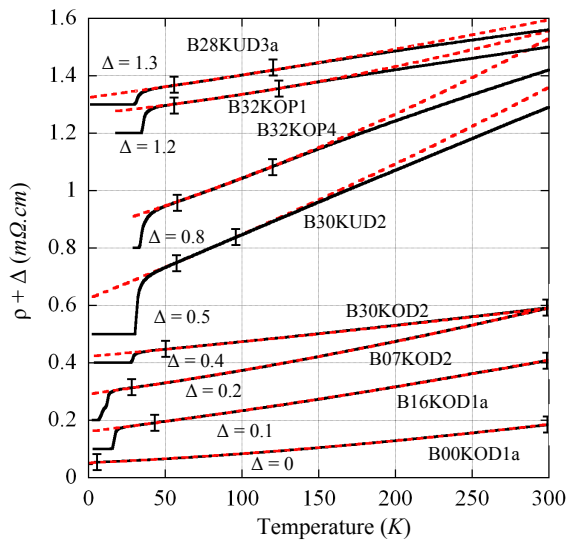


**Figure 5.3.2:** Resistivity curves plus the fits to  $\rho = \rho_0 + \rho_1 T + \rho_2 T^2$ . Bars on the plots delimit the fit regions used.

from the difference between the mid point and the zero resistance point. Results are listed in table 5.3 as well as the normalised  $T_c$  values,  $T_c/T_c(\text{max})$ , with  $T_c(\text{max}) = 36$  K.

The inset to figure 5.3.1 shows the  $\rho(300\text{ K})$  values for the samples along with vertical error bars due to uncertainty in the length determination. As we saw in the previous section, there is some misalignment of the voltage contacts which lead to systematic errors in length.

## 5.4 Hall plots

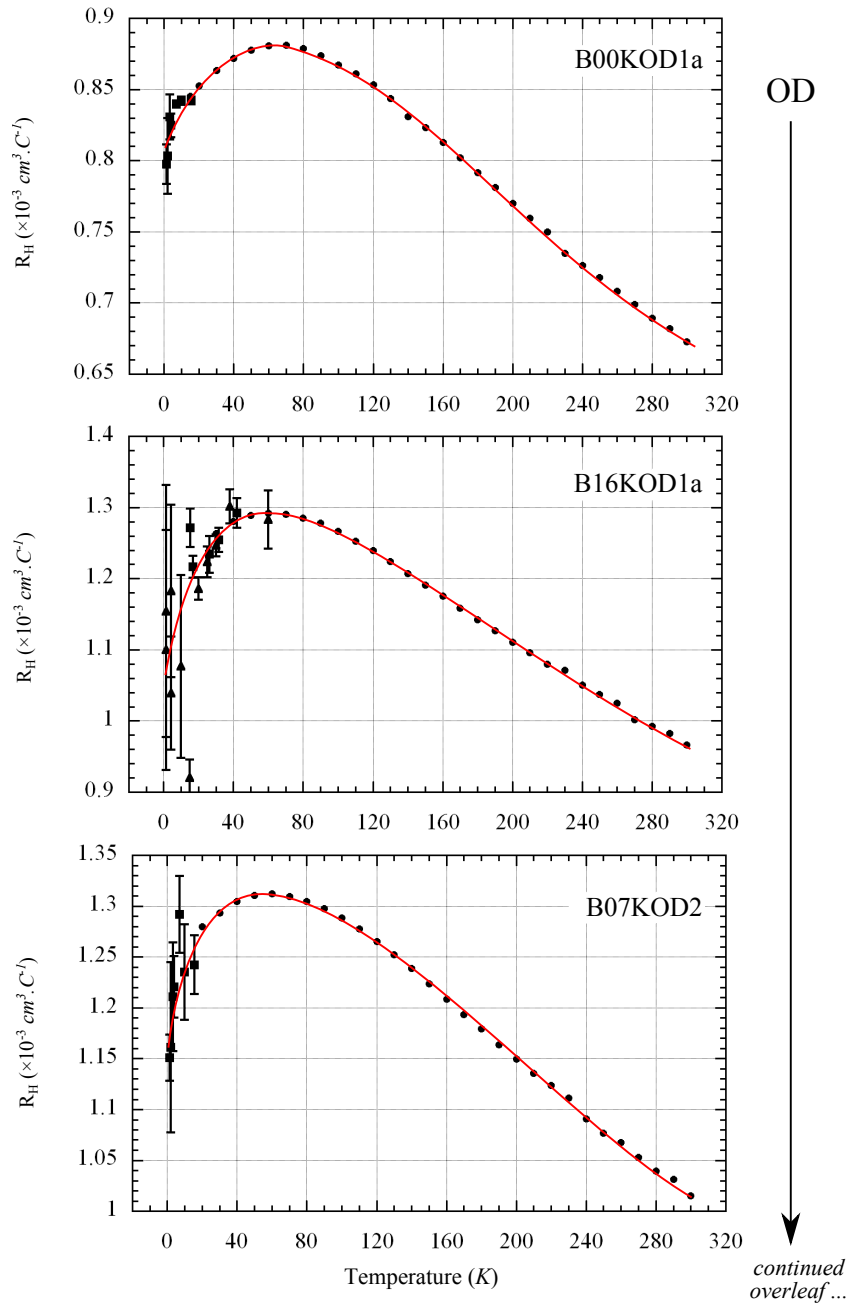
The data presented here was taken by a various people at various facilities. For full details see section 1.4.3. of The overarching six-probe measurement technique is used for all the transport measurements with differences chiefly in measurement geometry and apparatus.

Figures 5.4.1, 5.4.2 and 5.4.3 show the Hall coefficients extracted as described in the methods section for samples progressing from overdoped, optimally doped to underdoped respectively. Where appropriate, the data is alongside that from Ando *et al.* [78] for comparison. Red lines in the plots are guides to the eye.

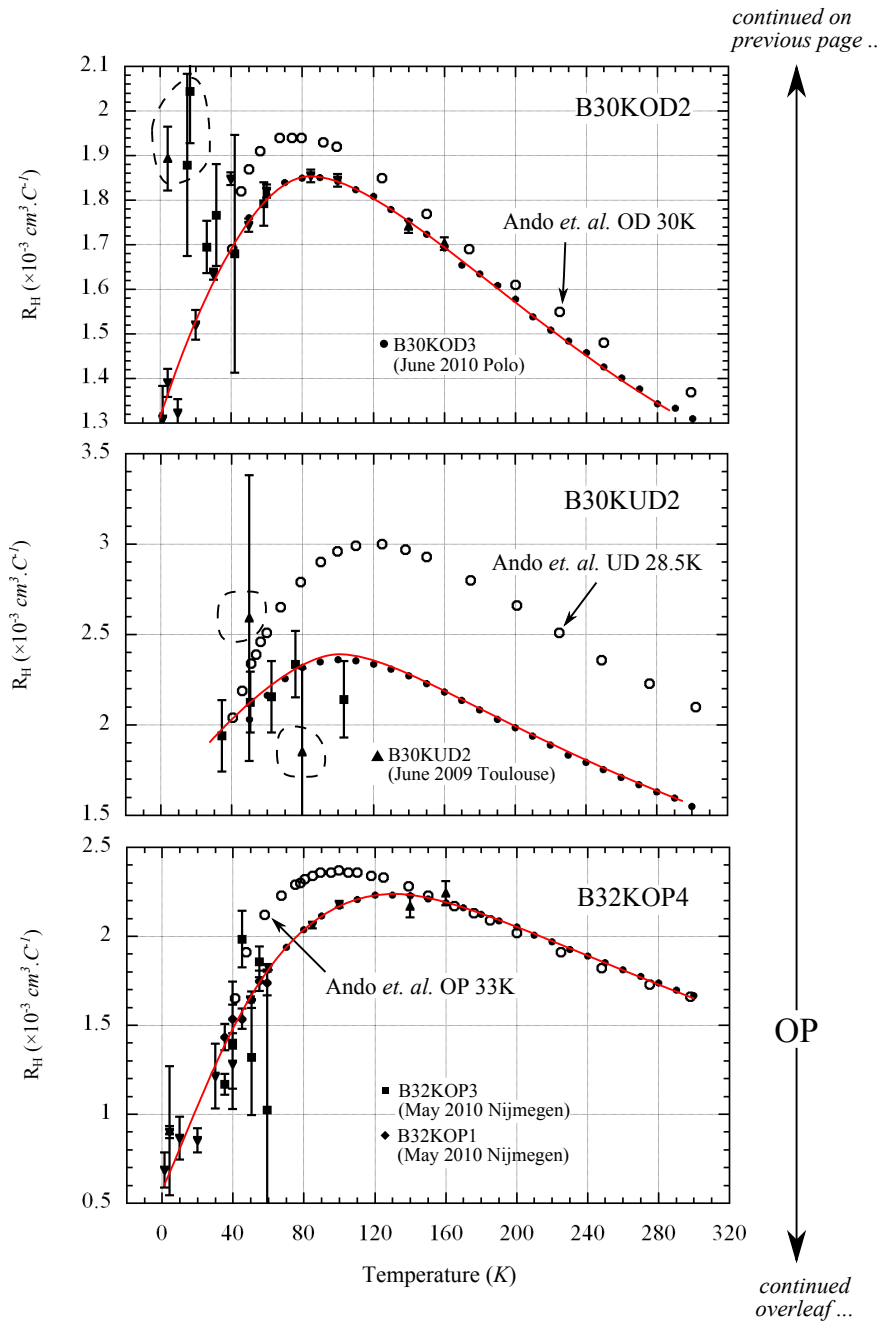
For the samples of  $T_C \leq 28$  K there are some data which did not reach sufficient field to obtain linear behaviour which are circled with a dashed line in the plots. For sample B30KOD2, many of the sweeps for  $T < 45$  °C showed significant hysteresis due to temperature drift. Despite temperature correction, many of the fits did not pass through the origin (circled in the figure) which is a good indicator that the true field suppressed linear Hall has not been obtained. The same goes for the circled points on the B30KUD2 plot and another data point at  $T = 1.5$  K and  $R_H = 7.3 \times 10^{-3}$  cm<sup>3</sup> from the first trip to LNCMI which is outside the plot boundary as well as data points on the plot for B28KUD3B. The data sets are combined, minus the points highlighted in the previous paragraph, in the main panels of figure 5.4.4 alongside the data from the Ando paper.

The error bars on the data points do not include error from the thicknesses which are systematic across the data points. The inset of figure 5.4.4 shows the  $R_H$  values at 300 K vs. doping for each of the samples with these error bars applied. The overall trend in  $R_H(300\text{ K})$  is downward due to the fact that  $R_H(300\text{ K})$  values for Tl2201 also trend downwards and the dopings were assigned by matching to this data — see section 5.5 for details.

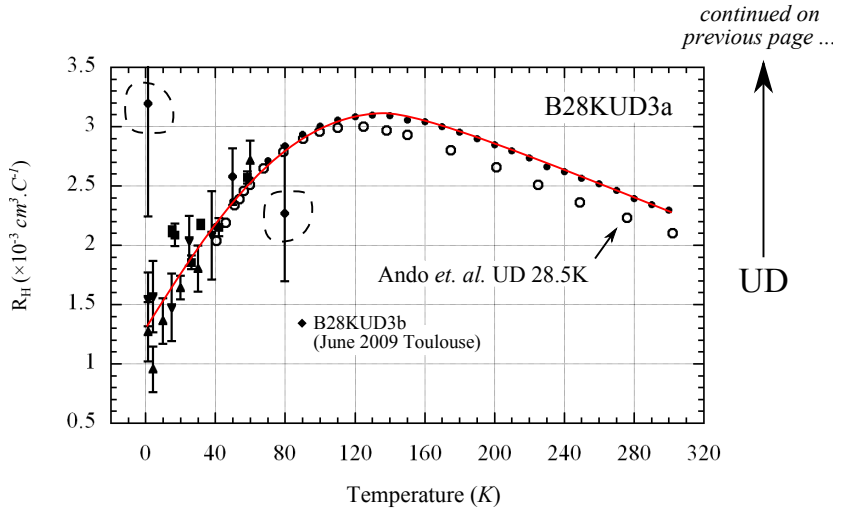
With reference to figure 5.4.4 and in particular the new low temperature data points, we see that doping strongly affects the qualitative shape of the  $R_H$  curves. The curves have a temperature dependence which is stronger on the underdoped side which gradually becomes less pronounced as doping increases, however all curves show a maximum in  $R_H$  at some point along the temperature axis. For the more underdoped samples the behaviour below  $R_H(\text{max})$  appears linear in temperature, however the error bars preclude resolving if there is a levelling off at 10 K to 20 K which Balakirev *et al.* found in strongly underdoped



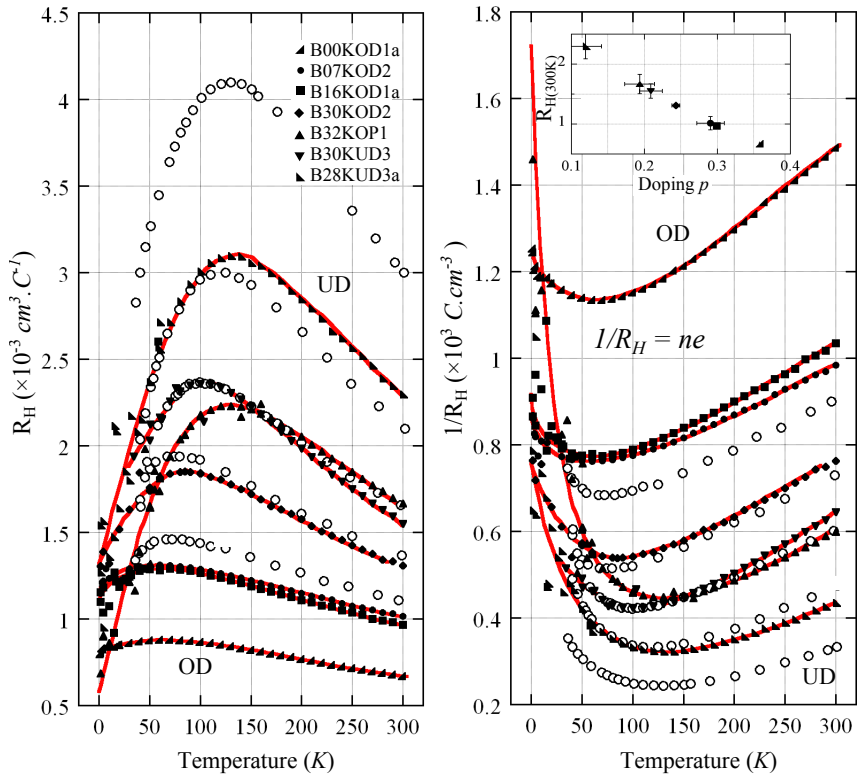
**Figure 5.4.1:**  $R_H$  for underdoped samples of BSCO2201. Plots show results from, • Polo in June 2010, ▲ LNCMI in June 2009, ▼ LNCMI in Feb 2010, ■ Nijmegen in May 2010. Symbols for comparable samples are marked on the plots. Red lines are a guide to the eye.



**Figure 5.4.2:**  $R_H$  for underdoped samples of BSCO2201. Plots show results from, • Polo in June 2010, ▲ LNCMI in June 2009, ▼ LNCMI in Feb 2010, ■ Nijmegen in May 2010. Symbols for comparable samples are marked on the plots. Dashed lines indicate points where the field was not sufficient to achieve linear behaviour. Red lines are a guide to the eye.

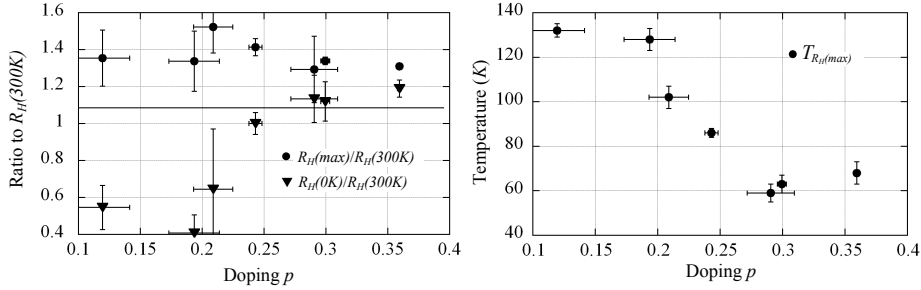


**Figure 5.4.3:**  $R_H$  for underdoped samples of BSCCO2201. Plots show results from, • Polo in June 2010, ▲ LNCMI in June 2009, ▼ LNCMI in Feb 2010, ■ Nijmegen in May 2010. Symbols for comparable samples are marked on the plots. Dashed lines indicate points where the field was not sufficient to achieve linear behaviour. Red lines are a guide to the eye.



**Figure 5.4.4:** Hall data in context with data from Ando *et al.* [78] (open circles) which are in order of increasing  $R_H$ , 24KOD, 30KOD, 33KOP, 28.5KUD, 20KUD. Right panel shows the inverse hall data which relates to carrier density. Red lines are the same guides to the eye used in previous figures. Inset shows  $R_H$  at 300 K plus systematic error bars due primarily to uncertainty in thickness vs. doping determined from scaling  $R_H$ (300 K) to Tl2201 data.

BSCO2201 samples [79]. The low temperature  $R_H$  values all tend towards approximately similar values of around  $0.5 \times 10^{-3} \text{ cm}^3/\text{C}$  to  $1.5 \times 10^{-3} \text{ cm}^3/\text{C}$ . The most pronounced difference between high and low temperature values though is with the optimally doped samples which are around  $\times 2.75$  greater at high temperature. None of the curves exhibit a change in sign right down to 0 K.



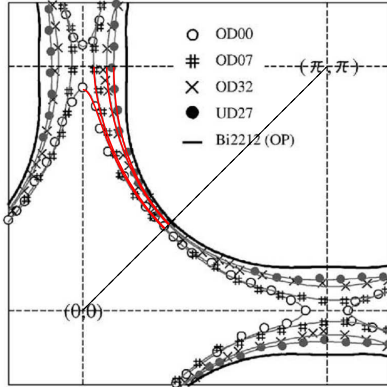
**Figure 5.4.5:** Left shows ratio of  $R_H$  values at the maximum of the Hall curves and at  $T = 0$  K to the  $T = 300$  K  $R_H$  values. Errors in  $R_H(0$  K estimated from Hall plots, the value for B30KUD2 is estimated based on linear extrapolation. Right shows the temperature where the maximum  $R_H$  occurs.

Figure 5.4.5 shows the ratio of the  $R_H(0$  K)/ $R_H(300$  K) values and  $R_H(\max)$ / $R_H(300$  K) values where  $R_H(\max)$  is where the curve reaches its maximum value. We can see relatively little change in  $R_H(\max)/R_H(300$  K) across the dopings, however the low temperature value drops off significantly at around  $p = 0.25$  and for the purpose of comparison with literature this corresponds to  $p = 0.19$  as determined by the Presland/Tallon relation. This coincides to a multitude of phenomena which are thought to be associated with the pseudogap [61]. Since we observe this in the normal state below the superconducting dome, this suggests that the drop is also associated with the pseudogap and that the third scenario described in 1.3.4 where the pseudogap merges with the superconducting gap at the top of the superconducting dome is not the correct one.

#### 5.4.1 Anisotropic model based on the Ong construction

To try and understand the Hall behaviour and whether this could be a result of an anisotropic scattering term in the overall scattering rate we attempt to model the data based on the Ong construction [105] which was detailed in section 2.6.1. We use Fermi surface data obtained by our collaborators by ARPES on crystals taken from the same batch [80]. Where data for a particular doping was not available, an interpolation was used between two known dopings. We assume a 2D Fermi surface and that the orthorhomobicity is slight enough that we can approximate fourfold symmetry and overlay four point Bezier curves as shown in figure 5.4.6 in order to obtain a well behaved analytic function representing the Fermi surface shape. These were checked against data points extracted

from the plots in the code and the symmetrised Fermi surface was checked against the original Fermi surface presented in the Kondo paper.



**Figure 5.4.6:** Fermi surfaces from the Kondo paper [80] with Bezier curves overlaid spanning 1/8th of the circumference of the Fermi surface

We then supposed a three term scattering rate as  $\Gamma = \Gamma_0 + \Gamma_1 \cos^2(2\phi)T + \Gamma_2 T^2$  which includes the anisotropic scattering rate proposed by Abdel-Jawad *et al.* [120] and discussed in section 1.3.6.  $R_H$  calculated in this way is invariant to scaling of the overall magnitude of  $\Gamma$  since the longitudinal conductivity terms cancel the transverse conductivity term. Because of this, we only fit the relative magnitudes of  $\Gamma_0$ ,  $\Gamma_1$  and  $\Gamma_2$ . Keeping the  $\Gamma_2$  term constant and adjusting the anisotropic scattering term,  $\Gamma_1$ , for the Fermi surfaces examined results in an overall scaling of the temperature dependent  $R_H$  curve as shown in the right panel of figure 5.4.7. Keeping  $\Gamma_2$  constant and increasing  $\Gamma_0$  results in  $R_H(\max)$  occurring at higher temperatures as well as a decrease in  $R_H$ . By first tuning  $\Gamma_0$  to obtain the correct temperature at which  $R_H(\max)$  occurs, then tuning  $\Gamma_1$  to obtain the correct  $R_H(0\text{ K})/R_H(\max)$  ratio the best match to the curves was determined.

Figure 5.4.8 shows the resulting  $R_H$  curves. The resulting parameters are shown in table 5.4 and are expressed as terms of a fit to a longitudinal resistivity curve, i.e.  $\rho^{R_H} = \rho_0^{R_H} + \rho_1^{R_H} \cos^2(2\phi)T^2 + \rho_2^{R_H} T^2$ .  $\rho^{R_H}(T)$  is normalised to match the actual resistivity curves at  $T = 300\text{ K}$  given in table 5.3. Since the  $\cos^2$  anisotropic term is averaged over the Fermi surface to obtain resistivity\*, this introduces a factor of 1/2 in the  $\rho_1$  fitted resistivity term. The  $\rho_1^{R_H}$  term is therefore halved to compare with the value from the anisotropic model. Ratios of the values of the two fitting methods are also shown in table 5.4.

In general the resulting ratios only match up very approximately, to within an order of magnitude, however the  $T$ -linear term from the anisotropic model matches the corresponding term from the resistivity reasonably well, ranging between 0.6 and 1.5 times the resistivity values. We see some systematic behaviour with the residual resistivity value,

\*See the conductivity equation in section 2.6.1.

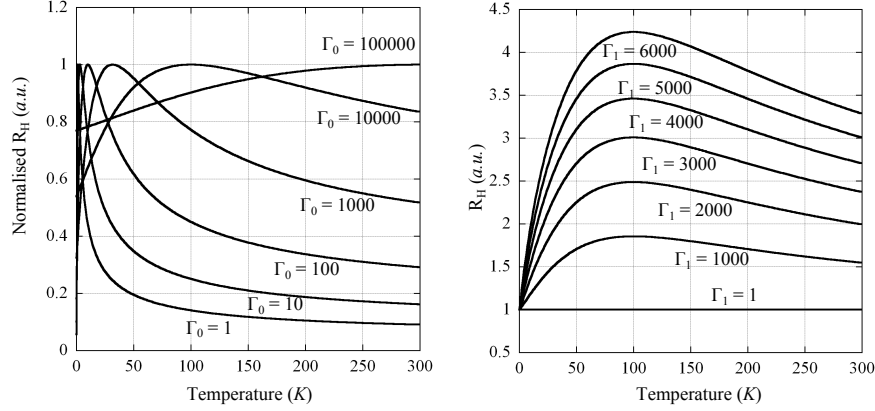


**Figure 5.4.7:** Left panel shows how the temperature dependence of  $R_H$  changes when the  $\Gamma_0$  scattering term is adjusted. Curves are normalised to their maximum value. Right panel shows the scaling of  $R_H$  resulting from the adjustment of the anisotropic  $\Gamma_1$  term. Both sets of data were taken using the Fermi surface for UD27K.

**Table 5.4:** The scattering terms obtained by the anisotropic model and their ratios compared to the resistivity fits. The anisotropic model terms are normalised to match the  $T = 300$  K value for the resistivity data.

Sample	$\rho_0^{R_H} \times 10^{-3}$	$\rho_1^{R_H} \times 10^{-4}$	$\rho_2^{R_H} \times 10^{-7}$	$\rho_0^{R_H}/\rho_0$	$\rho_1^{R_H}/\rho_1$	$\rho_2^{R_H}/\rho_2$
B00KOD1a	$7.50 \pm 0.9$	$3.67 \pm 1.1$	$16.31 \pm 2.8$	0.1	0.7	2.6
B16KOD1a	$11.92 \pm 2.6$	$7.75 \pm 4.1$	$29.79 \pm 7.4$	0.2	0.6	5.9
B07KOD2	$12.91 \pm 2.8$	$8.92 \pm 4.9$	$37.16 \pm 9.5$	0.1	0.6	4.3
B30KOD2	$10.31 \pm 1.2$	$6.75 \pm 1.5$	$13.84 \pm 1.6$	0.5	0.7	5.7
B30KUD3	$19.72 \pm 15.3$	$43.62 \pm 1.6$	$18.88 \pm 14.8$	0.2	1.0	1.7
B32KOP4	$12.62 \pm 5.1$	$37.79 \pm 2.4$	$7.70 \pm 3.2$	0.2	1.2	0.4
B32KOP1	$5.41 \pm 2.2$	$16.20 \pm 9.5$	$3.30 \pm 1.4$	0.1	1.5	0.2
B28KUD3	$9.60 \pm 3.8$	$15.09 \pm 9.0$	$5.52 \pm 2.2$	0.4	1.0	0.9

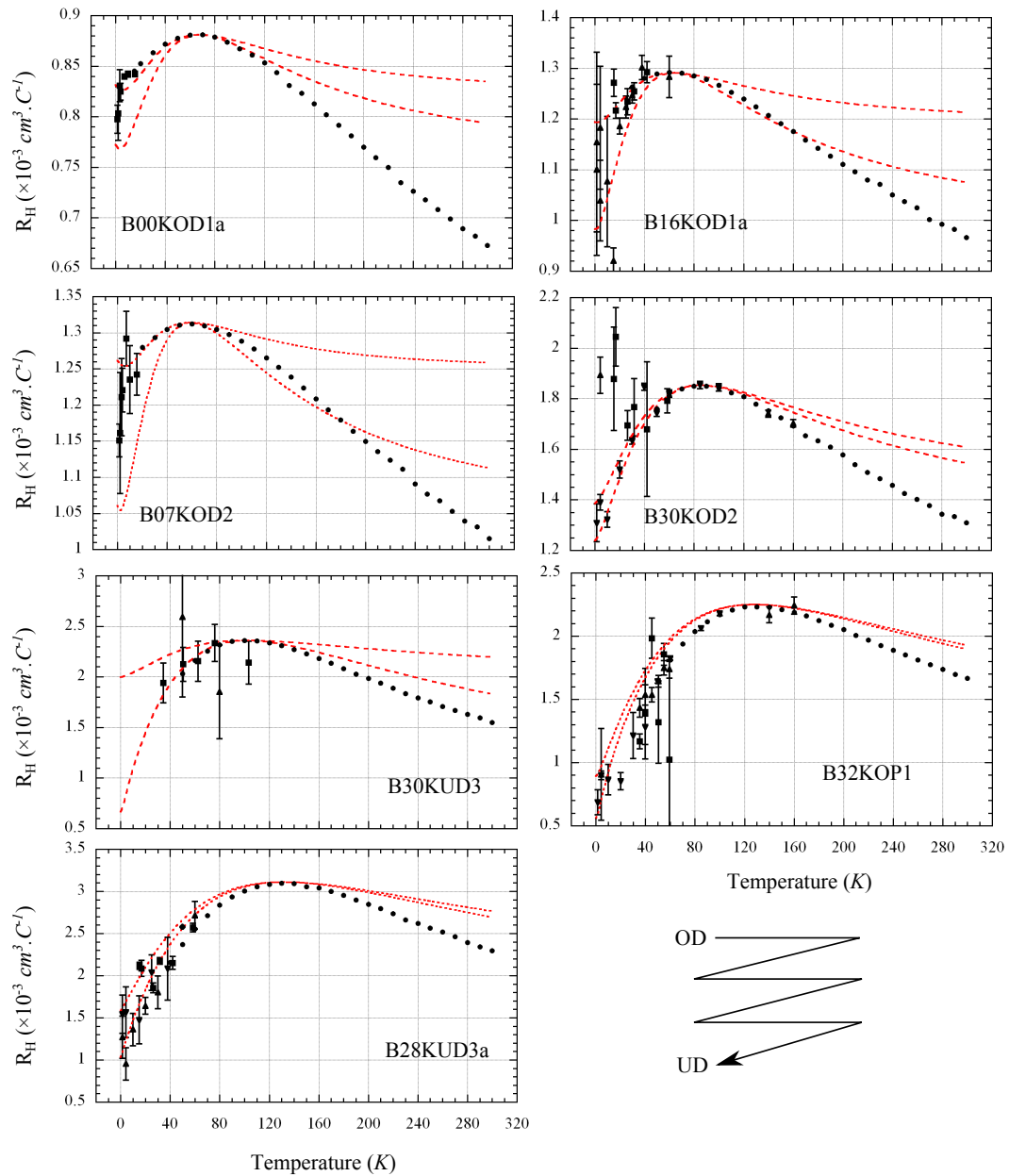


**Figure 5.4.8:** Hall data with data generated from the Ong construction overlaid in red. Bounds to account for the uncertainty in the  $R_H(0 \text{ K})$  values are shown. Bounds for the uncertainty in the temperature of the maximum of  $R_H$  are not shown since they vary very little.

OD  
UD

$\rho_0^{RH}$  being consistently undervalued by a factor of 2 to 10. For the overdoped samples the  $T^2$  factor is around 2.6 to 5.9 times higher than expected and for the underdoped samples is up to a factor of 5 lower than the resistivity fits show which suggests that perhaps there is a doping dependence to the  $T^2$  term. We also observe an increase in the linear in  $T$  term with doping and  $T_c$  similar to that found by Abdel-Jawed *et al.* [120]. The  $\rho_1^{RH}$  values are plotted in figure 5.4.9. This is encouraging and supports the notion that it may be possible to model the Hall data in the cuprates, in particular the downturn in the Hall coefficient at low temperatures, without requiring the sort of Fermi surface reconstructions proposed by LeBoeuf *et al.* [63] detailed in section 1.3.5. It should be emphasised however that the data does not preclude the type of scenario described by LeBoeuf *et al.*.

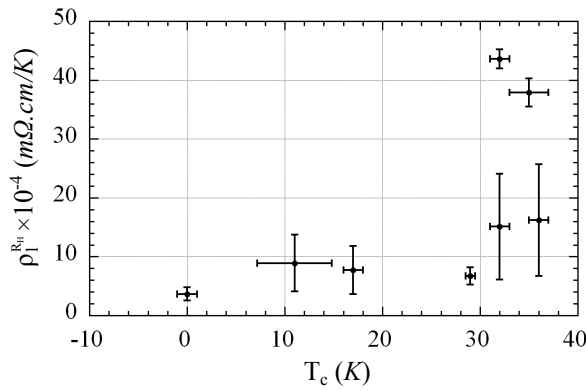


**Figure 5.4.9:** Linear in  $T$  terms determined from the anisotropic model fits plotted against  $T_c$  similar to Abdel-Jawed *et al.* [120]

It may be the case that refinements to the model will result in better agreement between the data and modeling  $v_F$  in the scattering rate will have significant effect close to the van-Hove singularity in the overdoped side. A prima-facie analysis suggests that it will enhance the anisotropy and therefore suppress the anisotropic linear in  $T$  term towards the overdoped side. Nonetheless a detailed investigation is required to see if this really is the case.

## 5.5 Doping determination

As described in section 1.4.2, we compared the Hall values of our samples at high temperature to determine the doping similar to the method used by Ando *et al.* [76]. In order to compare this method with other doping characterisation methods, the actual (i.e. not nominal)  $T_c$  values for the samples were used from the resistivity curves shown in figure 5.3.1. These values were input into the parabolic relation from Presland *et al.* [75] and Ando *et al.* [76]. This is then compared with the doping assignments which we make by matching  $R_H(300\text{ K})$  in the BSCO2201 data from the previous section with that com-

piled in Kokalj *et al.* [121] on Tl2201. The results of these comparisons are shown in figure 5.5.1. The Tl2201 data does not span the entire range of  $R_H(300\text{ K})$  values that

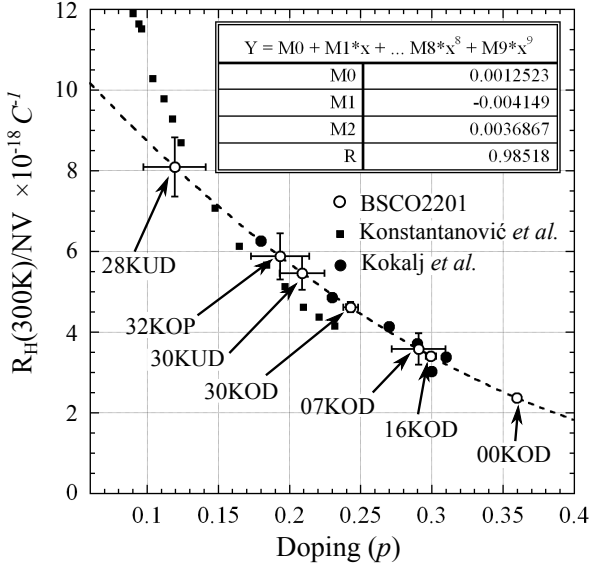


**Figure 5.5.1:** Assigning the dopings of the BSCO2201 data such that  $R_H(300\text{ K})$  values match those of Tl2201. Dashed line is a second order polynomial fit to the Tl2201 data that is used to obtain the exact dopings.

the BSCO2201 covers, for this reason a second order polynomial is fit to the Kokalj data and the BSCO2201 doping is assigned to this curve. The underdoped sample B28KUD3a is far along the extrapolated curve, however still lies within the standard Presland/Tallon assignment as used to determine the dopings for the Konstantanovic data [122].

Figure 5.5.2 shows the dopings as determined by the three different methods outlined in the experimental methods chapter. The dopings of the crystals range from  $p = 0.12$  to  $p = 0.36$  hole per Cu atom with significant discrepancies between the methods. The Ando determination bunches the doping values around a much narrower range, whereas the dopings determined by comparing with the Tl2201 dHvA data, spread the overdoped values over a wider range. The Presland/Tallon method sits between the two. Most notable is that the dopings assigned by Kondo *et al.* [80] from ARPES measurements of the Fermi surface volume taken at 200 K. These are for different samples from the same growth batch but show significantly higher still span of dopings between  $p = 0.25$  and  $p = 0.43$ . It is not clear why there is a discrepancy given that both determinations are based measure of the Fermi surface in the normal state (the dHvA being field induced at low temperature and ARPES being above  $T_c$ ), however we believe that the ARPES data may be subject to some kind of surface charge effect since it shows that the overdoped 0 K sample has passed the van-Hove singularity when our Hall data (obtained from the sample bulk) does not show any evidence for this.

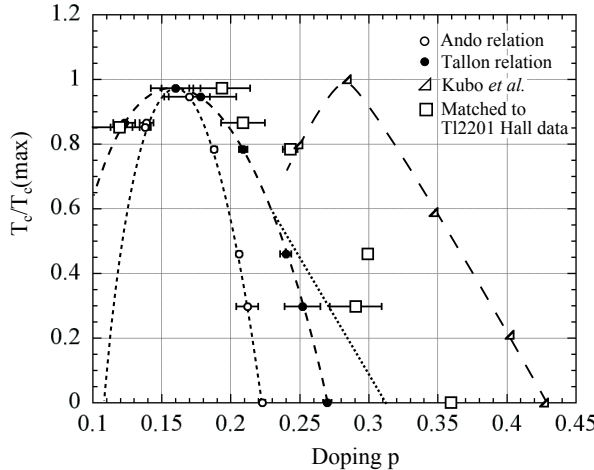


**Figure 5.5.2:** Doping distributions for the three different methods. From left to right, B28KUD3A, B30KUD3 (Assume UD), B32KOP1, B32KOP4, B30KUD3 (Assume OD), B30KOD3, B16KOD1A, B07KOD2, B00KOD1A. Broken lines are a guide to the eye. Circled points are B30KUD3 for both the overdoped and underdoped scenarios.

## 5.6 Conclusions

High quality crystals of Pb and Sr doped BSCO2201 were sourced and studied in the normal state by high-field magnetotransport measurements down to low temperatures, thereby determining the low temperature Hall behaviour. The samples exhibited a sharp change in the  $R_H(0 \text{ K})/R_H(300 \text{ K})$  which coincides with various phenomena related to the pseudogap. This occurs in the field induced normal state which suggests that the scenario described in section 1.3.4 where the pseudogap disappears at the top of the superconducting dome is not the correct one.

The data was modelled using a simple anisotropic model based on the Ong construction and was found to fit the relative scattering rates in the reasonably well it although consistently underestimated the residual resistivity term and for the overdoped samples overestimated the  $T^2$  term. An increase in the  $T$ -linear term was observed to scale with doping similar to as found by Abdel-Jawad *et al.* [120]. This relatively crude model suggests that with further refinement it could be used to explain the physics at underdoped side of the phase diagram without resorting to complex Fermi surface reconstruction scenarios proposed by LeBoeuf *et al.* The first port of call for the refinement would be the inclusion of the Fermi velocity in the scattering rate which may also improve the agreement in the overdoped side.

A novel doping determination technique is presented based on the method outlined by Ando *et al.* by matching the high temperature Hall data of the BSCO2201 samples to Hall data of samples of overdoped Tl2201 of known doping. The method assigns doping values that fall between the ‘universal’ method of Presland/Tallon and those found from

ARPES measurements by Kondo *et al.*

A natural continuation of this work would include a more precise determination of the low field region to determine with more certainty if the low temperature behaviour is truly  $T$ -linear or it plateaus at very low temperatures as found by Balkirev *et al.* in underdoped samples [79] and then attempt to model it using the Ong construction.



# Chapter 6

## Conclusions

In chapter 4 dHvA measurements were presented on high quality samples of BaFe<sub>2</sub>P<sub>2</sub>. Energy dispersions from DFT calculations were tweaked to match the measured Fermi surface orbits by rigidly shifting both the inner and outer electron energy bands and the inner hole band by 0.0050 Ry, 0.0043 Ry and -0.0083 Ry respectively. The hourglass shaped outer hole band energy required no shift at the wide part and a shift of -0.0038 Ry at the narrow part which was found to be nested with the inner electron band. To achieve a smooth transition between the two energy shift regimes, the dispersion was tweaked proportionally to the  $d_{z^2}$  band character and a complete Fermi surface was determined. Similar energy shifts were necessary to correct DFT data for the closely related compound SrFe<sub>2</sub>P<sub>2</sub> which is similarly nested but no shifts were necessary for the DFT dispersions modelling CaFe<sub>2</sub>P<sub>2</sub> which is not nested. The fact that electron-electron correlations are only accounted for in DFT calculations on a mean-field level and that the discrepancies occur at areas which show nesting suggests that these shortcomings in the DFT data are due to spin fluctuations arising from the nesting condition renormalising the band structure. To further investigate this the bare Lindhard susceptibility was computed and the nesting condition was clearly shown along the  $q = (\pi, \pi)$  vector between hole and electron bands despite the fact that no superconductivity is present in BaFe<sub>2</sub>P<sub>2</sub>. The conclusion is that partial nesting is not alone a sufficient condition for superconductivity.

The thermal effective masses were determined on the electron and, for the first time, hole orbits and the spin effective masses on the electron orbits. The masses showed a moderate renormalisation (between 0.88  $m_b$  and 3.04  $m_b$ ) on both hole and electron bands in line with previous literature [20]. Also presented in chapter 4 is an analytical fit to the Fermi surface similar to that in Bergemann *et al.* [112] for future use in theoretical models. It also includes a mapping of the progression of key orbit area sizes of the Fermi surface determined across the BaFe<sub>2</sub>(As<sub>1-x</sub>P<sub>x</sub>)<sub>2</sub> series using Vegard's law in order to aid the correction of DFT calculations.

The next step in this line of research would be to continue performing dHvA measurements on other members of the BaFe<sub>2</sub>(As<sub>1-x</sub>P<sub>x</sub>)<sub>2</sub> series in order to determine the topology and scale of the missing hole pockets, especially around the superconducting dome. This would provide further insight into whether nesting really is a crucial component of the exotic superconductivity and also shed some light on the validity of DFT calculations.

In chapter 5 Hall measurements taken in high field from 1.4 K to 300 K on good quality samples of BSCO2201 were presented. A sharp change in  $R_H(0 \text{ K})/R_H(300 \text{ K})$  was

observed at  $p = 0.19$  which coincides with other phenomena which indicate the presence of the pseudogap [61]. Since this occurs inside of the superconducting dome this is evidence in support of the scenario where the pseudogap drops inside of the superconducting dome.

A simple anisotropic scattering model based on the Ong construction [105] was fitted to the Hall data and the resulting scattering terms,  $\Gamma = \Gamma_0 + \Gamma_1 \cos(2\phi)^2 T + \Gamma_2 T^2$  were used to calculate the longitudinal resistivity and normalised to the 300 K values of the fitted resistivity curves. In general the comparison between the fitted resistivity curve coefficients and the coefficients obtained from the anisotropic model agreed within at least an order of magnitude with the linear in  $T$  term matching to within a factor of 0.6 to 1.5. The residual  $\rho_0^{RH}$  term obtained from the model is consistently undervalued by a factor of around 2 to 10. The  $T^2$  term from the anisotropic model is overvalued by up to a factor of 5.9 on the overdoped side to being undervalued by a factor of 5 on the underdoped side. This is likely due to the relative proximity to the van-Hove singularity and the fact that the model did not include a  $v_F$  term in the scattering rate. The results provide a good starting point for further refinement and possible full agreement between temperature dependent Hall and resistivity data in the cuprates without resorting to complicated Fermi surface reconstruction models such as that proposed by LeBoeuf *et al.* [63].

Finally, presented in chapter 5 is a novel doping determination technique based on a method of matching high temperature Hall coefficient to Tl2201 as a reference material. The resulting dopings are greater than those from the ‘universal’ Presland/Tallon relation [75] and less than those assigned to similar samples measured with ARPES [80]. The overall spread in dopings for these samples from this new method was determined to be between  $p = 0.12$  and  $p = 0.36$ .

Further refinements on the anisotropic scattering model is required to provide solid evidence that the model is an appropriate explanation of the temperature dependence of the low temperature Hall behaviour. In particular the effects of the Fermi velocity on the model close to the van-Hove singularity can be included relatively easily and would show whether this is the cause of the disparity of the model at higher temperatures. Moreover, a more precise determination of the low temperature Hall behaviour in BSCO2201 would better constrain the model as well as resolve any ambiguities as to whether the low temperature behaviour is, for example, linear in temperature.

# Bibliography

- [1] Y. Kamihara et al. *Journal of the American Chemical Society* **128** (2006), pp. 10012–3. DOI: [10.1021/ja063355c](https://doi.org/10.1021/ja063355c).
- [2] Y. Kamihara et al. *Journal of the American Chemical Society* **130** (2008), pp. 3296–7. DOI: [10.1021/ja800073m](https://doi.org/10.1021/ja800073m).
- [3] J. P. Attfield. *arxiv.org* (2010), pp. 1–20. DOI: [10.1039/C0JM03274C](https://doi.org/10.1039/C0JM03274C). eprint: [1012.1771](https://arxiv.org/abs/1012.1771).
- [4] D. C. Johnston. *Advances in Physics* **59** (2010), pp. 803–1061. DOI: [10.1080/00018732.2010.513480](https://doi.org/10.1080/00018732.2010.513480).
- [5] Z.-A. Ren et al. *EPL (Europhysics Letters)* **83** (2008), p. 17002. DOI: [10.1209/0295-5075/83/17002](https://doi.org/10.1209/0295-5075/83/17002).
- [6] C. Wang et al. *EPL (Europhysics Letters)* **83** (2008), p. 67006. DOI: [10.1209/0295-5075/83/67006](https://doi.org/10.1209/0295-5075/83/67006).
- [7] G. Wu et al. *Journal of physics. Condensed matter : an Institute of Physics journal* **21** (2009), p. 142203. DOI: [10.1088/0953-8984/21/14/142203](https://doi.org/10.1088/0953-8984/21/14/142203).
- [8] A. Carrington et al. *Physica C: Superconductivity* **469** (2009), pp. 459–468. DOI: [10.1016/j.physc.2009.03.045](https://doi.org/10.1016/j.physc.2009.03.045).
- [9] A. Coldea et al. *Physical Review Letters* **103** (2009), pp. 1–4. DOI: [10.1103/PhysRevLett.103.026404](https://doi.org/10.1103/PhysRevLett.103.026404).
- [10] A. Carrington. *Reports on Progress in Physics* **74** (2011), p. 124507. DOI: [10.1088/0034-4885/74/12/124507](https://doi.org/10.1088/0034-4885/74/12/124507).
- [11] J. G. Analytis et al. *Physical Review Letters* **103** (2009), pp. 1–4. DOI: [10.1103/PhysRevLett.103.076401](https://doi.org/10.1103/PhysRevLett.103.076401).
- [12] J. G. Analytis et al. *Physical Review B* **80** (2009). DOI: [10.1103/PhysRevB.80.064507](https://doi.org/10.1103/PhysRevB.80.064507). eprint: [0902.1172](https://arxiv.org/abs/0902.1172).
- [13] T. Terashima et al. *Physical Review Letters* **107** (2011), pp. 1–5. DOI: [10.1103/PhysRevLett.107.176402](https://doi.org/10.1103/PhysRevLett.107.176402). eprint: [1103.3329](https://arxiv.org/abs/1103.3329).
- [14] J. Paglione and R. L. Greene. *Nature Physics* **6** (2010), pp. 645–658. DOI: [10.1038/nphys1759](https://doi.org/10.1038/nphys1759).
- [15] Y. Nakai et al. *Physical Review Letters* **105** (2010), pp. 31–34. DOI: [10.1103/PhysRevLett.105.107003](https://doi.org/10.1103/PhysRevLett.105.107003).
- [16] T. Yamazaki et al. *Physical Review B* **81** (2010), pp. 1–5. DOI: [10.1103/PhysRevB.81.224511](https://doi.org/10.1103/PhysRevB.81.224511).
- [17] E. Colombier et al. *Physical Review B* **79** (2009), pp. 1–9. DOI: [10.1103/PhysRevB.79.224518](https://doi.org/10.1103/PhysRevB.79.224518).
- [18] P. L. Alireza et al. *Journal of Physics: Condensed Matter* **21** (2009), p. 012208. DOI: [10.1088/0953-8984/21/1/012208](https://doi.org/10.1088/0953-8984/21/1/012208).
- [19] L. E. Klintberg et al. *Journal of the Physical Society of Japan* **2** (2010), p. 5. DOI: [10.1143/JPSJ.79.123706](https://doi.org/10.1143/JPSJ.79.123706). eprint: [1009.2716](https://arxiv.org/abs/1009.2716).

- [20] H. Shishido et al. *Physical Review Letters* **104** (2010), pp. 1–4. DOI: 10.1103/PhysRevLett.104.057008.
- [21] C. van der Beek et al. *Physical Review Letters* **105** (2010), pp. 4–7. DOI: 10.1103/PhysRevLett.105.267002.
- [22] J. G. Analytis et al. *Physical Review Letters* **105** (2010), pp. 1–4. DOI: 10.1103/PhysRevLett.105.207004.
- [23] T. Kondo et al. *Physical Review B* **81** (2010), pp. 1–4. DOI: 10.1103/PhysRevB.81.060507.
- [24] T. Yoshida et al. *Physical Review Letters* **106** (2011), p. 4. DOI: 10.1103/PhysRevLett.106.117001. eprint: 1008.2080.
- [25] J. F. Annett. *Superconductivity, Superfluids and Condensates*. Oxford University Press, 2010, 22ff. ISBN: 978-0-19-850756-7.
- [26] J. Bardeen, L. N. Cooper, and J. R. Schrieffer. *Physical Review* **108** (1957), pp. 1175–1204. DOI: 10.1103/PhysRev.108.1175.
- [27] D. Osheroff, R. Richardson, and D. Lee. *Physical Review Letters* **28** (1972), pp. 885–888. DOI: 10.1103/PhysRevLett.28.885.
- [28] J. G. Bednorz and K. A. Müller. *Zeitschrift für Physik B Condensed Matter* **64** (1986), pp. 189–193.
- [29] J. F. Annett, N. Goldenfeld, and S. Renn. *Physical Review B* **43** (1991), pp. 2778–2782. DOI: 10.1103/PhysRevB.43.2778.
- [30] D. J. Van Harlingen et al. *Physica C: Superconductivity* **235** (1994), pp. 122–125.
- [31] Y. Wang et al. *Physical Review B* **83** (2011), pp. 4–8. DOI: 10.1103/PhysRevB.83.054509.
- [32] O. M Froehlich et al. *Europhysics Letters* **36** (1996), pp. 467–472. DOI: 10.1209/epl/i1996-00253-5.
- [33] R. A. Cooper et al. *Science* **323** (2009), pp. 603–7. DOI: 10.1126/science.1165015.
- [34] J. Custers et al. *Nature* **424** (2003), pp. 524–7. DOI: 10.1038/nature01774.
- [35] L. Boeri, O. V. Dolgov, and a. a. Golubov. *Physical Review Letters* **101** (2008), pp. 1–4. DOI: 10.1103/PhysRevLett.101.026403.
- [36] I. I. Mazin. *Physica C: Superconductivity* **468** (2008), pp. 105–110. DOI: 10.1016/j.physc.2007.08.015.
- [37] K. Haule, J. H. Shim, and G. Kotliar. *Physical Review Letters* **100** (2008), pp. 3–6. DOI: 10.1103/PhysRevLett.100.226402.
- [38] S. Jiang et al. *Journal of Physics: Condensed Matter* **21** (2009), p. 382203. DOI: 10.1088/0953-8984/21/38/382203.
- [39] S. Kasahara et al. *Physical Review B* **81** (2010), pp. 1–5. DOI: 10.1103/PhysRevB.81.184519.
- [40] K. Hashimoto et al. *Physical Review Letters* **108** (2012), pp. 1–5. DOI: 10.1103/PhysRevLett.108.047003.
- [41] Y. Zhang et al. *Nature Materials* **10** (2011), pp. 273–7. DOI: 10.1038/nmat2981.

- [42] H. Ding et al. *Europhysics Letters* **83** (2008), p. 47001. DOI: 10.1209/0295-5075/83/47001.
- [43] K Terashima et al. *Proceedings of the National Academy of Sciences* **106** (2009), pp. 7330–3. DOI: 10.1073/pnas.0900469106.
- [44] J. Fletcher et al. *Physical Review Letters* **102** (2009), pp. 1–4. DOI: 10.1103/PhysRevLett.102.147001.
- [45] X. Qiu et al. *arxiv.org* **2** (2011), p. 5. eprint: 1112.2421.
- [46] C.-L. Song et al. *Science* **332** (2011), pp. 1410–3. DOI: 10.1126/science.1202226.
- [47] J. K. Dong et al. *Physical Review Letters* **104** (2010), pp. 1–4. DOI: 10.1103/PhysRevLett.104.087005.
- [48] Y. Zhang et al. *Nature Physics* **8** (2012), pp. 371–375. DOI: 10.1038/nphys2248. eprint: 1109.0229.
- [49] M. Yamashita et al. *Physical Review B* **84** (2011), pp. 1–4. DOI: 10.1103/PhysRevB.84.060507.
- [50] K. Suzuki, H. Usui, and K. Kuroki. *Journal of the Physical Society of Japan* **80** (2011), p. 013710. DOI: 10.1143/JPSJ.80.013710.
- [51] Y. J. Uemura. *Nature Physics* **8** (2009), pp. 253–255.
- [52] N. Berk and J. Schrieffer. *Physical Review Letters* **17** (1966), pp. 433–435. DOI: 10.1103/PhysRevLett.17.433.
- [53] D. Scalapino. *Physics Reports* **250** (1995), pp. 329–365. DOI: 10.1016/0370-1573(94)00086-I.
- [54] I. I. Mazin. *Nature* **464** (2010), pp. 183–6. DOI: 10.1038/nature08914.
- [55] J. Orenstein and A. Vishwanath. *Nature Physics* **6** (2010), pp. 566–567. DOI: 10.1038/nphys1751.
- [56] H. Tasaki. *Journal of Physics: Condensed Matter* **10** (1998), pp. 4353–4378. DOI: 10.1088/0953-8984/10/20/004.
- [57] N. E. Hussey. *Journal of Physics: Condensed Matter* **20** (2008), p. 123201. DOI: 10.1088/0953-8984/20/12/123201.
- [58] W. Warren et al. *Physical Review Letters* **62** (1989), pp. 1193–1196. DOI: 10.1103/PhysRevLett.62.1193.
- [59] S. M. Hayden. “Neutron Scattering and the Magnetic Response of Superconductors and Related Compounds”. *Superconductivity*. Springer Berlin Heidelberg, 2008, pp. 993–1029. ISBN: 978-3-540-73253-2.
- [60] S. Hüfner et al. *Reports on Progress in Physics* **71** (2008), p. 062501. DOI: 10.1088/0034-4885/71/6/062501.
- [61] J. Tallon. *Physica C: Superconductivity* **349** (2001), pp. 53–68. DOI: 10.1016/S0921-4534(00)01524-0.
- [62] S. A. Kivelson et al. *Reviews of Modern Physics* **75** (2003), pp. 1201–1241. DOI: 10.1103/RevModPhys.75.1201.
- [63] D. LeBoeuf et al. *Physical Review B* **83** (2011), pp. 1–14. DOI: 10.1103/PhysRevB.83.054506.

- [64] M. Vojta. *Physics* **4** (2011). DOI: 10.1103/Physics.4.12.
- [65] N. E. Hussey. *The European Physical Journal B* **31** (2003), pp. 495–507. DOI: 10.1140/epjb/e2003-00059-9.
- [66] N. E. Hussey. *Journal of Physics and Chemistry of Solids* **72** (2011), pp. 529–532. DOI: 10.1016/j.jpcs.2010.10.057.
- [67] M. Abdel-Jawad et al. *Nature Physics* **2** (2006), pp. 821–825. DOI: 10.1038/nphys449.
- [68] L. Taillefer. *Nature Physics* **2** (2006), pp. 809–810. DOI: 10.1038/nphys478a.
- [69] M. Norman. *Physics* **3** (2010). DOI: 10.1103/Physics.3.86.
- [70] M. Hashimoto et al. *Physical Review B* **77** (2008), pp. 1–9. DOI: 10.1103/PhysRevB.77.094516.
- [71] A. Narduzzo et al. *Physical Review B* **77** (2008), pp. 4–7. DOI: 10.1103/PhysRevB.77.220502.
- [72] C. Torardi et al. *Physical Review B* **38** (1988), pp. 225–231. DOI: 10.1103/PhysRevB.38.225.
- [73] D. C. Peets et al. *New Journal of Physics* **9** (2007), pp. 28–28. DOI: 10.1088/1367-2630/9/2/028.
- [74] T. Kondo et al. *Physical Review Letters* **98** (2007), pp. 1–4. DOI: 10.1103/PhysRevLett.98.267004.
- [75] M. Presland et al. *Physica C: Superconductivity* **176** (1991), pp. 95–105. DOI: 10.1016/0921-4534(91)90700-9.
- [76] Y. Ando et al. *Physical Review B* **61** (2000), R14956–R14959. DOI: 10.1103/PhysRevB.61.R14956.
- [77] P. M. C. Rourke et al. *New Journal of Physics* **12** (2010), p. 105009. DOI: 10.1088/1367-2630/12/10/105009.
- [78] Y. Ando and T Murayama. *Physical Review B* **60** (1999), R6991–R6994. DOI: 10.1103/PhysRevB.60.R6991.
- [79] F. F. Balakirev et al. *Nature* **424** (2003), pp. 912–5. DOI: 10.1038/nature01890.
- [80] T. Kondo et al. *Journal of Electron Spectroscopy and Related Phenomena* **137-140** (2004), pp. 663–668. DOI: 10.1016/j.elspec.2004.02.104.
- [81] N. Ashcroft and N. Mermin. *Solid State Physics*. Thomson Learning, 1976. ISBN: 0-03-083993-9.
- [82] C. Kittel. *Introduction To Solid State Physics*. John Wiley & Sons Inc., 1996. ISBN: 0 471 11181 3.
- [83] D. Shoenberg. *Magnetic oscillations in metals*. Cambridge University Press, 1984. ISBN: 978-0-521-11878-1.
- [84] S. Blundell. *Magnetism in Condensed Matter*. Oxford University Press, 2001.
- [85] A. Carrington, J. Fletcher, and H. Harima. *Physical Review B* **71** (2005), pp. 2–5. DOI: 10.1103/PhysRevB.71.174505.
- [86] K. Yamaji. *Journal of the Physical Society of Japan* **58** (1989), pp. 1520–1523.

- [87] A. Wasserman, M. Springford, and F Han. *Journal of Physics: ...* **3** (1991), pp. 5335–5339.
- [88] A. Wasserman and M. Springford. *Advances in Physics* **45** (1996), pp. 471–503. DOI: [10.1080/00018739600101547](https://doi.org/10.1080/00018739600101547).
- [89] T. Moriya. *Spin fluctuations in itinerant electron magnetism*. Springer Verlag, 1985, 25 ff. ISBN: 3-540-15422-1.
- [90] M. Dressel and G. Gruner. *Electrodynamics Of Solids*. Cambridge University Press, 2002, p. 126. ISBN: 0 521 59726 9.
- [91] N. Majlis. *The Quantum Theory of Magnetism*. World Scientific Publishing Co., 2007. ISBN: 13-978-981-256-792-5.
- [92] P. Monthoux, D. Pines, and G. G. Lonzarich. *Nature* **450** (2007), pp. 1177–83. DOI: [10.1038/nature06480](https://doi.org/10.1038/nature06480).
- [93] D. L. Cox and M. B. Maple. *Physics Today* **48** (1995), p. 32. DOI: [10.1063/1.881443](https://doi.org/10.1063/1.881443).
- [94] P. Blaha et al. *WIEN2K, An Augmented Plane Wave + Local Orbitals Program for Calculating Crystal Properties*. Karlheinz Schwarz Techn. Universitat, 2001. ISBN: 3-9501031-1-2.
- [95] M. Luders. *Electrons In Solids*. 2010.
- [96] K. Burke. *The ABC of DFT*. 2003.
- [97] P. Hohenberg. *Physical Review* **136** (1964), B864–B871. DOI: [10.1103/PhysRev.136.B864](https://doi.org/10.1103/PhysRev.136.B864).
- [98] M. Levy. *Proceedings of the National Academy of Sciences* **76** (1979), pp. 6062–6065. DOI: [10.1073/pnas.76.12.6062](https://doi.org/10.1073/pnas.76.12.6062).
- [99] C. G. Broyden. *Mathematics of Computation* **19** (1965), p. 577. DOI: [10.2307/2003941](https://doi.org/10.2307/2003941).
- [100] J. P. Perdew, K. Burke, and M. Ernzerhof. *Physical Review Letters* **77** (1996), pp. 3865–3868. DOI: [10.1103/PhysRevLett.77.3865](https://doi.org/10.1103/PhysRevLett.77.3865).
- [101] J. P. Perdew and W. Yue. *Physical Review B* **33** (1986), pp. 8800–8802. DOI: [10.1103/PhysRevB.33.8800](https://doi.org/10.1103/PhysRevB.33.8800).
- [102] O. K. Andersen. *Physical Review B* **12** (1975), pp. 3060–3083. DOI: [10.1103/PhysRevB.12.3060](https://doi.org/10.1103/PhysRevB.12.3060).
- [103] G. Madsen et al. *Physical Review B* **64** (2001), pp. 1–9. DOI: [10.1103/PhysRevB.64.195134](https://doi.org/10.1103/PhysRevB.64.195134).
- [104] M. M. J. French. “Angle dependent magnetoresistance in  $Tl_2Ba_2CuO_{6+\delta}$ ”. PhD thesis. University of Bristol, 2009.
- [105] N. Ong. *Physical Review B* **43** (1991), pp. 193–201. DOI: [10.1103/PhysRevB.43.193](https://doi.org/10.1103/PhysRevB.43.193).
- [106] C. M. J. Andrew. “The Fermi surface of iron pnictides”. PhD thesis. University of Bristol, 2010.
- [107] *Heliox and superconducting magnet system - Operators handbook*. Oxford Instruments, 1998.

- [108] M. Platé et al. *Physical Review Letters* **95** (2005), p. 077001. DOI: 10.1103/PhysRevLett.95.077001.
- [109] P. M. C. Rourke et al. *New Journal of Physics* **12** (2010), p. 4. DOI: 10.1088/1367-2630/12/10/105009. eprint: 1005.0573.
- [110] M. Rotter, C. Hieke, and D. Johrendt. *Physical Review B* **82** (2010), pp. 1–7. DOI: 10.1103/PhysRevB.82.014513. eprint: arXiv:1005.1411v2.
- [111] A Mewis. *Z. Naturforsch* **35b** (1980), p. 141.
- [112] C. Bergemann et al. *Physical Review Letters* **84** (2000), pp. 2662–5.
- [113] L. Ortenzi et al. *Physical Review Letters* **103** (2009), pp. 1–4. DOI: 10.1103/PhysRevLett.103.046404.
- [114] W. D. Wise et al. *Nature Physics* **5** (2009), pp. 213–216. DOI: 10.1038/nphys1197.
- [115] W. D. Wise et al. *Nature Physics* **4** (2008), pp. 696–699. DOI: 10.1038/nphys1021.
- [116] T. Kondo et al. *Physical Review B* **72** (2005), pp. 1–9. DOI: 10.1103/PhysRevB.72.024533.
- [117] T. Kondo et al. *Nature Physics* **7** (2010), pp. 21–25. DOI: 10.1038/nphys1851.
- [118] T. Kondo et al. *Nature* **457** (2009), pp. 296–300. DOI: 10.1038/nature07644.
- [119] T. Kondo et al. *Physical Review B* **74** (2006), pp. 1–9. DOI: 10.1103/PhysRevB.74.224511.
- [120] M. Abdel-Jawad et al. *Physical Review Letters* **99** (2007), pp. 10–13. DOI: 10.1103/PhysRevLett.99.107002.
- [121] J. Kokalj, N. Hussey, and R. McKenzie. *Physical Review B* **86** (2012), pp. 1–16. DOI: 10.1103/PhysRevB.86.045132.
- [122] Z. Konstantinović, Z. Li, and H. Raffy. *Physica C: Superconductivity* **351** (2001), pp. 163–168. DOI: 10.1016/S0921-4534(00)01733-0.

# Appendix A

## ‘Microfit’ parameters

Fit parameters for the ‘microfitting’ technique described in section 3.1.4. Note: at 46° the peak is twinned.

Angle (deg.)	Band	Frequency (T)	Fit Periods	Filter Range
12	$\alpha_1$	1210	1.5	1100–1240
28	$\alpha_1$	1269	1.5	1200–1310
46	$\alpha_1$	1532	1.5	1430–1585
12	$\alpha_2$	1372	1.5	1320–1440
28	$\alpha_2$	1530	1.5	1450–1650
46	$\alpha_2$	2017	1.5	1970–2100
28	$\beta_2$	1365	1.5	1320–1440
12	$\beta_1$	2180	1.5	2100–2270
12	$\beta_2$	2500	1.5	2450–2550
28	$\beta_2$	2605	1.5	2555–2670
46	$\beta_2$	3347	1.5	3250–3370
46	$\beta_2$	3381	1.5	3365–2500
12	$\beta_3$	2350	1.5	2270–2450
28	$\beta_3$	2475	1.5	2400–2560
46	$\beta_3$	2970	1.5	2850–3100
12	$\delta$	1270	1.5	1250–1310
46	$\delta$	1626	1.5	1590–1690
28	$\gamma_1$	912	1.5	850–970
46	$\gamma_1$	1320	1.5	1270–1370
46	$\gamma_2$	4497	1.5	4400–4600



## Appendix B

# Lindhard susceptibility calculation code

The following is MATLAB code known to run on release 2008b.

```
1 function [total_re_x0 total_im_x0] = calc_x0(fs, T, delta, omega, ...
2     q_space, energy_ind_combs, out_filestem)
3
4 % A function to calculate the non-interacting susceptibility according to
5 % the Lindhard function. Matrix elements are assumed to be unity.
6 %
7 % energy_ind_combs: Optional Nx2 matrix of band pairs (default: empty,
8 %                     All band pairs are calculated)
9 % temperature:      Temperature (default: Absolute zero - slightly
10 %                  quicker to calculate)
11 % delta:           Quasiparticle lifetime, if zero this will give
12 %                  zero for the imaginary portion of the
13 %                  susceptibility (default: zero)
14 % omega:           Perturbation frequency (default: zero)
15 % out_filestem:   Filestem for all the individual band combinations
16 %                  Default: 'x0'
17 % q_space:        Indices of Q space to calculate passed as a cell array
18 %                  of 3 vectors, first for the Qx indices, second
19 %                  for the Qy indices, third for the Qz indices. An
20 %                  empty cell array or an empty vector in the
21 %                  cell array defaults to the full extent of
22 %                  grid of energy points. N.B. Since we are
23 %                  dealing with indices, not k-space values, 1
24 %                  corresponds to a zero in q-space (i.e.
25 %                  qx = (n-1)*dk_x where n is the number passed)
26 %
27 % RETURNS:
28 %     re_x0:          Real values of x0
29 %     im_x0:          Im values of x0
30 %
31 %
32 %
33 % Use to test the code. Generates free electron energy dispersion and
34 % calculates a susceptibility. Actually not straightforward since free
35 % electron dispersion is not periodic.
36 TEST_FREE_ELECTRON = false;
37 DIMENSIONS = 3;
38
```

```

39
40 if TEST_FREE_ELECTRON
41     clear fs;
42     free_electron_dispersion = @(kx, ky, kz) (kx.^2 + ky.^2 + kz.^2);
43     delta = 1e-9;
44     omega = 1e-9;
45     MAX_L = 1;
46     MIN_L = -1;
47     NUM PTS = 100;
48     fs.dL = (MAX_L - MIN_L) / (NUM PTS - 1);
49     fs.FermiLevel = 0.09;
50     L = linspace(MIN_L, MAX_L, NUM PTS);
51 if DIMENSIONS == 3
52     [fs.cartX, fs.cartY, fs.cartZ] = meshgrid(L, L, L);
53     q_space = {[[], [], []]};
54     % Calculate distance each grid point is from centre in order
55     % to build the symmetry mask
56     [x y z] = meshgrid(1:NUM PTS, 1:NUM PTS, 1:NUM PTS);
57     r = hypot(hypot(x - NUM PTS ./ 2, y - NUM PTS ./ 2), ...
58                 z - NUM PTS ./ 2);
59 elseif DIMENSIONS == 2
60     [fs.cartX, fs.cartY, fs.cartZ] = meshgrid(L, L, 0);
61     q_space = {[[], [], 1]};
62     [x y] = meshgrid(1:NUM PTS, 1:NUM PTS);
63     r = hypot(x - NUM PTS ./ 2, y - NUM PTS ./ 2);
64 else
65     error('Number of dimensions not supported');
66 end
67 % Symmetry mask based on Fermi function, ensures that the
68 % symmetry is spherical for the non-repeating free-electron case
69 MASK_TRIM = 1.5;
70 MASK_DECAY = 10;
71 sym_mask = 1 ./ (exp((r - (NUM PTS ./ 2 - MASK_TRIM)) ...
72                     * MASK_DECAY) + 1);
73 fs.cartE = {};
74 fs.cartE{1} = free_electron_dispersion(fs.cartX, fs.cartY, ...
75                                         fs.cartZ);
76 end
77
78
79 % Set the temperature
80 if isempty(T)
81     T = 0;
82 end
83 disp(sprintf('Temperature set to: %.3f', T));
84
85 % Set the lifetime
86 if isempty(delta)
87     delta = 0;
88 end

```

```

89 disp(sprintf('Quasiparticle lifetime set to: %.3f', delta));
90
91 % Set omega
92 if isempty(omega)
93     omega = 0;
94 end
95 disp(sprintf('Plasma frequency set to: %.3f', omega));
96
97 % Set the output filestem
98 if isempty(out_filestem)
99     out_filestem = 'x0';
100 end
101 disp(['Filestem set to: ' out_filestem]);
102
103 % Set the size of the Q region to be calculated
104 [num_qx num_qy num_qz] = size(fs.cartE{1});
105 if isempty(q_space)
106     q_space = {[[] [] []]};
107 end
108 if isempty(q_space{1})
109     qx_range = 1:num_qx;
110 else
111     qx_range = q_space{1};
112 end
113 if isempty(q_space{2})
114     qy_range = 1:num_qy;
115 else
116     qy_range = q_space{2};
117 end
118 if isempty(q_space{3})
119     qz_range = 1:num_qz;
120 else
121     qz_range = q_space{3};
122 end
123 disp(sprintf('Size of q space is: %dx%dx%d', num_qx, num_qy, num_qz));
124
125 % Set the combinations of bands to be calculated
126 % Replace if necessary
127 if isempty(energy_ind_combs)
128     % Compile a list of combinations of the bands in terms of indices
129     n = length(fs.cartE);
130     energy_ind_combs = zeros([n 2]);
131     i = 0;
132     for ind1 = 1:n
133         for ind2 = 1:n
134             i = i + 1;
135             energy_ind_combs(i,1) = ind1;
136             energy_ind_combs(i,2) = ind2;
137         end
138     end

```

```

139 end
140 disp('Band combinations to be calculated and summed over:');
141 disp(energy_ind_combs);
142
143
144 %K_BOLTZ = 1.3806503e-23;
145 K_BOLTZ = 6.3336e-6; % In Rydbergs
146
147 total_im_x0 = zeros(num_qx, num_qy, num_qz);
148 total_re_x0 = zeros(num_qx, num_qy, num_qz);
149
150 % This will be 'Inf' if T=0 but will not be used later if this is
151 % the case
152 beta = 1 ./ (K_BOLTZ .* T);
153
154 for inds = energy_ind_combs'
    % Assign the two coupled bands to be calculated
    energies = fs.cartE{inds(1)};
    q_energies = fs.cartE{inds(2)};
    % Initialise the results matrices
    im_x0 = zeros(num_qx, num_qy, num_qz);
    re_x0 = zeros(num_qx, num_qy, num_qz);
    % Iterate over all Q vectors
    for k = qz_range
        for j = qy_range
            disp(sprintf('Bands %d->%d: k=%d\bj=%d', inds', k, j));
            for i = qx_range
                % Determine the energies at k+Q
                if TEST_FREE_ELECTRON
                    qx = (i - 1) .* fs.dL;
                    qy = (j - 1) .* fs.dL;
                    qz = (k - 1) .* fs.dL;
                    energies_prime = free_electron_dispersion(fs.cartX ...
                        + qx, fs.cartY + qy, fs.cartZ + qz);
                else
                    energies_prime = circshift(q_energies, [i - 1, ...
                        j - 1, k - 1]);
                end
                % x0 (non-interacting susceptibility) is of form
                % A / (B + iC)
                % Re(x0) is of form AB / (B^2 + C^2)
                % Im(x0) is of form -CA / (B^2 + C^2)
                %
                % Quicker approximation for T=0 that also avoids Inf in
                % calculation
                if T == 0
                    A = (energies <= fs.FermiLevel) - (energies_prime ...
                        <= fs.FermiLevel);
                else
                    A = 1 ./ (exp(beta .* (energies - fs.FermiLevel)) ...

```

```

189          + 1 ) - 1 ./ ( exp(beta .* (energies_prime - ...
190              fs.FermiLevel)) + 1 );
191      end
192
193      B = energies_prime - energies - omega;
194      C = delta; % Is -delta in formula, but this is cancelled
195          % by a negative when finally calculating Im(x0)
196
197      D = A ./ (B.^2 + C.^2);
198
199      im_result = C .* D;
200      re_result = B .* D;
201
202      % Remove NaNs (usu. from 0/0 operations)
203      im_result(isnan(im_result)) = 0;
204      re_result(isnan(re_result)) = 0;
205
206      if TEST_FREE_ELECTRON
207          im_result = im_result .* sym_mask;
208          re_result = re_result .* sym_mask;
209      end
210
211      im_x0(i, j, k) = sum(im_result(:));
212      re_x0(i, j, k) = sum(re_result(:));
213
214  end
215
216  % Save this band pair data individually before combining with overall
217  % x0
218  save(sprintf([out_filestem '_Bands=%d-%d'], inds), 're_x0', 'im_x0');
219  total_im_x0 = total_im_x0 + im_x0;
220  total_re_x0 = total_re_x0 + re_x0;
221 end
222
223 end

```

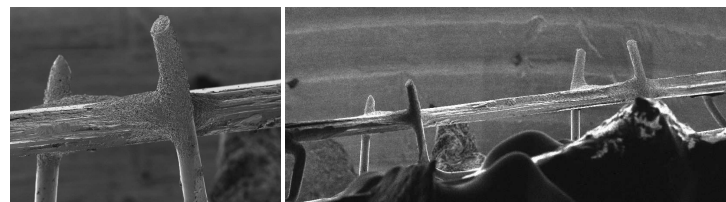


## Appendix C

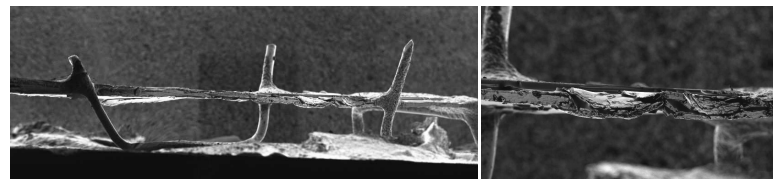
### FIB scans

Exemplary images from the FIB scans performed with the help of Dr. P. Heard.

B00KOD1a



B07KOD2



B16KOD1a



B30KOD3

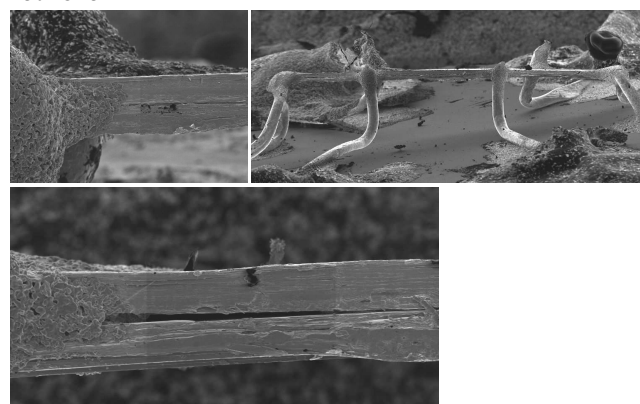


Figure C.0.1

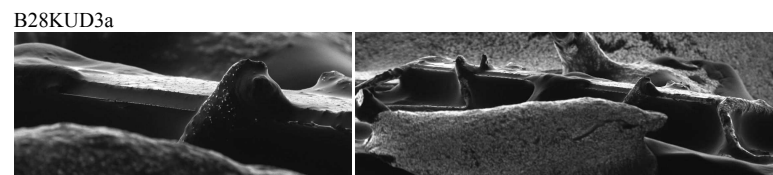
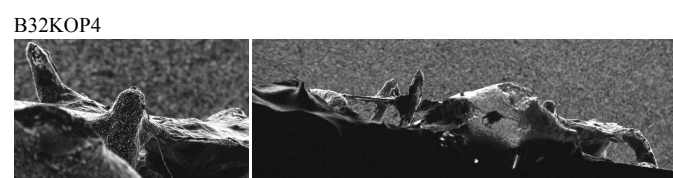
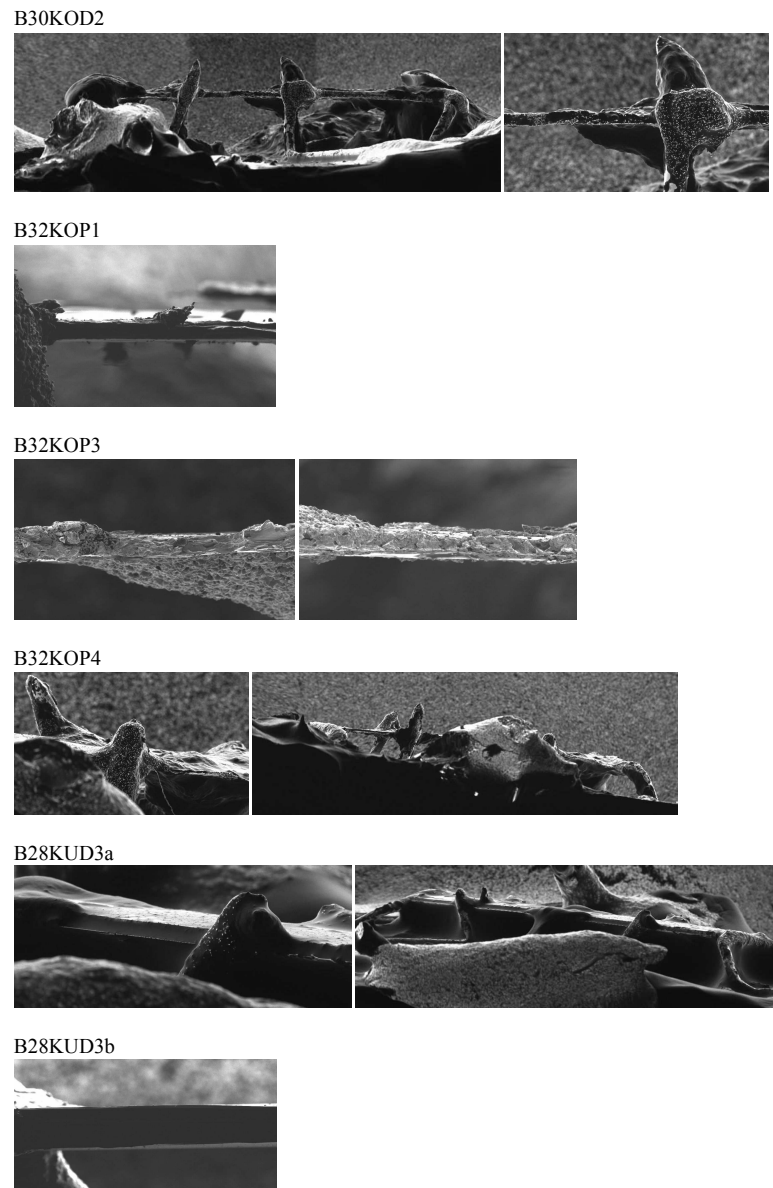


Figure C.0.2